

**STUDY OF POST-NECKING HARDENING IDENTIFICATION AND
DEFORMATION-INDUCED SURFACE ROUGHENING OF METALS**

BY

PAUL KNYSH

BS, Dnipro National University, 2012

MS, University of New Hampshire, 2014

DISSERTATION

Submitted to the University of New Hampshire

in Partial Fulfillment of

the Requirements for the Degree of

Doctor of Philosophy

in

Mechanical Engineering

September, 2019

This dissertation was examined and approved in partial fulfillment of the requirements for the degree of Doctor of Philosophy in Mechanical Engineering by:

Dissertation Director, Yannis Korkolis, Associate Professor of
Mechanical Engineering, The Ohio State University

Todd Gross, Professor of Mechanical Engineering

Marko Knezevic, Associate Professor of Mechanical Engineering

Igor Tsukrov, Professor of Mechanical Engineering

Tsuyoshi Furushima, Associate Professor of Mechanical Engineering,
The University of Tokyo

On 5/24/19

Approval signatures are on file with the University of New Hampshire Graduate School.

ACKNOWLEDGEMENTS

I would like first to thank my academic advisor, Professor Yannis Korkolis, for his continuous support throughout my PhD program. My research was supported by the U.S. National Science Foundation through the CAREER grant CMMI-1150523 and also by JSPS KAKENHI Grant-in-Aid for Scientific Research (c) Grant Number JP 16K06800.

I would also like to express my gratitude to the rest of my dissertation committee: Prof. Marko Knezevic, Prof. Todd Gross, Prof. Igor Tsukrov and Prof Tsuyoshi Furushima.

I also acknowledge the help of Peter Ripley, Scott Campbell, Mitsuhiro Yamane, Milan Ardeljan, Milovan Zecevic, Miroslav Zecevic and Jinjin Ha with different aspects of my research.

In addition, I would like to acknowledge the support from the Graduate School at the University of New Hampshire.

Finally, I am truly thankful for the support from my friends and family.

TABLE OF CONTENTS

CHAPTER 1 INTRODUCTION.....	1
1.1. General remarks.....	1
1.2. Thesis structure.....	3
CHAPTER 2 IDENTIFICATION OF THE POST-NECKING HARDENING RESPONSE OF RATE- AND TEMPERATURE-DEPENDENT METALS.....	7
2.1. Introduction.....	7
2.2. Experiments.....	10
a. Material properties and experimental setup.....	10
b. Results from conventional tension test.....	12
2.3. Hardening identification procedure.....	14
a. Finite element model.....	15
b. Objective function.....	18
c. Optimization procedure.....	19
d. Application examples.....	21
2.4. Results and discussion.....	25
a. Post-necking hardening response of 304L stainless steel.....	25
b. Predictions of conventional tension of 304L stainless steel.....	34
2.5. Summary and conclusions.....	39
CHAPTER 3 A SHAPE INTERPOLATION PROCEDURE: APPLICATION TO CREATING EXPLICIT GRAIN STRUCTURE MODELS BASED ON PARTIAL DATA SETS.....	42
3.1. Introduction.....	42
3.2. Description of the procedure.....	45
a. Reconstructing the mid-plane image between two images.....	46
b. Generation of a desired number of intermediate layers.....	48
3.3. Application examples.....	49
a. Simple demonstration example.....	49
b. Application to explicit grain structure reconstruction.....	50
c. Application to a reconstruction from multiple sections.....	55
3.4. Summary and conclusions.....	57

CHAPTER 4 DEFORMATION-INDUCED SURFACE ROUGHENING OF AN ALUMINUM-MAGNESIUM ALLOY: EXPERIMENTAL CHARACTERIZATION AND CRYSTAL PLASTICITY MODELING	59
4.1. Introduction	59
4.2. Experiments.....	68
a. Specimen preparation	69
b. Experimental setup	70
4.3. Modeling	74
a. Crystal-plasticity finite element (CPFE) model overview	74
b. Identification of material properties	77
c. Mesh construction	80
d. Finite element model.....	83
4.4. Comparison between experiment and model	84
4.5. Analysis of roughness statistics	99
a. Modeling surface roughening in a polycrystal	99
b. Texture-morphology relations.....	102
4.6. Summary and conclusions.....	107
CHAPTER 5 SUMMARY AND FUTURE WORK.....	110
REFERENCES.....	116
APPENDIX A.....	129
APPENDIX B.....	130
APPENDIX C	132
APPENDIX D	135
APPENDIX E.....	136
APPENDIX F.....	139

LIST OF FIGURES

Figure 2.1 – Setup for conventional and isothermal tension experiments and its components.....	11
Figure 2.2 – A set of conventional tension tests performed at different strain-rates.....	13
Figure 2.3 – Axial strain and temperature fields extracted from DIC and IR cameras...	14
Figure 2.4 – Axisymmetric FE model of a tube with boundary conditions and FE mesh shown.....	17
Figure 2.5a – A schematic of the black-box objective function, where x is the input vector and E is the output error (scalar).	18
Figure 2.5b – A schematic of the procedure for optimizing expensive black box functions.....	19
Figure 2.6 – Example of applying the optimization procedure. Left figure shows original isolines of $f(x,y)$; right figure shows isolines reconstructed using 10 function evaluations (black dots). Red dots show exact and estimated minimum.....	22
Figure 2.7a – An identified input curve that has its post-necking part represented with 2 shape parameters (u_1, u_2).....	24
Figure 2.7b – The matching in force-average axial strain response between FEA and experiment. Corresponds to the identified input curve of Fig. 2.7a.	24
Figure 2.7c – The error function that corresponds to Fig. 2.7a and b, reconstructed with 32 function evaluations. Ranges of u_1, u_2 and error values are normalized to $[0,1]$	25
Figure 2.8a – Identified input curve for the case when rate and temperature effects are not taken into account.	27
Figure 2.8b – The matching in force-average axial strain response between FEA and experiment that corresponds to the identified input curve in Fig. 2.8a.	27
Figure 2.9a – Identified input curves for a constant temperature (25 °C). Rate effect is not taken into account.	29
Figure 2.9b – The matching in force-average axial strain response between FEA and experiments that corresponds to the identified input curves in Fig. 2.9a.....	29
Figure 2.10a – Identified input curves for a constant temperature (15 °C). Both rate and temperature effects are taken into account.	31
Figure 2.10b – The matching in force-average axial strain response between FEA and experiments that corresponds to the identified input curves in Fig. 2.10a.....	31
Figure 2.10c – Identified input curves for a constant temperature (25 °C). Both rate and temperature effects are taken into account.	32
Figure 2.10d – The matching in force-average axial strain response between FEA and experiments that corresponds to the identified input curves in Fig. 2.10c.....	32
Figure 2.10e – Identified input curves for a constant temperature (35 °C). Both rate and temperature effects are taken into account.	33
Figure 2.10f – The matching in force-average axial strain response between FEA and experiments that corresponds to the identified input curves in Fig. 2.10e.....	33

Figure 2.11 – The matching in force-average axial strain response between FEA and experiment for the convection coefficient value identified with optimization procedure (8.4 W/m ² K). Also included is the response from the initial guess.....	35
Figure 2.12 – Evolution of axial strain along the specimen in the conventional tension test.	37
Figure 2.13 – Evolution of hoop strain along the specimen in the conventional tension test.	38
Figure 2.14 – Evolution of neck profile in conventional test.....	38
Figure 2.15 – Evolution of temperature along the specimen in conventional test.....	39
Figure 3.1 – Constructing the mid-plane image (d) from given 2 images (a, b). c shows the overlap of a and b; the mismatch areas are shown in white. Each mismatch area is filled with its neighboring colors iteratively, until image d is obtained.	46
Figure 3.2 – A set of images that interpolates two given images (“lightning” and “star”), produced by the morphing procedure described here.	49
Figure 3.3 – The 3D voxel model produced by stacking the images from Fig. 3.2.	50
Figure 3.4 – EBSD scans of the gauge section of a micro-scale specimen. (a) – top, (b) – bottom. Different colors represent different grains. The black color is representing grains that do not go all the way through the thickness and hence are incompatible with the reconstruction procedure.....	51
Figure 3.5 – A schematic drawing of cross-section of the specimen. Interior sections A and B are shown with dashed lines.	52
Figure 3.6 – Morphology of grain structure at section A; (a) - measured, (b) - reconstructed (c) - the difference between (a) and (b) (gray = match, white = mismatch, 24.2% of the total image).	53
Figure 3.7 – Morphology of grain structure at section B; (a) - measured, (b) - reconstructed (c) - the difference between (a) and (b) (gray = match, white = mismatch, 16.6% of the total image).	54
Figure 3.8 – Reconstructed voxel models of several grains.	55
Figure 3.9 – Optical micrographs used as input for the reconstruction process of a martensite (red) – ferrite (blue) representative volume element.	56
Figure 3.10 – Reconstructed voxel model martensite-ferrite representative volume element and magnification showing the finite element mesh.	57
Figure 4.1 – Dependence between roughness and applied strain observed in Osakada and Oyane 1971.....	61
Figure 4.2 – A columnar model of aluminum oligocrystal studied in Zhao <i>et al.</i> 2008...	63
Figure 4.3 – Geometry of the oligocrystal specimen. (Top) Photo showing the relative size of the dogbone in comparison to rice grains on the left. (Bottom) Engineering drawing of the dogbone (dimensions in mm). Thickness is 134 μ m.	70
Figure 4.4 – Initial grain structure of the oligocrystal specimen with IPF colors representing grain orientations relative to the sample RD direction according to the colors in the IPF triangle. Scans of top and bottom faces are shown. Scan of bottom face was flipped horizontally for ease of interpretation.....	71

Figure 4.5 – A schematic of the objective function used in optimization procedure, where x is the vector of input parameters and E is the scalar error value (output).....	79
Figure 4.6 – Measured and predicted stress-strain curves for a polycrystal, that are used for calculating corresponding error value ($E = 0.5\sigma_{FEA} - \sigma_{exp}$). The plot shows the match between two curves after the 4 unknown parameters were identified.	80
Figure 4.7 – Preparation steps that are applied in order to obtain clear images of top and bottom faces (subsequently used in reconstruction procedure).	81
Figure 4.8 – A reconstructed non-columnar voxel model of the oligocrystal specimen and its boundary conditions, also showing the finite element mesh.	83
Figure 4.9 – Prediction of the distribution of equivalent plastic strain (PEEQ) in the oligocrystal specimen. A deformation scale factor of 2 is used in order to exaggerate deformed shape, for easier visualization.	85
Figure 4.10 – Prediction of the deformed shape of the oligocrystal specimen along with the distribution of z-displacements (uz). Two cross-sectional views are shown. A deformation scale factor of 2 is used in order to exaggerate deformed shape, for easier visualization.....	86
Figure 4.11 – Surface topographies at the top and bottom faces of the specimen, extracted from simulation (marked as “sim”) and experiment (marked as “exp”) at 10% nominal strain. The absolute difference plots (marked as “ exp-sim ”) are shown, as well.	88
Figure 4.12 – Relative error between simulation and experiment at 10% nominal strain. Error of less than 2 indicates correctly predicted displacement direction.	88
Figure 4.13 – Elevation derivatives at the top face of the specimen, extracted from simulation (marked as “sim”) and experiment (marked as “exp”) at 10% nominal strain. The absolute difference plots (marked as “ exp-sim ”) are shown, as well.	90
Figure 4.14 – Elevation derivatives at the bottom face of the specimen, extracted from simulation (marked as “sim”) and experiment (marked as “exp”) at 10% nominal strain. The absolute difference plots (marked as “ exp-sim ”) are shown, as well.	91
Figure 4.15 – Evolution of average surface roughness (Sa) at the top and bottom faces of the specimen with nominal strain, extracted from simulation and experiment.	92
Figure 4.16 – Initial and final (at 10% nominal strain) structures at the top face of the specimen, extracted from simulation (marked as “sim”) and experiment (marked as “exp”).	93
Figure 4.17 – Initial and final (at 10% nominal strain) structures at the bottom face of the specimen, extracted from simulation (marked as “sim”) and experiment (marked as “exp”).	94
Figure 4.18 – Reorientation of several soft and hard grains during the experiment, in terms of change of corresponding IPF (RD) colors and of crystal lattice unit cell rotation (presented as cubes).....	96
Figure 4.19 – Reorientation of 5 of the softest grains in the oligocrystal specimen, in terms of change of corresponding IPF (RD) colors. Solid arrows represent experimental observations, dashed arrows represent model predictions.	97

Figure 4.20 – Initial and final (at 10% nominal strain) distributions of Schmid factor at the top and bottom faces of the specimen, extracted from simulation (marked as “sim”) and experiment (marked as “exp”).	98
Figure 4.21 – One of the indentation areas from the surface of polycrystal along with Schmid factor and surface elevation data extracted from the same area.	99
Figure 4.22 – Schmid factor and surface elevation data from 10 (out of 19) marked areas at the surface of polycrystal specimen.	100
Figure 4.23 – Finite element meshes and boundary conditions (L is the side of the cube) for two representative volume elements (RVEs) that were used to model the roughening behavior of a polycrystal.	101
Figure 4.24 – A comparison between experiment and model for a polycrystal: raw values of normalized roughness parameters extracted from corresponding regions in experiment (19 areas) and model (8 areas). Average values are shown as well.	102
Figure 4.25 – Surface topography and Schmid factor data, extracted from a grain and its elliptical neighborhood. Similar data is extracted from each surface grain of the polycrystalline specimen (e.g., Figs. 4.21 and 4.22).	104
Figure 4.26 – Correlations shown for circular (radius $3r$) and elliptical (semi-axes $3r$ and r) neighborhoods. Red solid line corresponds to perfect correlation; blue dots are actual observations. The elliptical neighborhood offers better correlation (variance = 0.16) than the circular one (variance = 0.49).	107
Figure A1 – Infrared images of a tube during isothermal tests, taken after necking but right before failure. Test at 15 °C is shown on the left, test at 35 °C is shown on the right.	129
Figure B1 – Intensity plot from X-ray diffraction of a deformed SS-304L specimen after failure. The microstructure has remained FCC, with no evidence of martensite forming.	131
Figure C1 – Representation of a color in the RGB space including a circle representing proximity of two colors.	133
Figure C2 – Three pairs of grains from the EBSD scans of the top and bottom surfaces (top and bottom rows, respectively).	134
Figure D1 – Crystallographic texture of as-received polycrystalline AA5052-O, shown as a set of pole figures.	135
Figure E1 – Finite element meshes of non-columnar and columnar models.	136
Figure E2 – Deformed shapes of both columnar and non-columnar models along with the distribution of z-displacements (uz). A deformation scale factor of 2 is used in order to exaggerate deformed shape, for easier visualization.	137
Figure E3 – Surface topographies for columnar/non-columnar models at the top and bottom faces of the specimen, extracted from simulation (marked as “sim”) and experiment (marked as “exp”) at 10% nominal strain.	137
Figure E4 – The absolute difference between simulation and experiment (marked as “ exp-sim ”) for both columnar and non-columnar models.	138
Figure F1 – The absolute difference between measured (DIC) and predicted strain components (Baudoin et al., 2018).	139

Figure F2 – Measured (DIC) and predicted path strain (Zhang et al., 2018).....	140
Figure F3 – Measured and predicted values of R_a (Kubo et al., 2018).....	141

LIST OF TABLES

Table 2.1. Chemical composition of the SS-304L microtubes (wt. %)	10
Table 2.2. Physical and material properties used for the numerical simulations	36
Table 4.1 – Initial grain orientations in the oligocrystal. Bunge Euler angles (φ_1 , Φ , φ_2) in degrees are listed.	72
Table 4.2 – Material parameters of AA5052-O alloy.	77
Table 4.3 – Level of agreement between predicted and measured reorientations.	95
Table 4.4 – Relations constructed for different shapes of the neighborhood.	105
Table C1 – Colors of pairs of grains at the top and bottom surfaces used in this analysis.	134

ABSTRACT

STUDY OF POST-NECKING HARDENING IDENTIFICATION AND DEFORMATION-INDUCED SURFACE ROUGHENING OF METALS

by

Paul Knysh

University of New Hampshire

This thesis covers topics at two fundamental scales at which plastic deformation is occurring – macroscopic and microscopic.

The first topic is related to the localization of deformation and subsequent necking that happens in metals during deformation, e.g., sheet metal during forming. The open fundamental question is – what happens to the material properties inside of the localized region. The localization process is very challenging to analyze, even using a conventional tension test since several effects such as material hardening as well as effects of strain-rate and temperature are strongly coupled. In this thesis we propose a novel approach that allows to decouple these effects and furthermore to identify the true hardening behavior of material. The solution is based on solving an inverse problem that involves optimization of an expensive black-box function. The methodology developed is presented in detail.

In the second topic we consider the microscopic aspects of deformation, namely grain-scale plasticity. More specifically, we apply a crystal plasticity finite element framework to analyze the deformation-induced surface roughening effect. This task also involves a number of challenges. One such challenge is the accurate calibration of the

model, which was tackled here using the black-box optimization procedure developed earlier. The second challenge is the accurate non-destructive reconstruction of a 3D texture based on images of several planar sections. The texture reconstruction problem was solved and presented as a general methodology. Subsequently it was possible to construct a comprehensive model that accounts for all major effects. It is shown that this model is able to capture the physics of deformation-induced surface roughening, however primarily in the average sense.

CHAPTER 1

INTRODUCTION

1.1. General remarks

The discovery and usage of metals by mankind was a crucial step that enabled creation of tools and weapons that were harder and more durable than previously possible. Today, thousands years later, metals and metal alloys are among the most essential structural materials, that find their applications in a wide range of industries. The manufacturing of metal parts remains a big challenge that originates from a fundamental tradeoff between weight, safety, reliability, efficiency and cost of the resultant product.

In the past several decades, owing to rapid development of computational capabilities and material science, a much better understanding of metal deformation and forming principles was obtained both on macroscopic and microscopic levels. The usage of computational modeling allowed to significantly reduce the number of time-consuming physical experiments and to focus on optimization and cost reduction of product design and manufacturing processes.

Nowadays a vast majority of modern deformation processes involve non-trivial geometries, boundary conditions and coupled physical effects that can only be analyzed numerically. The most widely used numerical technique is finite element analysis (FEA). While “kinematics” of FEA is more or less studied and established, the most complicated and challenging part of any FEA code is the material model. In terms of constructing/choosing proper material model, there exists another fundamental tradeoff – predictive power of the model versus its computational complexity.

Generally speaking, all material models can be divided into two large groups – phenomenological (macroscopic) and physical (microscopic). Phenomenological models assume the homogeneity of the media and are currently dominant in industry due to their robustness and significantly lower computational cost. Nevertheless, the accurate calibration of such models remains a difficult question. The number of model parameters often can be on the order of 10-20, and each parameter might also evolve based on deformation history. A significant number of physical experiments, sometimes non-trivial, needs to be performed in order to identify these parameters. As will be shown further, even for simplest J_2 model that can be calibrated using a single tension test, the necking formation is a big limitation that needs to be carefully resolved in order to obtain the correct hardening behavior. The situation becomes much more complex when the effects of strain-rate and temperature sensitivity are taken into account.

In contrast to phenomenological models, physics-based models attempt to capture the exact behavior of metal crystals and therefore also often called crystal plasticity models. Each single crystalline grain is assumed to deform by a set of slip systems defined by the crystal lattice structure of the material. The crystallographic orientations of grains, grain shapes and resistances to slip and twinning within the grains completely determine the mechanical response of the polycrystal. Because the morphology of every individual grain is involved and the amount of grains present is usually significant, crystal plasticity models are substantially more complex and computationally expensive than the phenomenological models. As will be shown further, even simulating a tension of a mesoscale-size specimen is a complicated task, that causes a set of computational challenges. One such challenge is an accurate reconstruction of volumetric texture from

available surface texture data. Another challenge is the accurate calibration of a crystal plasticity model. On the other hand, crystal plasticity models are valuable as they allow to better understand the underlying physics of deformation.

1.2. Thesis structure

This dissertation consists of several integral parts. More specifically, there are 3 main chapters and each chapter is based on a research study presented in a corresponding journal paper. A brief summary of each chapter is given next, highlighting the significance and novelty of each study.

[Chapter 2](#) describes a method for identifying the material hardening curves past the limit of necking in uniaxial tension and across a range of strain-rates and temperatures in a fully-coupled way. Experiments on microtubes of 304L stainless steel, which is a rate- and temperature-dependent material, were performed using a custom isothermal testing setup. Digital Image Correlation and Infrared Thermography provide full-field measurements of the strain and temperature during testing. The proposed identification procedure uses a finite element (FE) model of the experiments and the problem is cast as one of mathematical optimization. The corresponding objective function has input parameters that control the post-necking shape of the hardening curves and a scalar output that represents the proximity between the FE predictions of the force-average axial strain response and the experimental data. Since the objective function is not available in closed form and is expensive to evaluate, an efficient optimization method that requires a limited number of function evaluations is developed. The identification procedure is applied to identifying the post-necking hardening response under different

assumptions, starting from a single material curve with no rate and temperature effects included, to a family of curves with both strain-rate and temperature considered in a coupled way. To validate the family of hardening curves identified for 304L stainless steel, a fully-coupled FE model is used to simulate a conventional tension test. This model is shown to be able to reproduce this experiment, including the strain and temperature fields which develop during testing.

[Chapter 3](#) reports a robust shape interpolation procedure for constructing a voxel-based 3D model from a set of parallel 2D sections. The procedure is based on a morphing technique and is applicable to compact shapes of grains that appear in at least two consecutive sections. It relies on a set of images of the same resolution and containing the same sets of colors that correspond to different grains of the given volume. A simple demo example is followed by successful application of the procedure to reconstruct the volumetric grain structure morphology of a thin Al-Mg oligocrystal specimen from two electron-back-scatter-diffraction scans of two parallel faces. For verification purposes the same physical specimen is machined down and two interior sections, parallel to the faces, were scanned. A good matching between reconstructed and actual grain structures at these two sections is observed. As a further illustration, the 3D shapes of several grains are extracted and shown. A demonstration of reconstruction from multiple sections using a dual-phase, martensite-ferrite representative volume element is also given. Finally, a quantitative analysis of false-positive results, as well as a way to decide the applicability of this method for grain reconstruction for a given material are described.

In [Chapter 4](#) the deformation-induced surface roughening of an Al-Mg alloy is

analyzed using a combination of experiments and modeling. The behavior of a mesoscale oligocrystal that contains around 40 grains during uniaxial tension test is studied. The oligocrystal is obtained by recrystallization annealing of a AA5052-O sheet and subsequent machining, to contain one layer of grains through the thickness. A laser confocal microscope is used to measure the surface topography of the deformed specimen. A finite element model with realistic (non-columnar) shapes of the grains based on a pair of EBSD scans of a given specimen is constructed using a custom-developed shape interpolation procedure. A Crystal Plasticity Finite Element (CPFE) framework is then applied to the voxel model of the tension test of the oligocrystal. The unknown material parameters are determined inversely using an efficient 'black-box' optimizer. Based on this simulation, the following features are analyzed: deformed shape of the specimen; surface topography at top and bottom faces; corresponding elevation derivatives; evolution of the average roughness value; texture and Schmid factor after deformation; and reorientation of several soft and hard grains. The results extracted from the model correlate well with the experimental observations in the average sense, however they do not capture the exact surface elevation patterns. As an additional verification of the CPFE model, the statistics of surface roughening are analyzed by simulating uniaxial tension of the AA5052-O polycrystal and comparing it to experiments. The predictions of average roughness agree well with the experiment. Finally, using the same polycrystalline specimen, texture-morphology relations are discovered, using a symbolic Monte Carlo approach.

As can be seen from above description of chapters, the topics of this dissertation are covering both phenomenological and physics-based approaches to modeling metal

deformation processes. Two fundamental and related to each other aspects of metal deformation – strain localization (necking) and deformation-induced surface roughening – are studied in detail.

CHAPTER 2

IDENTIFICATION OF THE POST-NECKING HARDENING RESPONSE OF RATE- AND TEMPERATURE-DEPENDENT METALS¹

2.1. Introduction

The hardening curve of a material is one of the three essential ingredients of an associated-flow plasticity theory, along with the yield function and the flow-rule. The uniaxial tension test is perhaps the most common way of identifying the hardening curve. However, the test is limited by the loss of stability in the form of localization of deformation and necking. This limits the deformation that is achievable during the test, often to levels significantly below what is achievable in other deformation processes. Therefore, the proper identification of the hardening response of materials at large strains (in comparison to the uniaxial tension test) is of interest. There are two main approaches to achieve this: a) continuing to use the uniaxial tension test, due to its simplicity, but extracting additional information beyond the pre-necking stress-strain response, and b) performing a different kind of experiment that is not limited by the localization experienced during uniaxial tension. In the latter approach, experiments such as the hydraulic bulge test (e.g., [Chen et al., 2016](#), [Reis et al., 2016](#)), cylinder

¹ Published as Knysh, P. and Korkolis, Y.P., 2017. Identification of the post-necking hardening response of rate-and temperature-dependent metals. *International Journal of Solids and Structures*, 115, pp.149-160.

The optimization algorithms is published as Knysh, P. and Korkolis, Y., 2016. Blackbox: A procedure for parallel optimization of expensive black-box functions. *arXiv preprint arXiv:1605.00998*.

compression (e.g., [Lovato and Stout, 1992](#)) and stacked compression (e.g., [Coppieters et al., 2010](#)) have been used.

Focusing now in the first approach, the first well-known analytical solution of the post-necking response was obtained by Bridgman for a circular bar ([Bridgman, 1944](#)). This was later extended to a rectangular bar ([Aronofski, 1951](#)). Since then a number of analytical and numerical studies on necking in uniaxial tension have been reported ([Hill 1952](#), [Chen 1971](#), [Needleman 1972](#), [Ghosh 1977](#), [Norris et al., 1978](#), [Saje, 1979](#), [Tvergaard 1993](#)). Furthermore, a variety of optical techniques have been used to probe the strain fields inside the neck including Moiré ([Theocaris and Marketos, 1967](#), [Cordero et al., 2005](#)) and speckle pattern interferometry ([Petit et al., 2014](#)).

To extract post-necking material properties using the uniaxial tension test, a number of methods were developed. They can be divided into two broad groups – explicit and implicit. Explicit methods are based on extracting strain fields directly from the necking region using full-field measurement techniques such as Digital Image Correlation (DIC). For example, ([Coppieters et al., 2011](#), [Coppieters and Kuwabara, 2014](#)) proposed to equalize the external work (which comes from total force and elongation) and internal work (which can be quantified from the strain fields obtained from DIC and the adoption of a material model) and thus determine the stress field in the neck. The Virtual Fields Method (VFM) used by [Kim et al., 2013](#) (originally proposed in [Pierron et al., 2000](#)) and another explicit technique proposed by [Wang and Tong \(2015\)](#) are based on similar idea.

Implicit methods are using finite element analysis (FEA) to iteratively update the post-necking hardening curve, until the FEA results are matching experimental data. In

most studies, the goal is to match post-necking force-displacement data ([Zhang and Li, 1994](#), [Ling, 1996](#), [Zhang et al., 1999](#), [Koc and Stok, 2004](#), [Joun et al., 2008](#), [Peirs et al., 2011](#), [Tardif and Kyriakides, 2012](#), [Kamaya and Kawakubo, 2014](#)). An alternative goal is to match the strain distribution in the neck region (measured experimentally) as in the work of [Scheider et al. \(2004\)](#). The combination of these two goals is considered in [Kajberg and Lindkvist \(2004\)](#) and [Gross and Ravi-Chandar \(2015\)](#).

Some advantages that the implicit methods appear to have over the explicit ones are the following. Usage of FEA makes them independent of strain measurements, which can be performed only at the surface of the specimen. Also, implicit methods don't always require the extraction of full-field strain fields from the neck region, if only force-displacement data is to be matched. Finally, advanced yield functions may already be available in the FE codes.

Since necking is also associated with a rapid change in strain-rate and temperature due to deformation-induced heating (e.g., [Knysh and Korkolis, 2015](#)), both effects should be addressed, as for example in [Johnson and Cook \(1983\)](#). A specialized version of such relation for 310 stainless steel was developed in [Lin and Wagoner \(1986\)](#). More recent studies were done for AL-6XN austenitic stainless steel ([Nemat-Nasser et al., 2001](#)) and for Ti-modified stainless steel ([Mandal et al., 2009](#)). An experimental study on metal sheets for a variety of strain-rates and temperatures was reported by [Rusinek and Klepaczko \(2001\)](#).

In this work, a procedure for identifying the material hardening curves in the post-necking range, and across a range of strain-rates and temperatures is proposed. The experiments on 304L stainless steel are described first, including a simple but very

efficient method of performing isothermal tension tests. Subsequently, the hardening identification procedure is described, including a FE model of the experiments and the objective function and search algorithm used for the optimization. Two examples illustrate the framework developed. Finally, this is applied to the experiments on the 304L stainless steel. The hardening curves of the material are identified under a variety of assumptions, starting from the rate- and temperature-independent model and concluding with the fully-coupled approach.

2.2. Experiments

a. Material properties and experimental setup

The material that was selected for our experiments is 304L stainless steel in the form of tubes of 2.4 mm outside diameter and 0.16 mm wall thickness. This material is both rate- and temperature-dependent, as was also revealed in the experiments reported below. The tubes were drawn-over-mandrel by the manufacturer and were received in the fully-annealed state. The chemical composition of the material is given in [Table 2.1](#).

Table 2.1. Chemical composition of the SS-304L microtubes (wt. %)

C	Mn	P	S	Si	Ni	Cr	Al	Fe
0.015	1.43	0.029	0.008	0.4	10.85	18.67	0.003	Balance

The uniaxial tension experiments were performed with the mesoscale tensile stage manufactured by Psylotech, Inc. ([Ripley and Korkolis, 2015](#)). The stage is capable of +/-

2000 N axial force, with 10 mN resolution, and has 50 mm available stroke. The tubes were held using a modified hydraulic fitting to grips with self-aligning spherical bearings, so that no moment was allowed to develop. During testing, the strain was measured using the full-field 2D Digital Image Correlation (DIC) method. The images were acquired using a 2.0 MPixel Point Grey Research GRAS-20S4M-C camera with 35 mm Schneider-Kreuznach Xenoplan lenses. The images were post-processed with the commercial DIC software VIC-2D. The software includes a virtual extensometer feature, which was used to determine the engineering strain over a 10 mm gage-length. At the same time, the temperature field was acquired using a FLIR SC-645 Infrared Camera with temperature resolution of 0.05 °C and range of -20 to +150 °C. A photograph of the experimental setup is shown in [Fig. 2.1](#).

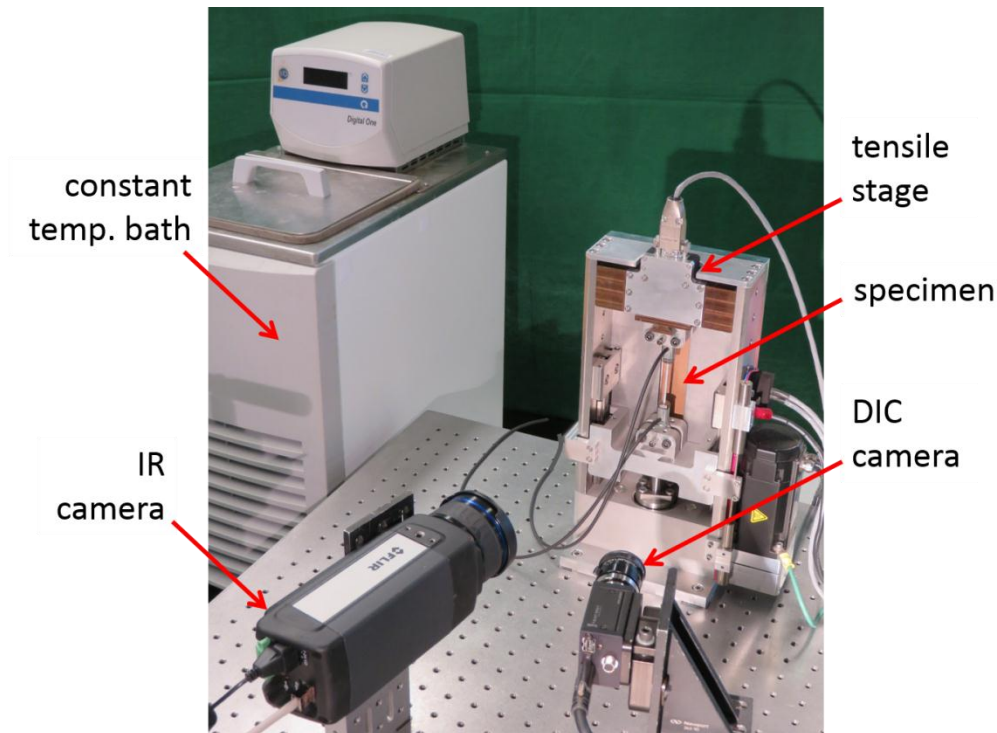


Figure 2.1 – Setup for conventional and isothermal tension experiments and its components.

The uniaxial tension experiments were performed under velocity-control. The total length of the tubes was 64 mm, with the distance between the two grips being 30 mm. The velocities were varied between 3 $\mu\text{m/s}$ and 3 mm/s, resulting in constant (nominal) strain-rates in the gage-length of 10^{-4} , 10^{-3} , 10^{-2} and 10^{-1} s^{-1} , respectively. Beyond these “conventional tension tests”, isothermal tension tests were performed by connecting the grips to a Neslab RTE 740 constant-temperature bath and circulating water through the tubes during tensile loading. This is an evolution of the isothermal testing method proposed earlier by [Cullen and Korkolis \(2013\)](#), adapted here to tubular specimens. Isothermal tension tests were performed at 15, 25 and 35 °C, and across the same range of strain-rates as the conventional tension tests. As will be shown later, this is a particularly effective and easy method for performing an isothermal test in the temperature range of interest.

b. Results from conventional tension test

The nominal stress-strain responses obtained during the conventional tension tests at 4 different strain-rates are shown in [Fig. 2.2](#). The 304L stainless steel material of the microtubes is seen to have very large ductility, with the elongation-to-fracture of the quasistatic tests (e.g., strain-rate of 10^{-4} s^{-1}) approaching 70%. At the same time, the initial parts of the responses cascade as expected, with the flow stress increasing as the strain-rate is increased. However, at higher strains, the responses are seen to cross over each other, with the higher strain-rates failing earlier than the rest. This is in agreement with earlier work by the authors ([Cullen and Korkolis, 2013](#)) and is a direct consequence of deformation-induced heating and the establishment of a temperature

gradient along the gage-length (e.g., Cullen and Korkolis, 2013 and the references therein).

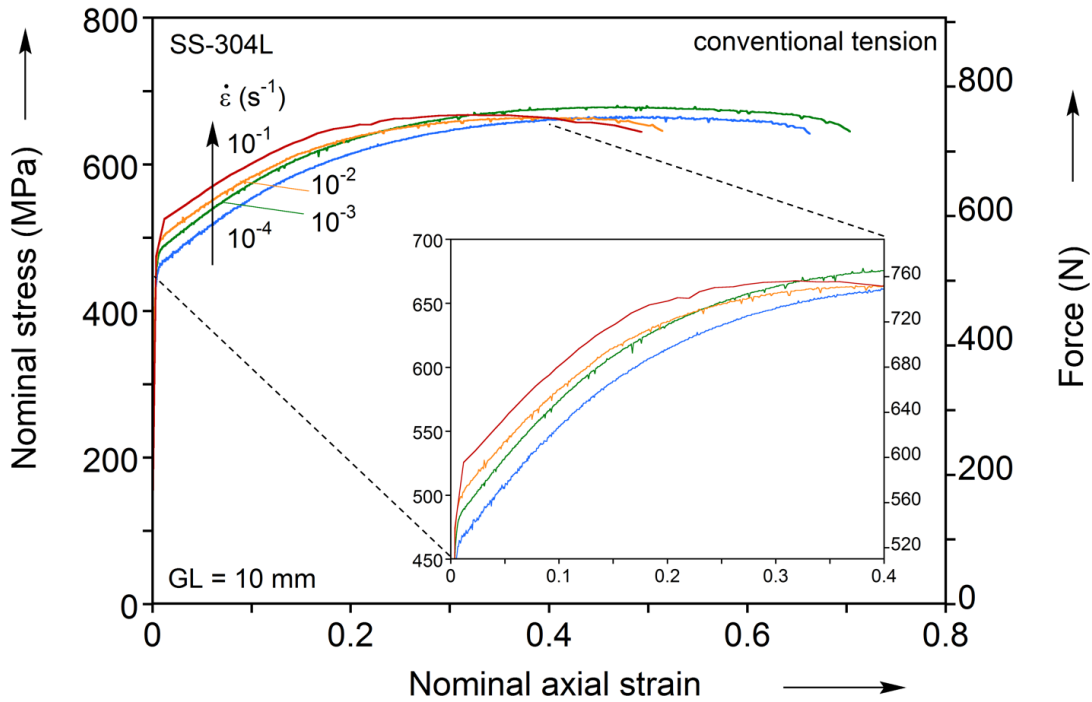


Figure 2.2 – A set of conventional tension tests performed at different strain-rates.

The full-field strain and temperature measurements that the DIC and IR systems afford illustrate this effect. In Fig. 2.3, both fields are presented *vis-a-vis*. While the axial strain is seen to be uniform, a temperature gradient is detected. This is because the main mechanism of heat-transfer in this problem is conduction to the cold grips (which are seen to remain at ambient temperature during the test, see Fig. 2.3). The temperature gradient acts as an imperfection that triggers an earlier localization of deformation than in the corresponding isothermal case. Increasing the strain-rate intensifies this gradient, with detrimental effects to the apparent elongation-to-fracture, as can be seen in Fig. 2.2.

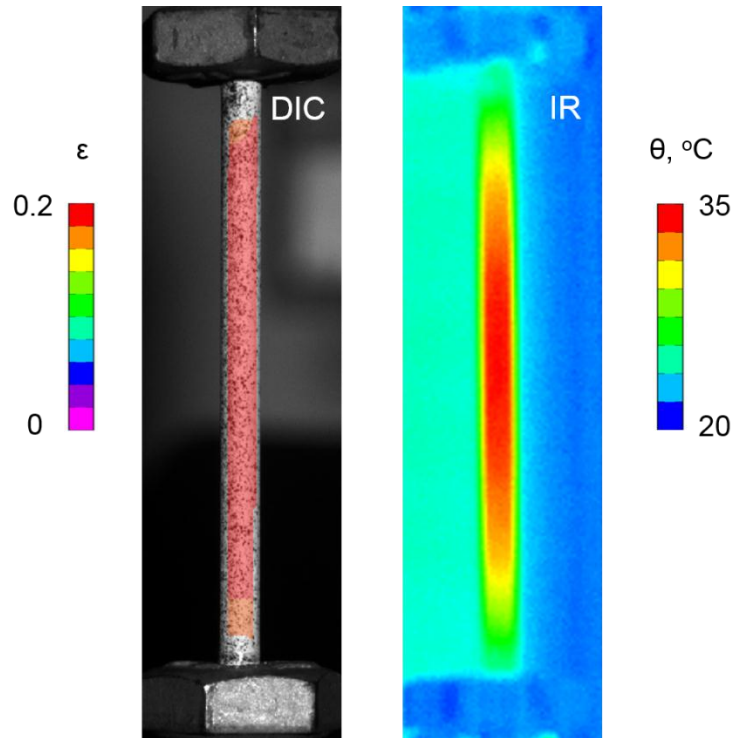


Figure 2.3 – Axial strain and temperature fields extracted from DIC and IR cameras.

The net conclusion of the results of [Figs. 2.2 and 2.3](#) is that these tests cannot be used for material characterization, as the mechanical and thermal effects are intertwined. This motivated the creation of the isothermal tension tests described in this and earlier ([Cullen and Korkolis, 2013](#)) work.

2.3. Hardening identification procedure

Assuming now that the mechanical and thermal effects are decoupled, the strategy to identify the post-necking hardening response of the material will be the following: a) isothermal experiments will be performed at various strain-rates and temperatures, b) a FE model of these experiments will be created, c) a family of post-necking hardening curves (i.e., at different strain-rates and for given constant temperatures) will be

introduced in the FE model, d) since necking is an instability, the post-necking structural response predicted by the FE model will be compared to the one measured experimentally, and e) the input hardening curves will be iteratively adjusted through an optimization procedure, until the agreement of the structural responses is found within a pre-set tolerance.

While this identification procedure has been used extensively in the past (e.g., [Korkolis and Kyriakides, 2008a, 2008b, 2009, 2010, 2011](#), [Luo and Wierzbicki, 2010](#), [Cullen and Korkolis, 2013](#), [Dick and Korkolis, 2014, 2015](#)), because of the rate- and temperature-dependence of the 304L stainless steel, it has to be performed in a coupled fashion across the strain-rates and temperatures of interest. In other words, it is not sufficient to match the experiments one-by-one. Necking involves an increase in the strain-rate and the temperature gradient, which requires that the entire family of input hardening curves must be adjusted simultaneously to yield predictions that fit the entire family of experiments. This an arduous and expensive task, that has not been reported before, and which led to the development of a computationally effective search algorithm presented in [Knysh and Korkolis \(2016\)](#) and summarized below.

a. Finite element model

The finite element model of the tube was built in the non-linear code Abaqus/Standard. An associated flow-rule using the von Mises yield surface as the plastic potential is adopted in this work:

$$d\varepsilon_{ij}^p = d\lambda \frac{\partial f}{\partial \sigma_{ij}} \quad (2.1)$$

where ε_{ij}^p are the plastic strain tensor components, σ_{ij} are the stress tensor

components, λ is the hardening parameter and f is the von Mises plastic potential:

$$f = J_2 - k^2 \quad (2.2)$$

where k is the material constant and J_2 is the second invariant of deviatoric stress tensor s_{ij} :

$$J_2 = \frac{1}{2} s_{ij} s_{ij} \quad (2.3)$$

The hardening curves were input either individually (for rate- and temperature-independent models) or as a cluster across strain-rates and temperatures. When multiple hardening curves are input to the model, the software interpolates linearly between them for the current flow stress and tangent modulus per integration point.

The finite element model that was used in this work is shown in [Fig. 2.4](#). Taking advantage of the symmetries present, an axisymmetric model of half of the tube was created. Note that at the final moments before rupture the axisymmetry is broken, however this occurs significantly after the limit-load instability that is associated with the onset of necking. Beyond that, the model replicates the actual geometry used in the experiments very accurately, as it will be used to match the post-necking structural responses. Recall that in the experiments the gage-length from which results are reported was controlled as accurately as possible.

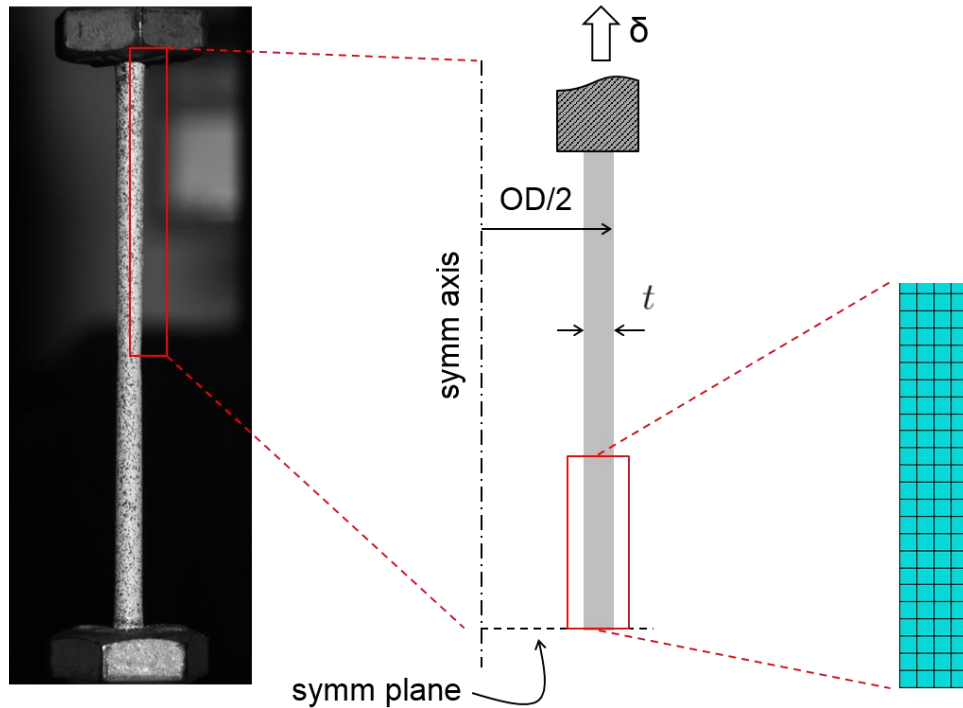


Figure 2.4 – Axisymmetric FE model of a tube with boundary conditions and FE mesh shown.

An isotropic mesh of 1,500 axisymmetric elements with reduced integration (CAX4R) was used, after a sensitivity study demonstrated that it captured the physics of the process at a reasonable computational cost. The end of the tube is clamped so that no rotation or radial displacement is allowed. At the clamped end, the axial displacement (velocity in case of rate-dependent simulation) is prescribed, replicating the displacement-control used in the experiments. A geometric imperfection in the form of a circular arc that creates a change in the thickness of ($10^{-4} \times t$) is introduced, to ensure that necking will happen at the center of the tube.

Because of the nature of the conventional tension tests, a coupled thermomechanical FE model (using CAX4RT elements) was also created. In this case, thermal boundary conditions need to be assigned, as described in [Section 2.4b](#).

b. Objective function

The objective function used for the optimization represents the proximity between the FE predictions and the experiments. An outline of how the objective function is computed is given in Fig. 2.5a. A family of hardening curves at different temperatures and strain-rates is used as input to isothermal finite element models, described in the next section. The structural responses of these models, in the form of the force-average axial strain curves, is compared to the ones from the isothermal experiments. The error between the two is computed as the integral of the absolute difference between the two curves and serves as the objective function for the optimization procedure discussed in Section 2.3c. This environment is created using the Python language.

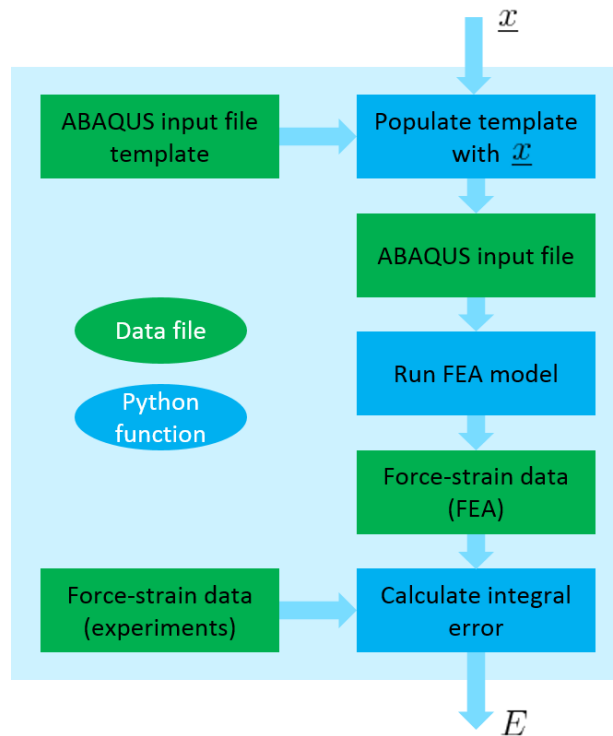


Figure 2.5a – A schematic of the black-box objective function, where \underline{x} is the input vector and E is the output error (scalar).

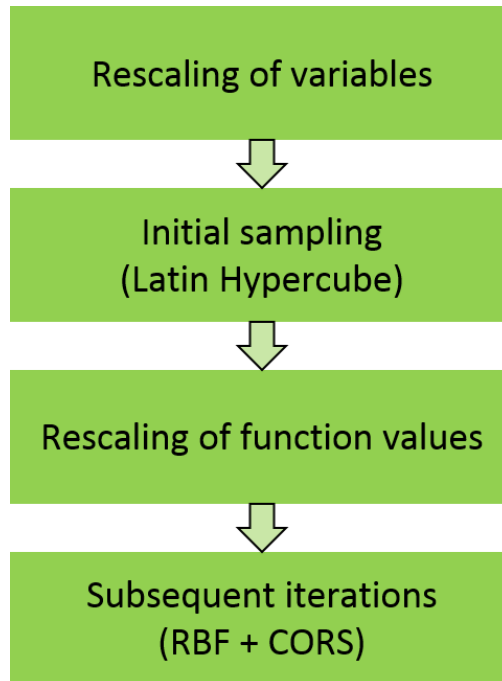


Figure 2.5b – A schematic of the procedure for optimizing expensive black box functions.

c. Optimization procedure

Different techniques can be used for the optimization task. Some common choices are: Gauss-Newton-like methods (Koc and Stok, 2004), generalizations of simplex method (Kajberg and Lindkvist, 2004), genetic algorithms (Gross and Ravi-Chandar, 2015) and others.

Because in this case a FE model is involved, the corresponding objective function is expensive to evaluate and has an implicit nature (i.e., no information on the function itself is available a-priori). A class of methods that is designed to efficiently optimize such expensive black-box functions is based on the response surface methodology (Box and Wilson, 1951). This methodology replaces the real objective function with a fit (termed the “response surface”) that is built with only few function evaluations, and that is much cheaper to optimize. Unlike other methods, beyond requiring much fewer

function evaluations, this methodology does not need information on gradients and is less likely to be trapped in local optima.

Let $s_n(\underline{x})$ be a response surface that estimates the value of the objective function for an arbitrary point \underline{x} using n sampled points. In this work, we modify the Radial Basis Functions (RBF) with cubic basis ([Holmström, 2008](#)) to use as the response surface:

$$s_n(\underline{x}) = \sum_{i=1}^n \lambda_i \varphi(\|\underline{T}(\underline{x} - \underline{x}_i)\|) + \underline{b}^T \underline{x} + a \quad (2.4)$$

where $\varphi(r) = r^3$. In this expression, the difference between an arbitrary point \underline{x} and the n known vectors \underline{x}_i at the sampled points is computed, and then scaled by the linear operator \underline{T} , which is the modification of RBF that is introduced in this work (see [Knysch and Korkolis, 2016](#)). The Euclidian norm is used to determine the distances. The values of the function φ are calculated, and then weighted with λ_i and summed. In addition, $s_n(\underline{x})$ contains a linear part, controlled by a and \underline{b} .

The optimization procedure consists of 4 main steps:

1) Rescaling of variables. Since it is possible that the components in the input vector \underline{x} are of different orders of magnitude, they are scaled to the $[0, 1]$ interval, to facilitate proper calculation of distances in [Eq. \(2.4\)](#).

2) Initial sampling. The values of the function at an initial set of \underline{x}_i are determined. While a uniform mesh would be a natural option, the number of function evaluations would grow geometrically with mesh refinement. Instead, we opted to build a Latin Hypercube ([McKay et al., 2000](#)), to fill the parameter space in a uniform way for any given number of sampled points.

3) Rescaling of function values. During evaluations of the function, it is possible to generate outliers. These are removed, and the remaining function values are normalized into $[0, 1]$ for ease of interpretation.

4) Subsequent iterations. The search for the global optimum is performed using a modified CORS algorithm (Regis and Shoemaker, 2005). In our approach, at every iteration we seek the optimum of the current $s_n(\underline{x})$, with the constraint that the corresponding \underline{x} cannot lie within a radius r of the existing points \underline{x}_i . The point \underline{x} thus discovered is then added to the set of \underline{x}_i , the response model $s_n(\underline{x})$ is updated and the process is repeated, with a radius r that decreases in every iteration (Knysh and Korkolis, 2016). This prevents the procedure from being trapped in a local optimum.

To further accelerate the procedure, multi-core CPUs are used by dividing the function evaluations into batches, with the size of the batch equal to number of cores available. These batches are then evaluated in parallel way.

An outline of the optimization procedure is given in Fig. 2.5b.

d. Application examples

Two examples of the optimization procedure described above are discussed here. In the first case, the method is applied to a known and simple objective function so that the result can be easily verified. The following function of two variables is adopted:

$$f(x, y) = (x - y - 0.25)^2 + (x - 0.5)^2, \quad 0 \leq x, y \leq 1 \quad (2.5)$$

Contours of this function on a unit square are shown in the left plot in Fig. 2.6 along with its global minimum at $x = 0.5, y = 0.25$ identified with a red dot. Assume now that

the analytical expression (Eq. (2.5)) is not known, but it is possible to evaluate the function at discrete points (x, y) , thus imitating the black-box function. The result of applying the optimization algorithm to detect the global minimum is shown in the right plot in Fig. 2.6. Only 10 function evaluations were necessary and are marked in that plot as black dots. As can be seen from the contours, the RBF model is able to properly reconstruct a given function and accurately identify its minimum.

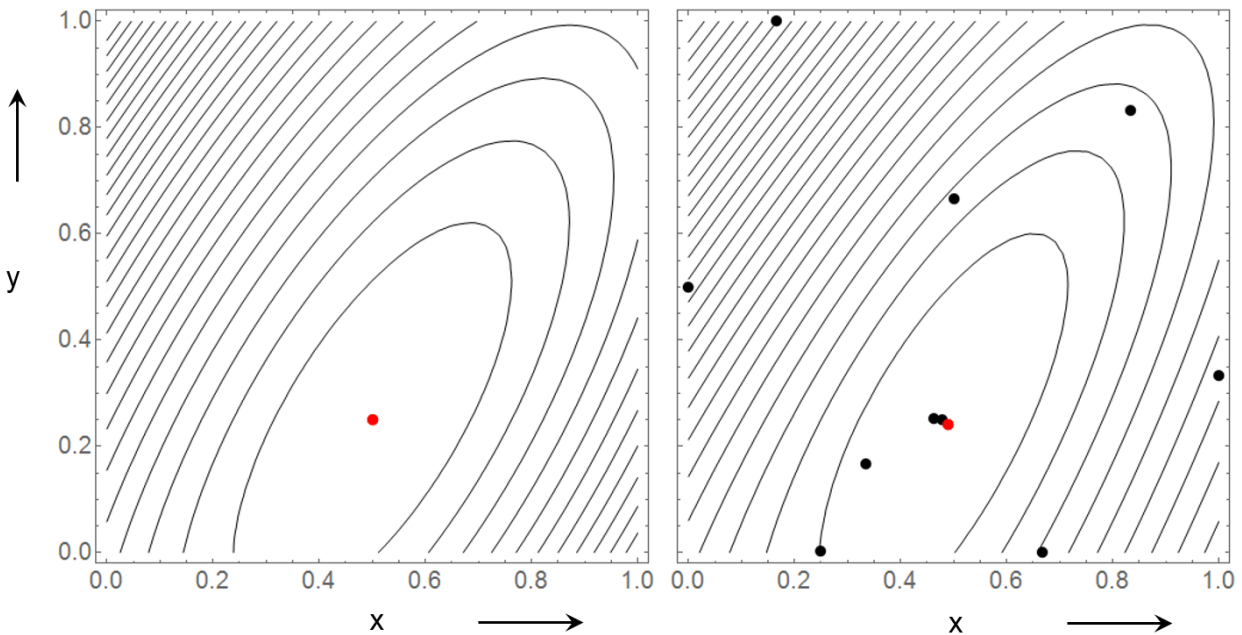


Figure 2.6 – Example of applying the optimization procedure. Left figure shows original isolines of $f(x,y)$; right figure shows isolines reconstructed using 10 function evaluations (black dots). Red dots show exact and estimated minimum.

In the second example, the proposed method is applied to post-necking hardening identification, but using a single experiment as input, and neglecting the rate- and temperature-dependence of the material. An isothermal uniaxial test on a SS-304L tube performed at 25 °C is used as the experiment. The material hardening curve is known until necking (plastic strain of 0.3) and is modeled with a cubic function of the form $ax^3 + bx^2 + cx + d$ (where $x = \varepsilon^p$) in the post-necking region (plastic strain 0.3-1).

The use of a cubic function guarantees a smooth result without excessive numerical noise. Alternatively, one can use a linear combination of the Swift and Voce hardening laws (e.g., [Sung *et al.*, 2010](#), [Coppieters and Kuwabara, 2014](#), [Mohr and Marcadet, 2015](#)). In addition to C^0 -continuity at plastic strain of 0.3, two variables are introduced to control the shape of post-necking part (see [Fig. 2.7a](#)): u_1 is the slope of the curve at plastic strain of 0.3 and u_2 is the value of stress at plastic strain of 1. Furthermore, it is assumed that the curvature at plastic strain of 1 is zero, which implies that the curvature is of the same sign between plastic strains of 0.3 and 1, so that the hardening curve is either convex or concave in that interval. [Figure 2.7](#) shows the result of applying the optimization algorithm with 32 function calls. The optimal shape of the post-necking material curve is shown in [Fig. 2.7a](#) and the corresponding matching of the force-average axial strain data between experiment and analysis is shown in [Fig. 2.7b](#). Finally, the estimated error as a function of u_1 and u_2 (normalized) is given in [Fig. 2.7c](#). It can be seen that the procedure started with scanning (in a Latin Hypercube sense) the entire solution domain and gradually identified the region of low values of error. Subsequently, it scanned that region with a higher resolution, until the global minimum was identified. Finally, note that the variable u_1 was introduced here as a free parameter only to verify that its optimal value, as found by the identification procedure, matches its actual value. In other words, that there is no kink present in the hardening curve identified.

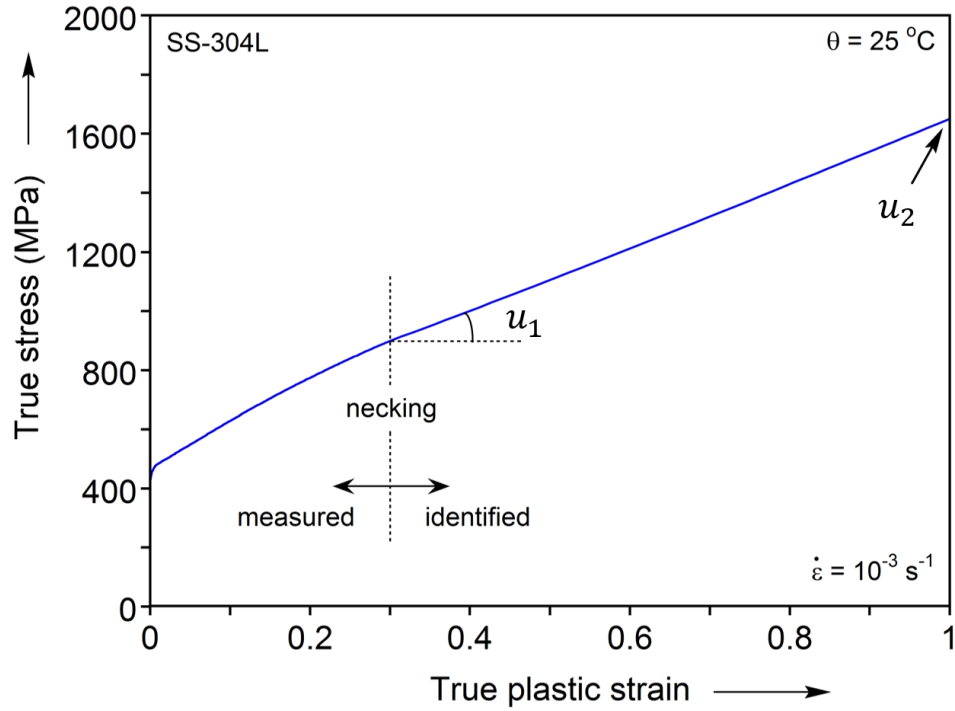


Figure 2.7a – An identified input curve that has its post-necking part represented with 2 shape parameters (u_1 , u_2).

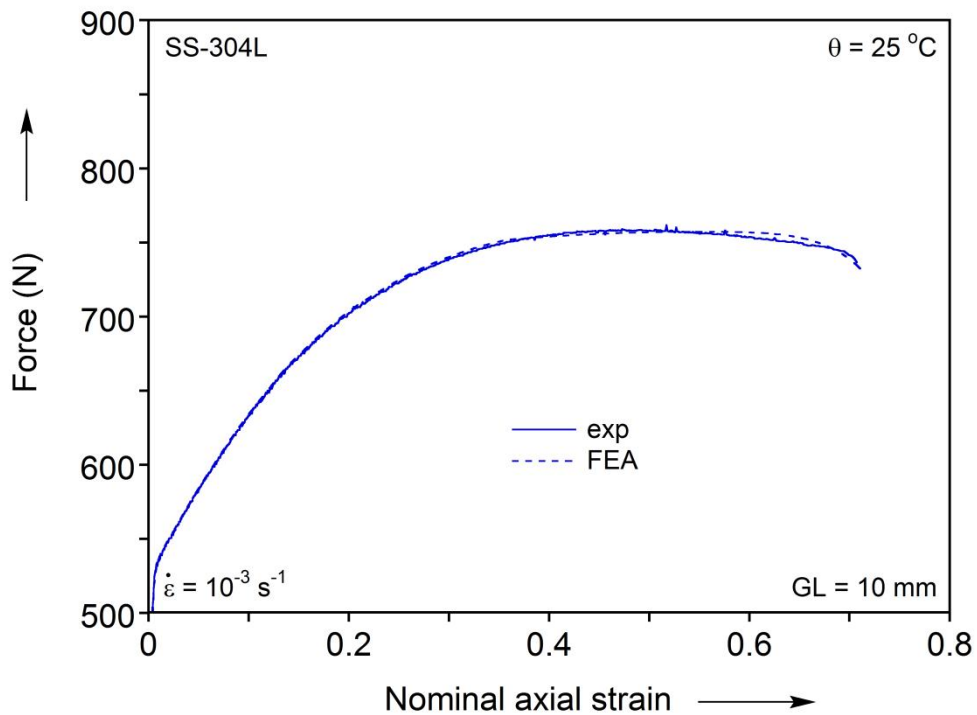


Figure 2.7b – The matching in force-average axial strain response between FEA and experiment. Corresponds to the identified input curve of Fig. 2.7a.

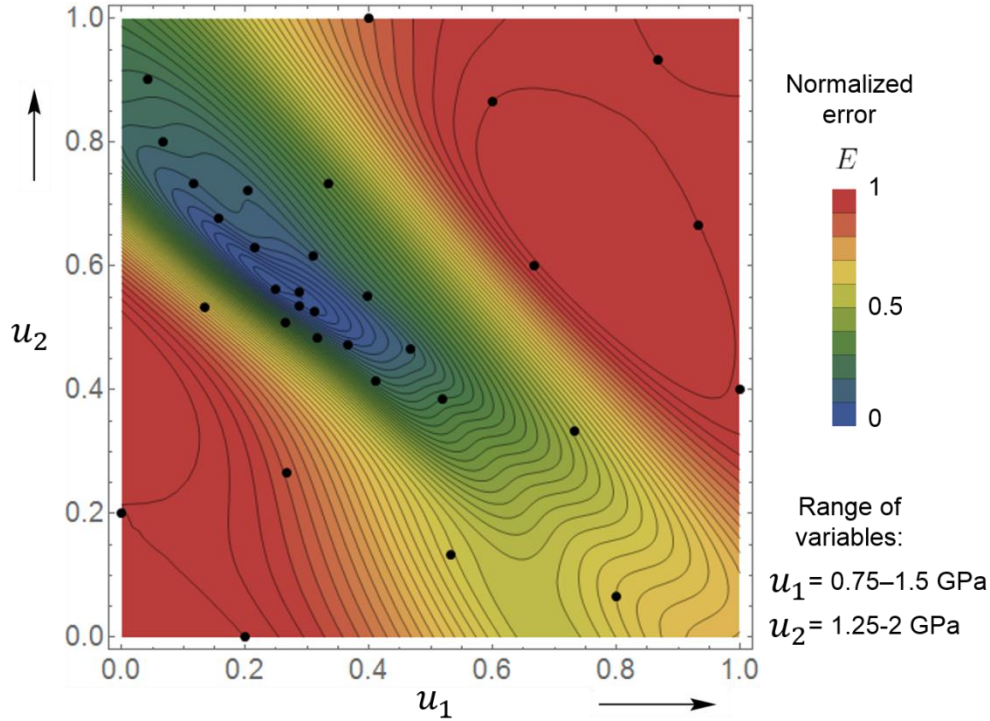


Figure 2.7c – The error function that corresponds to Fig. 2.7a and b, reconstructed with 32 function evaluations. Ranges of u_1 , u_2 and error values are normalized to $[0, 1]$.

In summary, both examples demonstrate that the proposed optimization procedure accurately identifies the optimum with a limited number of function evaluations.

2.4. Results and discussion

a. Post-necking hardening response of 304L stainless steel

In this section, we apply the procedure described in Section 2.3 to identify the post-necking hardening response of SS-304L under different sets of assumptions.

Assuming at first that the material is rate- and temperature-independent (R&TI), the corresponding post-necking identification becomes as simple as finding a single hardening curve that provides an acceptable agreement of the force-average axial strain data between experiments and FEA for a given conventional test. For a material

that is rate- and temperature-dependent (R&TD, such as the SS-304L used in this work) such identification, while it is not physical, can still be mechanistically applied. The resulting post-necking hardening curve is shown in [Fig. 2.8a](#) and the corresponding matching of the force-average axial strain data from a conventional experiment (at a strain-rate of 10^{-3} s^{-1}) is shown in [Fig. 2.8b](#). From these two plots, it can be deduced that even though the agreement of the structural response between the experiment and the FEA is excellent, the hardening curve identified has an unnatural inflection point at 0.3 strain, changing from concave-down to convex. We have no physical basis (e.g., a phase transformation) to substantiate this finding. On the other hand, we can explain this increased work-hardening rate as follows. During necking, the strain-rate and the temperature both increase inside the neck, with the former making the material harder to deform and the latter making it softer. Since the temperature effect here is modest in comparison to the rate effect, the post-necking part of the response is the result of the hardening of the material inside the neck due to the increased strain-rate. Since the R&TI model is only provided with a single input curve, that curve shows an increased work-hardening rate to allow the matching of the experimental structural response.

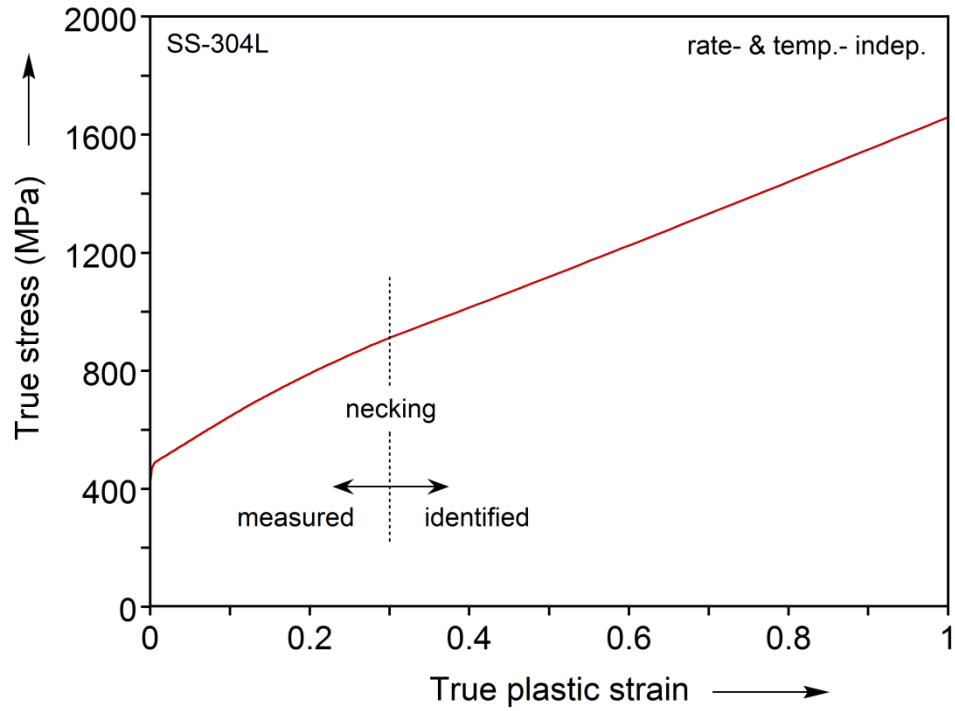


Figure 2.8a – Identified input curve for the case when rate and temperature effects are not taken into account.

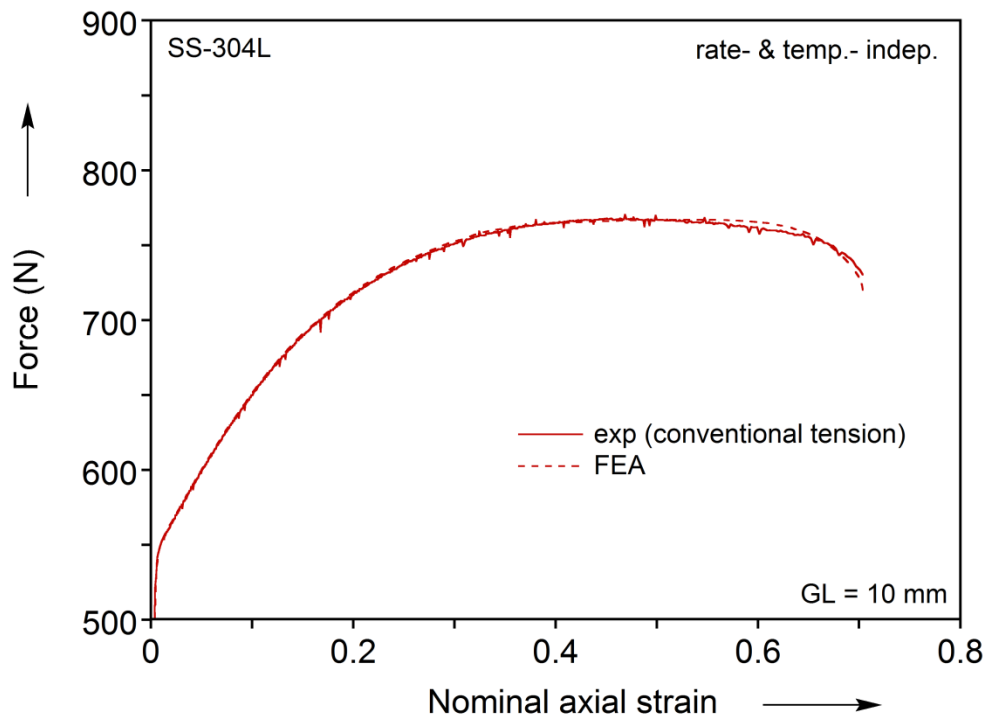


Figure 2.8b – The matching in force-average axial strain response between FEA and experiment that corresponds to the identified input curve in Fig. 2.8a.

Results that are more meaningful can be obtained if we use the same R&TI model along with a set of isothermal tests that are performed at fixed temperatures and different strain-rates. In this case, a different post-necking curve is going to be identified for each temperature (which essentially takes the temperature effect into account). Still, usage of the rate-independent model means that we won't be able to capture the rapid change in strain-rate that happens from the onset of necking and onwards. This change in strain-rate can be substantial (up to 10 times higher than the nominal strain-rate of the test). Identification for a set of isothermal tests at 25 °C and at different strain-rates was performed. The resulting post-necking hardening curves are shown in [Fig. 2.9a](#), corresponding to the force-average axial strain data shown in [Fig. 2.9b](#). The same conclusions as earlier can be drawn: while the force-average axial strain data has been matched perfectly, the identified hardening curves still exhibit a steady, if not increasing rate-of-hardening, that is not supported by physical mechanisms such as stage III hardening ([De Almeida *et al.*, 1984](#), [Meyers and Chawla, 1984](#)) and the absence of a phase transformation.

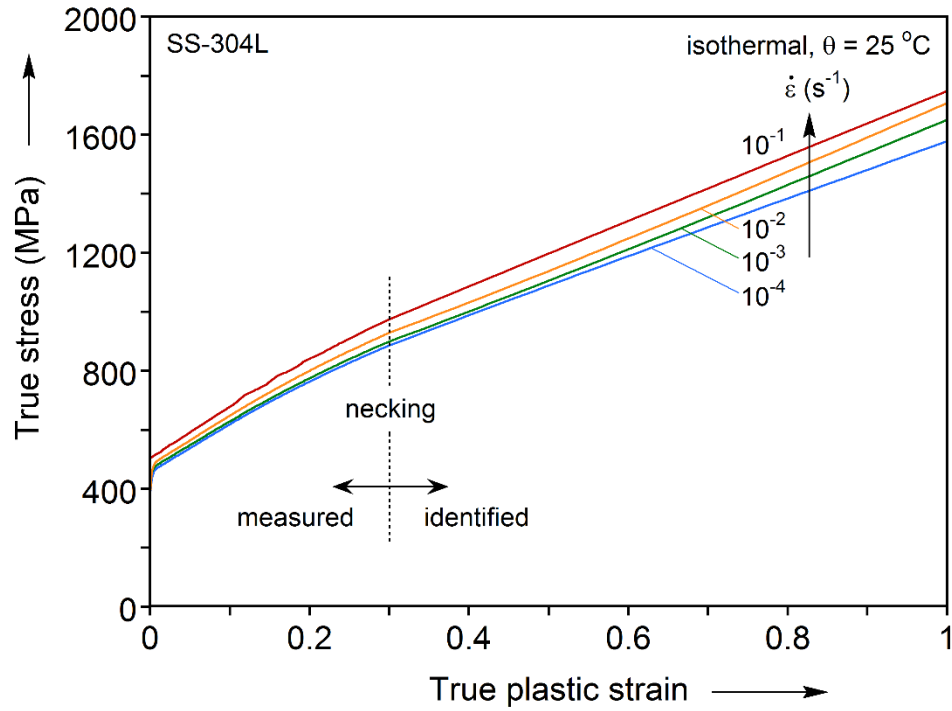


Figure 2.9a – Identified input curves for a constant temperature (25 °C). Rate effect is not taken into account.

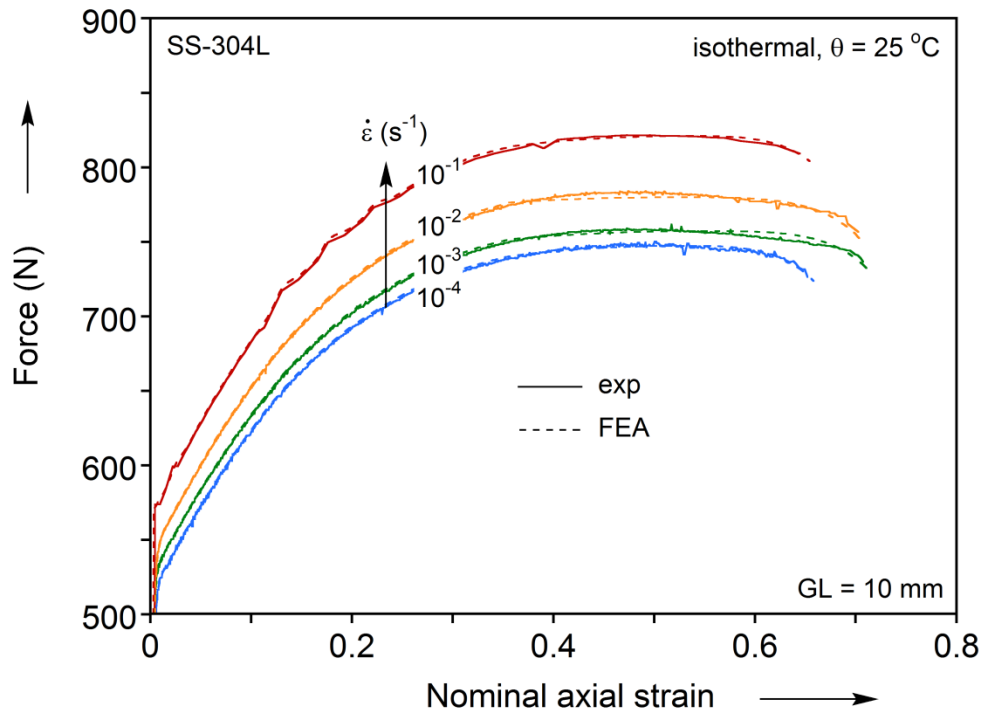


Figure 2.9b – The matching in force-average axial strain response between FEA and experiments that corresponds to the identified input curves in Fig. 2.9a.

Finally, we include the both the temperature and rate effects in our model. As was mentioned above, the strain-rate in the neck region is up to 10 times higher than the nominal strain-rate of the test. This suggests that the strain-rates used in the experiments should not be more than an order of magnitude different from each other. Therefore, a strain-rate sequence of 10^{-4} , 10^{-3} , 10^{-2} and 10^{-1} s^{-1} was used in this work. The matching of the force-average axial strain data was pursued for all tests except for the fastest one, because the strain-rate in the neck for this case is even higher, and therefore not possible to consider. Still, the hardening curve identified for the fastest test is not “arbitrary”, in the sense that it indirectly affects the force-average axial strain response of the second-fastest test.

In this case, all hardening curves are coupled and therefore must be provided to the FE model all at once, as well as adjusted simultaneously. From the optimization point of view, this means that more variables (in comparison to previous analysis) have to be introduced. Even though only one variable was used in this work to control the shape of each hardening curve (shown as u_2 in [Fig. 2.7a](#)), a 4D optimization problem had to be solved. However, the procedure described in [Section 2.3](#) is able to find the optimum set of hardening curves with only about 100 function calls (which are shown as black dots in [Fig. 2.7c](#), for a simpler problem with only two free variables). The post-necking hardening curves identified are shown in [Figs. 2.10a, 2.10c and 2.10e](#) for 3 different isothermal testing temperatures. The corresponding force-average axial strain data from the experiments and the FEA are shown in [Figs. 2.10b, 2.10d and 2.10f](#). In this case, while the force-average axial strain data continue to show excellent fits, the identified hardening curves have a continuously dropping hardening-rate, as expected.

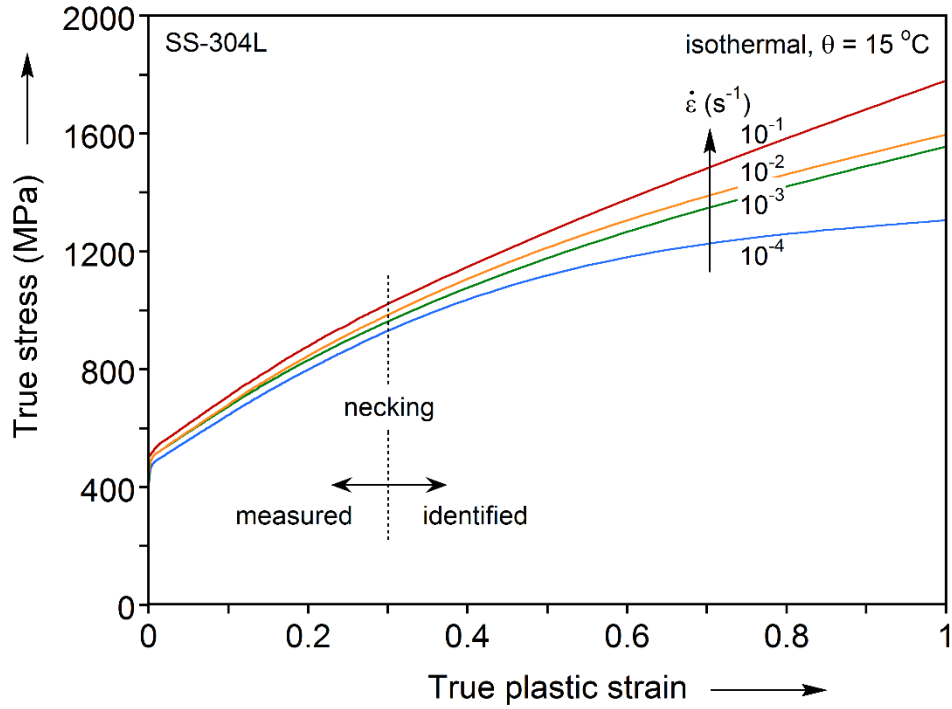


Figure 2.10a – Identified input curves for a constant temperature (15°C). Both rate and temperature effects are taken into account.

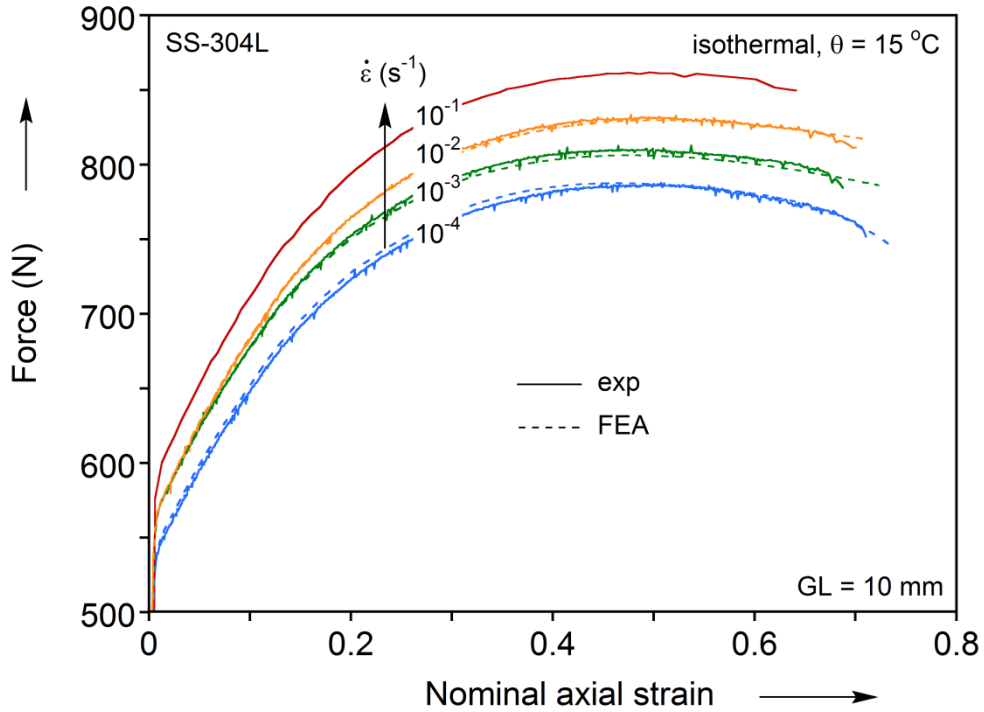


Figure 2.10b – The matching in force-average axial strain response between FEA and experiments that corresponds to the identified input curves in Fig. 2.10a.

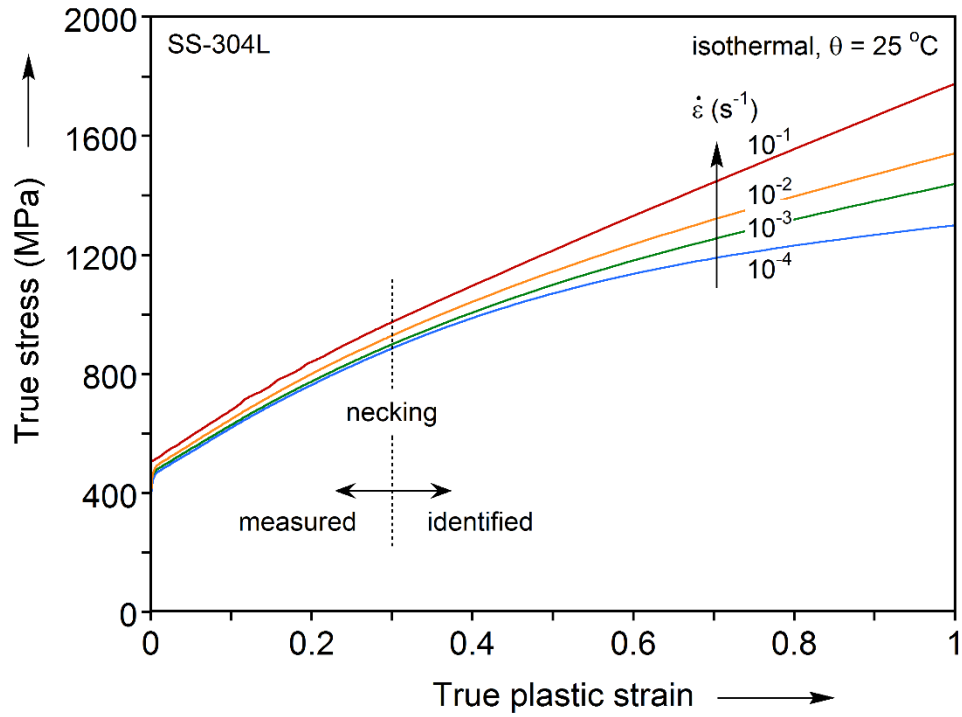


Figure 2.10c – Identified input curves for a constant temperature (25 °C). Both rate and temperature effects are taken into account.

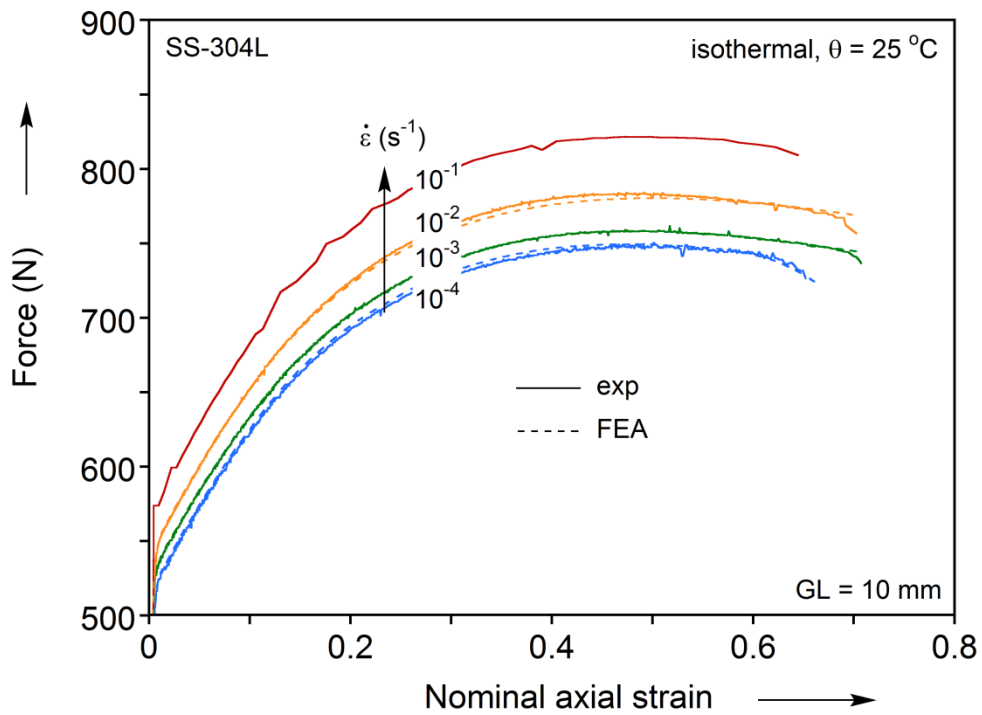


Figure 2.10d – The matching in force-average axial strain response between FEA and experiments that corresponds to the identified input curves in Fig. 2.10c.

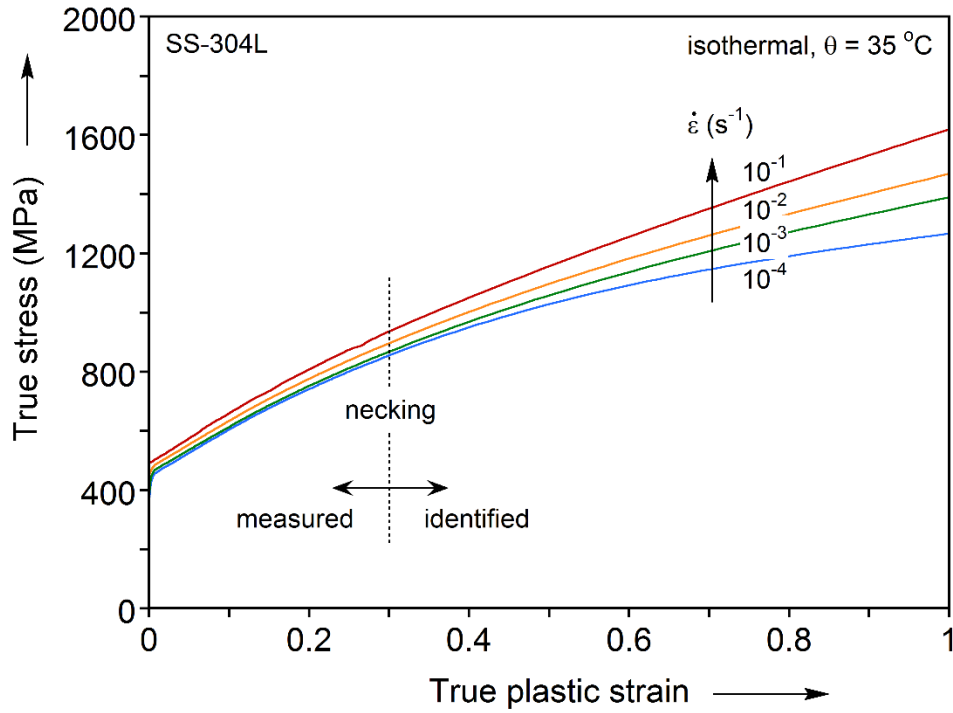


Figure 2.10e – Identified input curves for a constant temperature (35 °C). Both rate and temperature effects are taken into account.

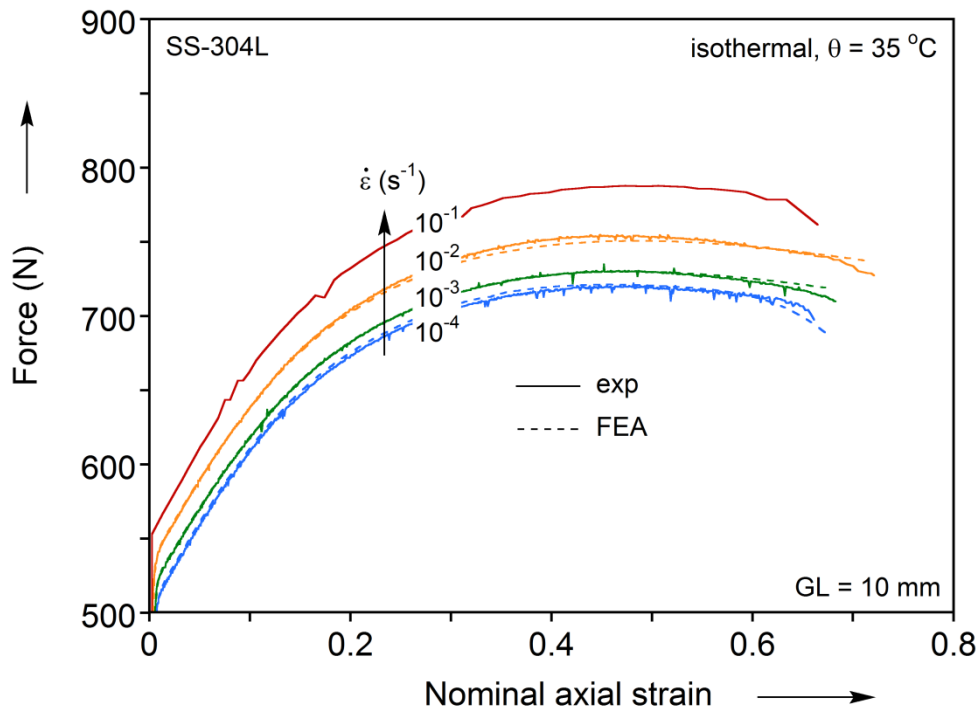


Figure 2.10f – The matching in force-average axial strain response between FEA and experiments that corresponds to the identified input curves in Fig. 2.10e.

The predictions under the R&TI and RI assumptions lead to stiffer hardening curves, as was explained earlier in this section. The predictions of the fully-coupled analysis show a monotonic decrease of the hardening rate, as purported by microstructural considerations.

b. Predictions of conventional tension of 304L stainless steel

The post-necking hardening curves that were identified in [Section 2.4a](#) can be used to model a complex material deformation process that develops large strains and takes place over a range of strain-rates and temperatures. As a verification of the curve identified, we now use them to model a conventional tension test, where deformation-induced heating occurs (see [Figs. 2.3 and 2.16](#)), using a fully-coupled thermomechanical FE model.

The fully-coupled FE model has the same geometry as the one discussed in [Section 2.3](#). All hardening curves identified in [Section 2.4a](#) are provided to the model. The additional physical parameters that are needed for the thermal analysis are listed in [Table 2.2](#) ([Cullen and Korkolis, 2013](#), [Knysh and Korkolis, 2015](#)). Thermal losses through the gripped areas are modeled using a constant temperature (equal to the ambient temperature of 22 °C) at the ends of the tube. Radiation heat losses are included only on the outside surface of the tube, as it is assumed that the inside surface irradiates on itself and no heat is transferred in this manner. Finally, the heat losses due to convection are substantial for a thin-walled tube and also have to be taken into account. However, it's not easy to estimate a film coefficient accurately, as it is very sensitive to a number of parameters such as geometry, local temperature of the tube,

surface roughness, external airflows, etc. It was decided to determine a value of film coefficient indirectly, using the optimization procedure described in Section 2.3 and after all the hardening curves were identified. By setting the film coefficient to be the free variable, with an initial guess of $25 \text{ W}/(\text{m}^2 \text{ K})$ (Cullen and Korkolis, 2013) and applying the same the objective function as before, the film coefficient of $8.4 \text{ W}/\text{m}^2\text{K}$ was found (Fig. 2.11) to provide the optimal fit.

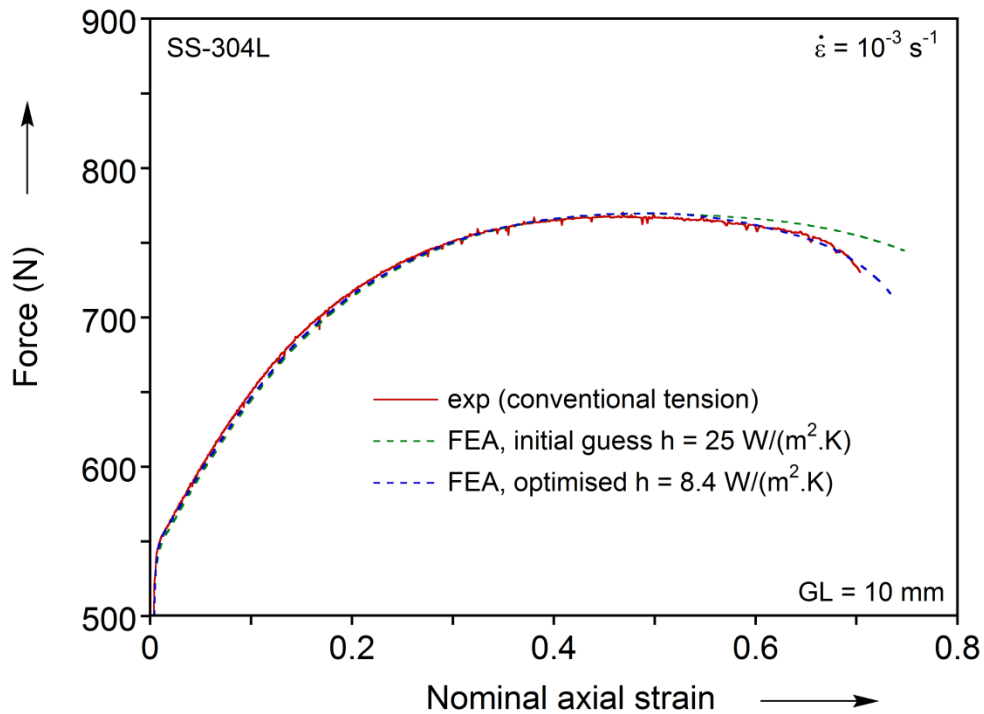


Figure 2.11 – The matching in force-average axial strain response between FEA and experiment for the convection coefficient value identified with optimization procedure ($8.4 \text{ W}/\text{m}^2\text{K}$). Also included is the response from the initial guess.

Since the force-average axial strain data was already used to identify the appropriate value of the film coefficient, different metrics should be used for the further validation of the hardening curves identified. This was accomplished by utilizing the full-field techniques for measuring strain and temperature during the experiments. In addition, the predictions of the fully-coupled FE model are compared to those of the

R&TI FE model.

Table 2.2. Physical and material properties used for the numerical simulations

Mechanical properties		
Young's modulus	E	187 GPa
Poisson's ratio	ν	0.3
Physical and thermal properties		
Density	ρ	8000 kg/m ³
Thermal conductivity	k	16.2 W/(m·K)
Inelastic heat fraction	β	0.8
Specific heat	c	500 J/(kg·K)

The measured and predicted axial and hoop strain fields are compared between two models and the conventional tension experiment in [Figs. 2.12 and 2.13](#). It can be seen that before the localization and necking sets-in at about 50% average strain, both models agree well with the experiment. However, the R&TI model predicts a much less diffuse neck than what is observed experimentally, as well as what is predicted by the fully-coupled model. This is further substantiated in [Fig. 2.14](#), which shows the evolution of necking in the experiment and the 2 models. This difference is because the increase in the strain-rate and temperature that is associated with localization spreads the extent of necking axially more than in the hypothetical R&TI case. Furthermore, the establishment of a temperature gradient along the specimen (e.g., see [Figs. 2.3 and 2.15](#)) implies that the areas of the specimen that are cooler (i.e., towards the ends)

show less total strain (mechanical + thermal) than the hotter middle ones. This can be discerned in the strain fields shown in Figs. 2.12 and 2.13. Finally, of interest to observe is that once the localization sets-in (at an average strain of about 50%), the R&TI model predicts no further growth of the strains outside of the neck. In contrast, the fully-coupled R&TD model shows a continuous growth, albeit at a slower rate than inside the neck, as does the experiment.

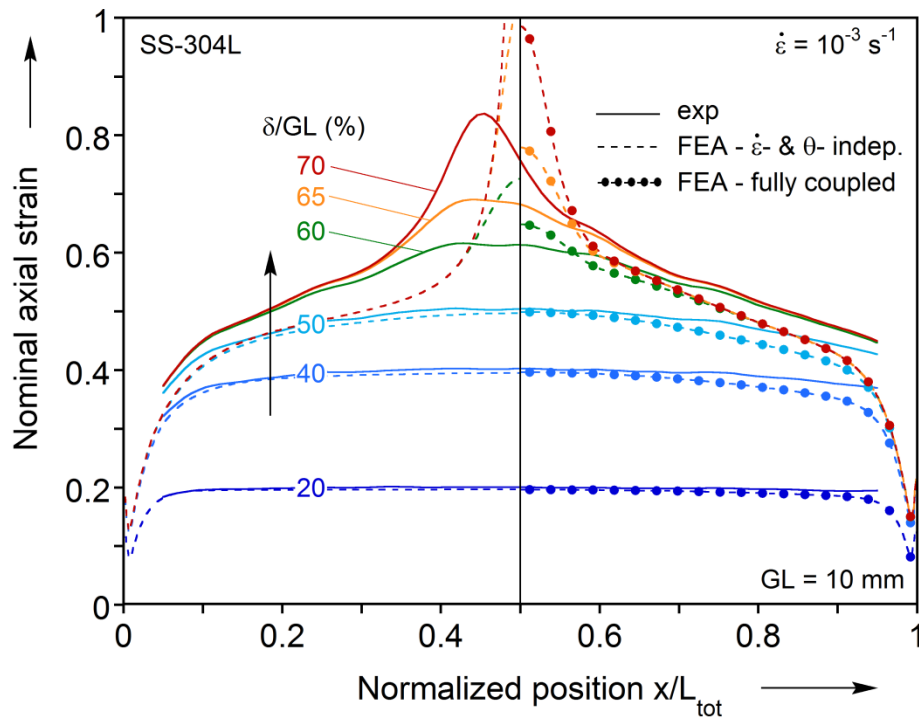


Figure 2.12 – Evolution of axial strain along the specimen in the conventional tension test.

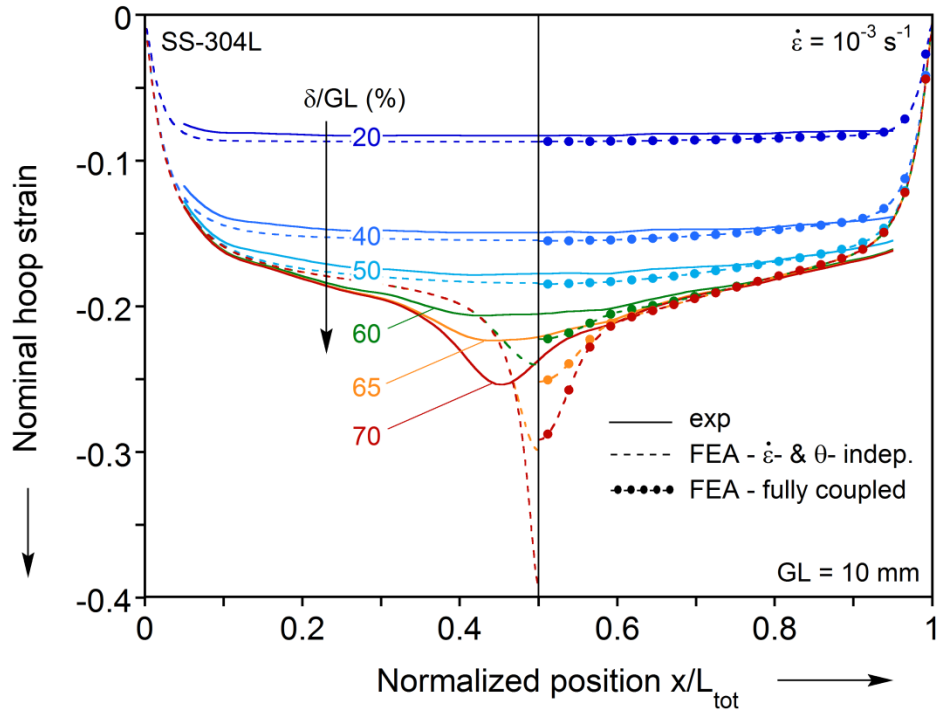


Figure 2.13 – Evolution of hoop strain along the specimen in the conventional tension test.

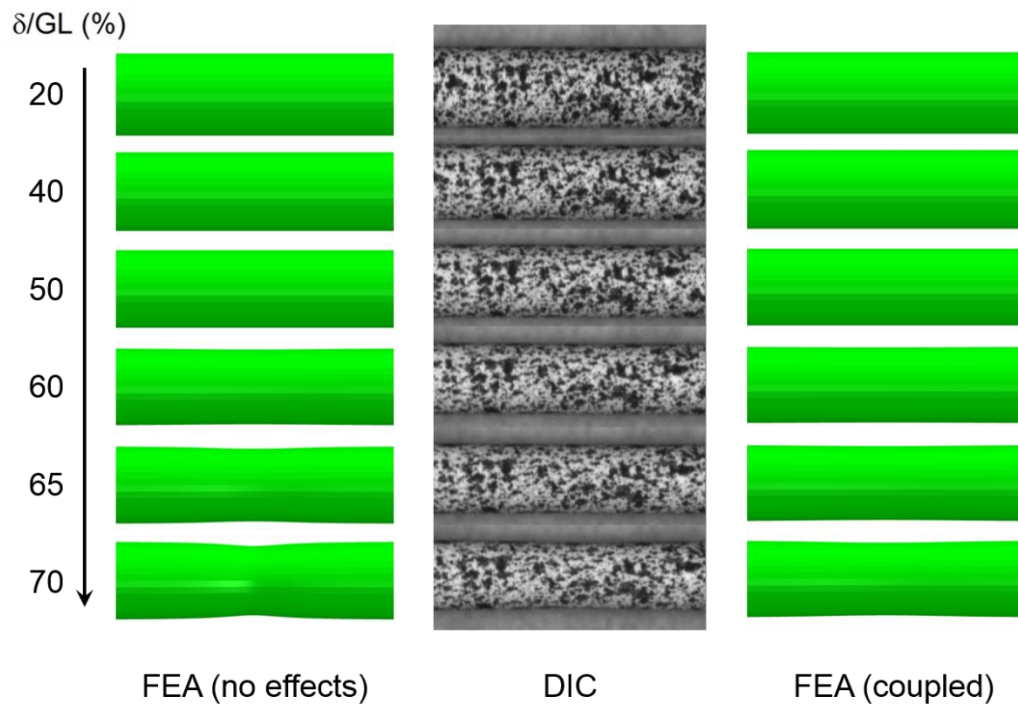


Figure 2.14 – Evolution of neck profile in conventional test.

As a final validation of the identification procedure, the predicted temperature gradient along the specimen is compared in Fig. 2.15 to the one measured experimentally. It can be seen that the model captures the temperature gradient very accurately, definitely up to the onset of necking.

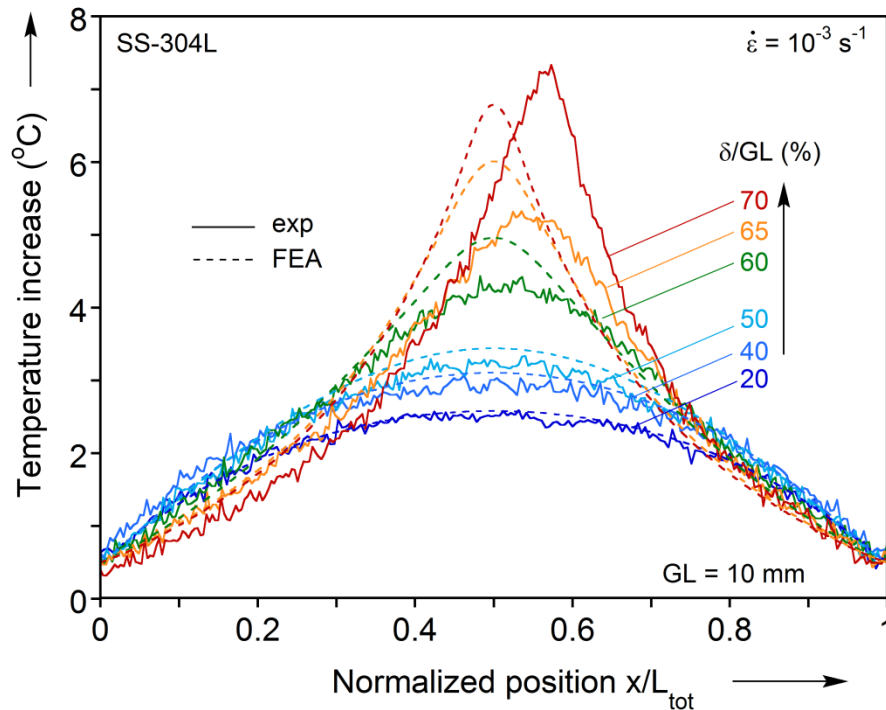


Figure 2.15 – Evolution of temperature along the specimen in conventional test.

2.5. Summary and conclusions

An approach to identify post-necking hardening curves with decoupled rate and temperature effects was proposed in this work. Isothermal tension experiments were performed on SS-304L tubes using a custom setup. The problem was tackled as an optimization task. An objective function was created using parameters that control the post-necking shape of the hardening curves as input, and a scalar value that represents the proximity between the predicted (FEA) and experimental structural responses as output. Because such a function is expensive to evaluate, an optimization procedure

based on the response surface methodology was implemented in order to reach an optimum with limited number of function evaluations. The post-necking hardening curves were identified under different assumptions: without considering rate and temperature effects; by considering only the temperature effect; and by considering both rate and temperature effects. The latter case makes the most sense, physically.

The hardening curves identified were verified using fully-coupled thermomechanical FEA for modeling a conventional tension test. A proper value of the convection coefficient was found using the optimization procedure to match the experimental force-average axial strain curve. Using full-field measuring techniques (DIC and IR) it was possible to extract the strain and temperature fields along the specimen and compare them to the FE predictions. These predictions were found to be more accurate for the case of the fully-coupled curves in comparison to rate- and/or temperature-independent cases.

The major conclusions are summarized below:

- Stainless steel 304L exhibits rate- and temperature-dependent plastic flow. A simple but very effective isothermal tension test was proposed, to decouple the mechanical and thermal effects when probing the material response.
- This material exhibits strong deformation-induced heating, so that a temperature gradient is established from the early stages of plastic deformation.
- The response surface methodology proposed here for the problem at hand was found to converge to the global minimum with a limited number of iterations (i.e., function evaluations).
- The post-necking shapes of the hardening curves depend strongly on the

consideration of rate and temperature effects.

- A thermomechanical simulation of the conventional (i.e., non-isothermal) tension test, using the hardening curves identified here in a fully-coupled way across the strain-rate and temperature ranges, provided close predictions of both the strain and temperature fields measured experimentally. Using hardening curves identified in a decoupled fashion was seen to be deficient in matching these measurements.

In the future, the hardening curves identified for the SS-304L microtubes will be used to probe the plastic flow and fracture under biaxial linear and non-linear paths, as well as to model microtube hydroforming.

CHAPTER 3

A SHAPE INTERPOLATION PROCEDURE: APPLICATION TO CREATING EXPLICIT GRAIN STRUCTURE MODELS BASED ON PARTIAL DATA SETS²

3.1. Introduction

This chapter switches the topics and also the level of analysis from macroscopic (Chapter 2) to grain-scale. Namely, it describes the details of general procedure for 3D reconstruction from a pair/set of parallel 2D images. This procedure is then successfully used in Chapter 4 for producing a realistic texture of the oligocrystal model.

Modeling of polycrystalline metals often employs spatially resolved computational techniques especially when attempting to reveal critical aspects of extreme material behavior such as void nucleation, where knowledge of plasticity processes at grain scale is necessary. The finite element (FE) numerical method has been extensively used for calculating mechanical fields (Ardeljan *et al.* 2015, Barrett *et al.* 2018, Knezevic *et al.* 2014, Zhao *et al.* 2008). Under uniform macroscopic loading, these models reveal heterogeneous deformation because they account for the spatial distribution of grain size and shape of constituent grains and their inherent anisotropy, as well as intergranular interactions. The FE models are constructed based on microstructural characterization data.

² Published as Knysh, P., Sasaki, K., Furushima, T., Knezevic, M. and Korkolis, Y.P., 2019, A shape interpolation procedure: Application to creating explicit grain structure models based on partial data sets. *Computational Materials Science*, 167, pp. 42-51.

A widely used methodology for synthetic voxel-based explicit grain structure generation is the Voronoi tessellation method, along with various extensions (Aboav 1970, Boots 1982, De Berg *et al.* 2000, Diard *et al.* 2005, Shenoy *et al.* 2008, Zhang *et al.* 2012). The digital microstructure analysis environment DREAM.3D has recently been developed by the U.S. Air Force Research Laboratory and Blue Quartz (Groeber Jackson 2014) as a more advanced alternative for creating synthetic microstructures. Reconstructing a synthetic microstructure is often statistical (Fullwood *et al.* 2008).

Realistic microstructures can be obtained by in-situ experimental techniques such as focused-ion-beam electron-back-scattered-diffraction (FIB-EBSD) for serial sectioning and EBSD for obtaining crystallographic map for each section (Calcagnotto *et al.* 2010, Khorashadizadeh *et al.* 2011, Uchic *et al.* 2006, Yi *et al.* 2009, Zaafarani *et al.* 2006, Zaefferer *et al.* 2008). However, a disadvantage of sectioning methods is that they are destructive. Non-destructive near-field high-energy X-ray diffraction microscopy (nf-HEDM) (Johnson *et al.* 2008, Li *et al.* 2012, Lind *et al.* 2014, Ludwig *et al.* 2008, Stein *et al.* 2014) has also been developed to acquire voxel-based grain structure data in 3D. Instead, reconstruction of the 3D microstructure from 2D scans of external faces is non-destructive, and the scanned specimen can then be used for further testing.

The reconstruction of 3D objects from a set of 2D slices is an important task that finds its primary applications in medical imaging of the brain (Joliot Mazoyer 1993), heart (Boissonat 1988, Goshtasby *et al.* 1992), blood vessels (Chen *et al.* 1990), skeleton (Bajaj *et al.* 1996, Raya Udupa 1990), teeth (Bors *et al.* 2002), and other parts of human body (Higgins *et al.* 1996, Luo Hancock 1997). As stated in Bors *et al.* 2002, there are two main categories of methods for reconstruction from slices: grey-level

interpolation and shape-based interpolation. In grey-level interpolation ([Higgins *et al.* 1996](#)) grey intensities of pixels in the reconstructed images are approximated by corresponding grey intensities of pixels in the input images (using linear, polynomial, spline functions, etc.). In contrast, shape-based interpolation uses binary input/output images. One of the successful techniques that is used for shape-based interpolation is morphing ([Bors *et al.* 2002](#), [Joliot Mazoyer 1993](#), [Luo Hancock 1997](#), [Surazhsky *et al.* 2001](#)). The idea of the technique is to iteratively “average” pairs of neighboring sections using the mathematical operations of dilation and erosion, and subsequently stack all images on top of each other (grain reconstruction by stacking a number of 2D slices was addressed before in [Inkson *et al.* 2001](#), [Rowenhorst *et al.* 2006](#), [Ha *et al.* 2017](#)).

In this work, we propose a shape-based interpolation algorithm that uses a morphing technique. The method works with a set of images that contain a given number of colors, each representing a different volumetric phase ([Sasaki *et al.* 2017](#), [Knysh *et al.* 2018](#)). Due to the way the proposed method works, the scope of the procedure is limited to compact grain shapes (i.e., those with aspect ratios “close” to 1:1:1) that appear in at least two consecutive sections. We provide a simple demonstration example, as well as an example of application for real, explicit grain structure images. In the latter we reconstruct the topology of the grains in a thin metallic specimen based on a pair of EBSD scans ([Humphreys 2004](#)). It is assumed that the thin specimen contains one layer of grains through its thickness, so that every grain appears on both scans. The procedure proposed is then verified by sequentially removing layers from the specimen, performing EBSD scans and comparing the measurements with the reconstructed grains. A very good agreement between the two is observed. Therefore,

the procedure can be applied for explicit grain structure reconstruction, provided that only a single layer of grains exists through the thickness. We propose a check to establish that fact, since the destructive method we use here may not always be applicable. We also demonstrate how the procedure can be used for a reconstruction from multiple sections using a dual-phase, martensite-ferrite representative volume element. Furthermore, we assess the probability of false-positive in our procedure, i.e., to mistakenly treat two similar but different grains in the pair of EBSD scans as one. For the material we examined this is limited to 0.7%.

To the authors' knowledge, there is no similar procedure available in commercial codes used for image processing. As supplementary material, a code that generates nodal coordinates and element connectivity, which can be used for finite element meshing, is provided.

3.2. Description of the procedure

Below we describe how the reconstruction procedure is applied to a pair of parallel sections. The procedure can be easily extended to any number of sections (see [Section 3.3c](#)).

The procedure aims at reconstructing a 3D voxel model based on images of two parallel sections of a 3D volume. Both images contain the same sets of colors. Each color represents its corresponding volumetric phase such as a grain of a metallic material. The resolution of both images is $w \times l$ pixels and the volume between the sections needs to contain a given number of voxel layers h .

The desired output is a set of h images that includes the given top and bottom images, as well as the $h - 2$ intermediate (reconstructed inside of the bulk volume) images. Such images, if stacked on top of each other, give the desired voxel model.

a. Reconstructing the mid-plane image between two images

We begin by describing the most important part of the procedure - how to reconstruct the mid-plane image between two images. At this step we need to find an average (in the sense of Fig. 3.1) of two images.

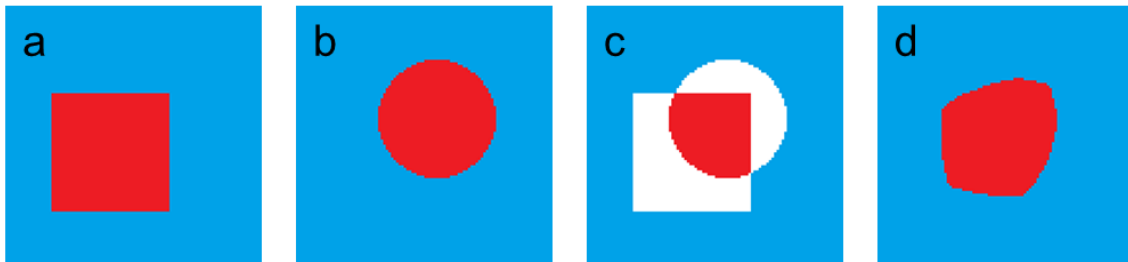


Figure 3.1 – Constructing the mid-plane image (d) from given 2 images (a, b). c shows the overlap of a and b; the mismatch areas are shown in white. Each mismatch area is filled with its neighboring colors iteratively, until image d is obtained.

Firstly, we overlap the given two images. Areas in which colors in both images are matching will be called “match areas”, otherwise, “mismatch areas”. Colors in match areas are kept as they are (i.e., unchanged), while each mismatch area is assigned with its own unique color (e.g., white). Next, in order to fill all mismatch areas we colorize them with neighboring colors from right/top/left/bottom pixels iteratively.

In formal terms, the top and bottom images can be represented by matrices T and B , respectively. Each matrix is of dimension $w \times l$, filled with non-zero integers that

represent colors (phases). The mid-plane image is a matrix M , that is obtained using the following operation:

$$M_{ij} = \begin{cases} T_{ij}, & \text{if } T_{ij} = B_{ij} \\ 0, & \text{if } T_{ij} \neq B_{ij} \end{cases} \quad (3.1)$$

The iterative procedure can then be written in the following way:

1. Find all M_{ij} : $M_{ij} = 0, M_{i(j+1)} \neq 0$. Assign $M_{ij} \leftarrow M_{i(j+1)}$.
2. Find all M_{ij} : $M_{ij} = 0, M_{(i-1)j} \neq 0$. Assign $M_{ij} \leftarrow M_{(i-1)j}$.
3. Find all M_{ij} : $M_{ij} = 0, M_{i(j-1)} \neq 0$. Assign $M_{ij} \leftarrow M_{i(j-1)}$.
4. Find all M_{ij} : $M_{ij} = 0, M_{(i+1)j} \neq 0$. Assign $M_{ij} \leftarrow M_{(i+1)j}$.
5. If M contains zeros, repeat steps 1-4.

The procedure is illustrated for a simple case of two binary images in [Fig. 3.1](#) and works similarly when the images contain more colors.

The order of operations 1-4 is not important and will not cause negligible changes to the final result (d).

Such process of constructing the “average” between two images can be classified as one of the morphing techniques. More general cases of morphing are considered in detail in [Bors et al. 2002](#), [Joliot Mazoyer 1993](#), [Luo Hancock 1997](#).

The procedure has one major limitation - in order to interpolate between two shapes, those shapes must overlap somewhere. Otherwise there are no match areas for a given color, so the mismatch areas will be filled with other colors but not with the needed one. In the context of texture reconstruction, the procedure is generally applicable only to grains of compact shapes that appear in both images.

b. Generation of a desired number of intermediate layers

The procedure described above (reconstruction of a mid-plane image from 2 images) is initially applied to the top and bottom scans to obtain the first 3 layers - top, middle, bottom. Subsequently, it can be reapplied to the top-middle and middle-bottom pairs of images to obtain 2 more layers, and so on. However, due to such bisectional manner of producing additional layers, their total number is always equal to $2^n + 1$, where n is the number of bisection cycles (each bisection cycle inserts a mid-plane section between each pair of neighboring sections).

In order to produce the desired number of layers h , we can perform a simple indicial rescaling using the following formula:

$$\text{round}\left(i \frac{2^n}{h-1}\right) + 1, \quad i = 0, \dots, h-1. \quad (3.2)$$

For example, assume we performed three bisection cycles ($n = 3$), which will have resulted in $2^3 + 1 = 9$ layers. If we need to obtain exactly 6 layers instead (i.e., $h = 6$), we apply [Eq. \(3.2\)](#) to obtain the proper rescaling pattern:

$$(1,2,3,4,5,6,7,8,9) \rightarrow (1,3,4,6,7,9). \quad (3.3)$$

This pattern dictates that in the given example, of the 9 original layers we keep the 6 identified in [Eq. \(3.3\)](#) and equispace them through the thickness.

For a given number of layers h we recommend to pick the minimal value n such that $2^n + 1 \geq h$. This allows to perform a minimal amount of bisection cycles without repetitions of layers in the obtained set.

Regarding the time to compute the reconstruction, it is linearly proportional to:

1. $N - 1$, where N is the number of input sections.

2. $w \times l$, i.e., the number of pixels in each image.
3. $2^n - 1$, where n is the number of bisectional cycles.

3.3. Application examples

a. Simple demonstration example

Here we provide a simple example to demonstrate how the morphing procedure described works for interpolation between two shapes. With reference to Fig. 3.2, the input is two images of dimension 100×100 pixels, shown in top left and bottom right corners (i.e., a “lightning” and a “star”). We are producing 10 layers ($h = 10$, therefore $n = 4$) that interpolate the two given images. As we can see, the images generated provide a smooth transition between two shapes. By varying the number of layers h it is possible to control the smoothness of interpolation.

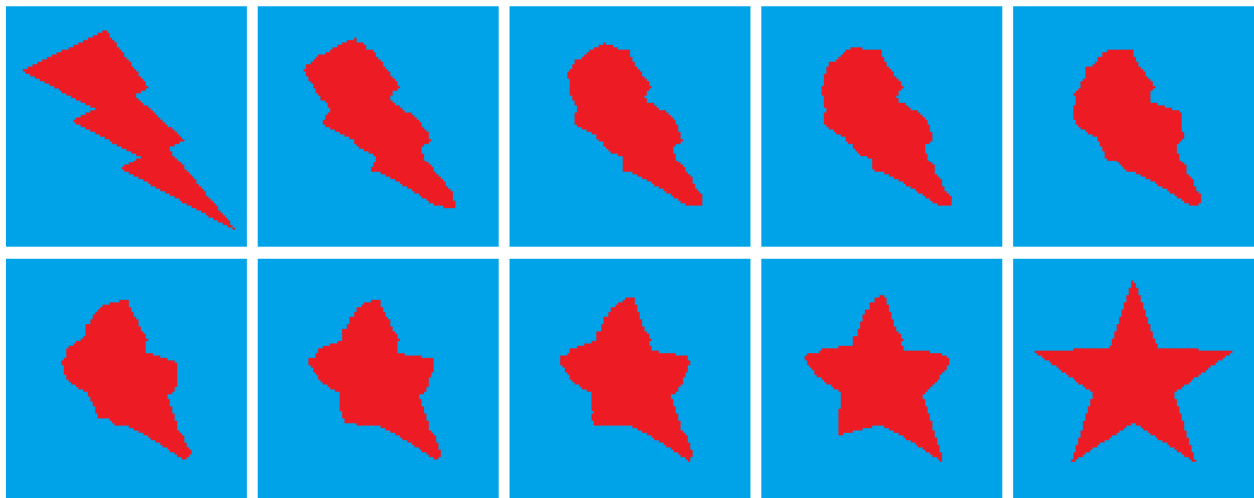


Figure 3.2 – A set of images that interpolates two given images (“lightning” and “star”), produced by the morphing procedure described here.

A corresponding 3D voxel model is constructed and shown in Fig. 3.3. Such a model can represent the finite element mesh of a given material phase (for example, a grain).

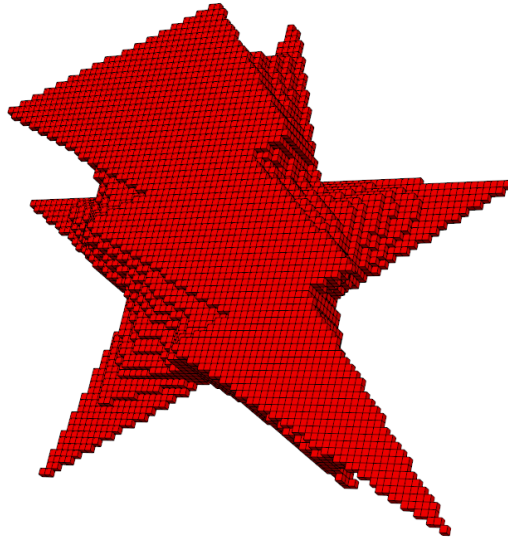


Figure 3.3 – The 3D voxel model produced by stacking the images from Fig. 3.2.

b. Application to explicit grain structure reconstruction

The morphing procedure described can be used in multiple applications in order to construct a voxel model of a given 3D object. In the current work, we use the procedure for reconstructing the volumetric grain structure of a thin Al-Mg specimen from two EBSD scans. The gauge area of the specimen is a rectangular block with in-plane dimensions of 6 mm by 1 mm and thickness of 0.12 mm. To establish that there is indeed only one grain through the thickness, which is the assumption our procedure hinges upon (see [Section 3.1](#)), we propose to scan a plane perpendicular to the other two EBSD scans. This scan will reveal the grain size and morphology between the two base scans. However, in this work we employ a different, more direct but also destructive technique (see later in this Section), to establish the validity of this assumption.

The images were acquired using a HITACHI Scanning Electron Microscope with Nordlys EBSD system. Both scans were pre-processed to eliminate image rotation,

distortion and noise. Eventually the sets of matching colors appear in both images (see Fig. 3.4a and b), which is an evidence of the fact, that there is only one layer of grains through the thickness (with several grains being exceptions and shown in black).

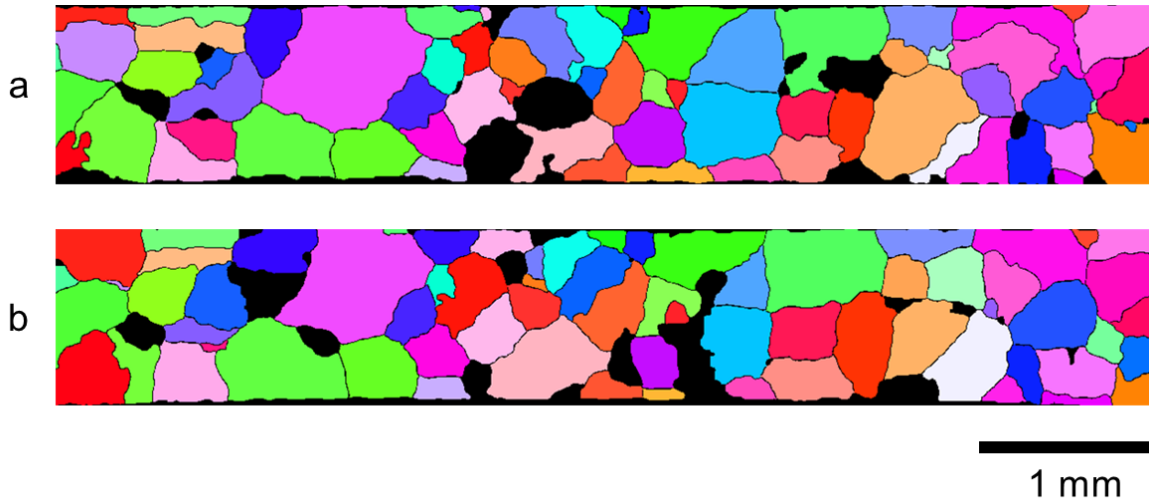


Figure 3.4 – EBSD scans of the gauge section of a micro-scale specimen. (a) – top, (b) – bottom. Different colors represent different grains. The black color is representing grains that do not go all the way through the thickness and hence are incompatible with the reconstruction procedure.

The procedure is applied to these two images in exactly same way as it was applied for the two-color example in Section 3.3a. All match areas are kept as they are, and all mismatch areas (e.g., Fig. 3.1c) are identified. Since the procedure cannot handle grains that are not visible on both EBSD sections, those grains are excluded from the analysis. The areas excluded are marked as black in Fig. 3.4 and indicate “cavities”. Then, the iterative procedure (Section 3.2a) is applied in order to fill the mismatch areas (i.e., the cavities) with their neighboring colors (e.g., Fig. 3.1c and d). During the procedure, the black color that represents the cavities is treated as any other color and the procedure is used as is. Subsequently, the mid-plane image from the two EBSD

sections is obtained. These steps are repeated until the desired amount of layers is generated.

To verify the accuracy of obtained reconstruction, we perform the following test. After the top and bottom sides of the specimen were scanned, layers of material were machined away and additional scans of two interior sections were obtained. The first interior section (A) is located at $1/6^{\text{th}}$ of the thickness (0.02 mm of 0.12 mm) from the top of the specimen. The second interior section (B) is located at $1/3^{\text{rd}}$ of the thickness (0.04 mm) from the bottom of the specimen (Fig. 3.5). EBSD scans from both interior sections were obtained and then compared with the corresponding sections from our reconstruction.

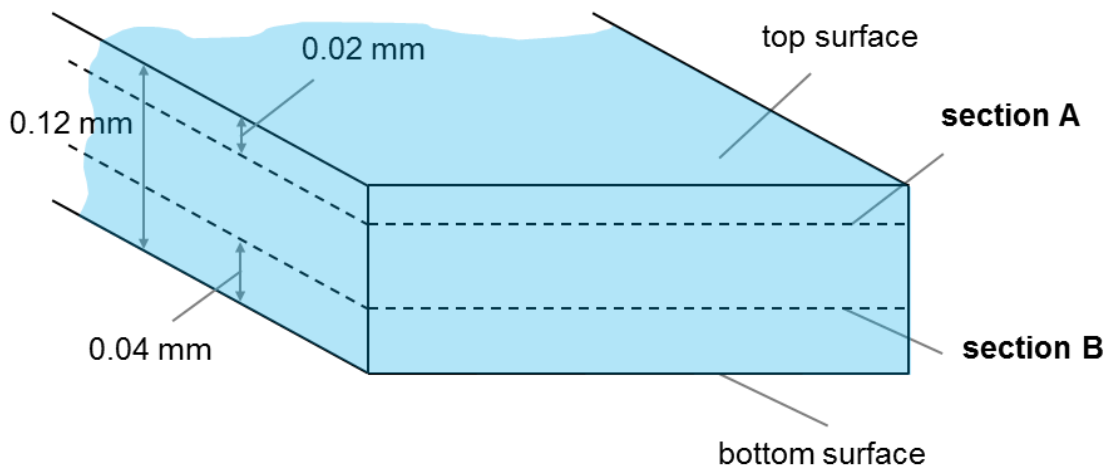


Figure 3.5 – A schematic drawing of cross-section of the specimen. Interior sections A and B are shown with dashed lines.

A comparison between measured and reconstructed morphology at these two interior sections is shown in Fig. 3.6 and Fig. 3.7. For ease of comparison we also provide “difference” images – match areas between two images are shown as gray and mismatch areas are shown as white. As we can see, the overall sizes and shapes of the

grains at both interior sections are predicted well. In Fig. 3.6 we can see that middle area of the section A ($1/6^{\text{th}}$ of the thickness from the top) contains more white color in comparison to the two side ones, which means less prediction accuracy. This is happening due to the presence of large “bad” grains (shown as black) in that area. These grains do not go all the way through the thickness, and therefore significantly affect the shapes of neighboring grains at the interior sections.

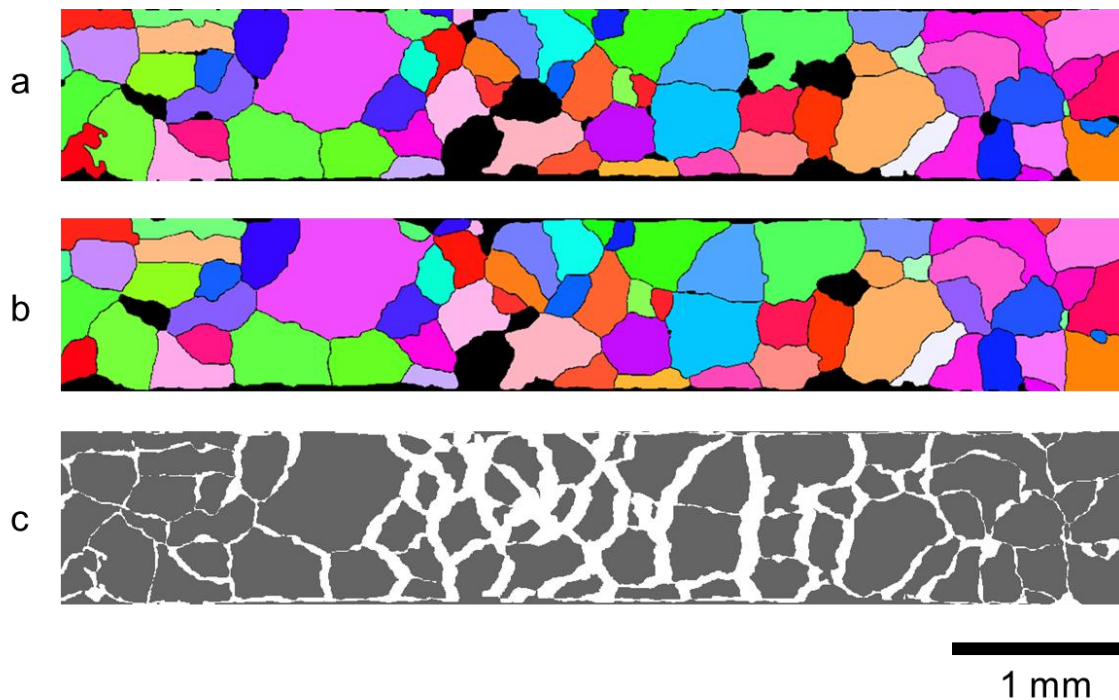


Figure 3.6 – Morphology of grain structure at section A; (a) - measured, (b) - reconstructed (c) - the difference between (a) and (b) (gray = match, white = mismatch, 24.2% of the total image).

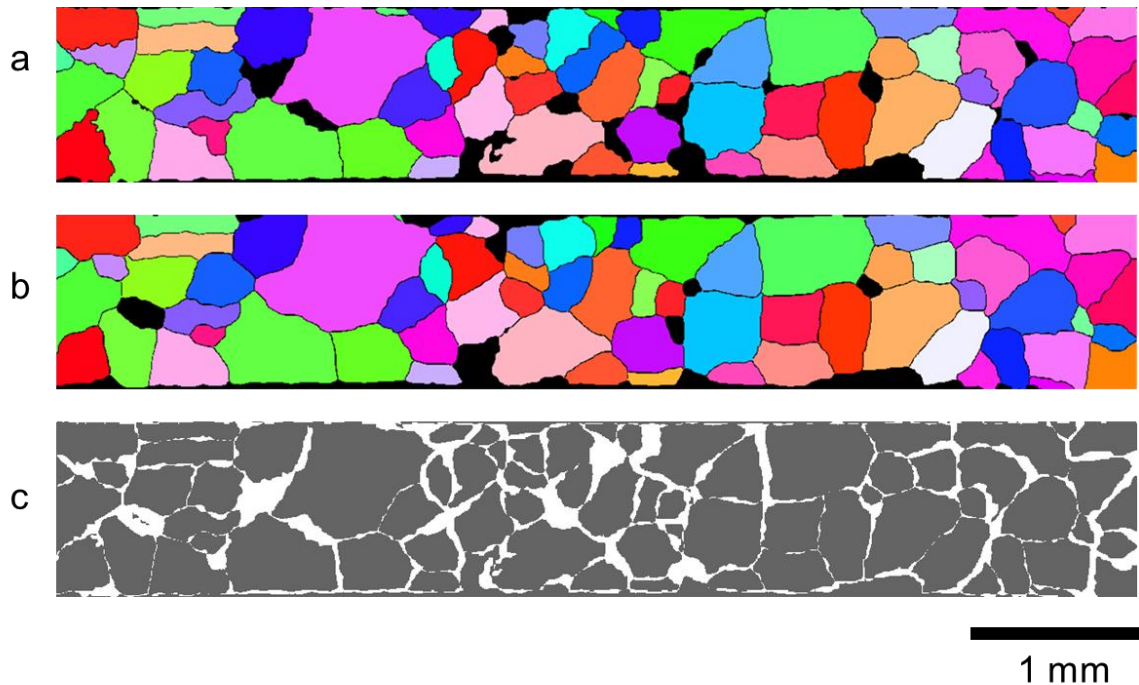


Figure 3.7 – Morphology of grain structure at section B; (a) - measured, (b) - reconstructed (c) - the difference between (a) and (b) (gray = match, white = mismatch, 16.6% of the total image).

As a further check of the validity of this procedure, we establish the probability of a false-positive in our example. This procedure is detailed in [Appendix C](#).

For illustration purposes, we also extract and show several individual grains in 3D ([Fig. 3.8](#)). As can be seen, the method works well for grains with compact shapes (left and right grains), as well as for grains with irregular features (middle grain).

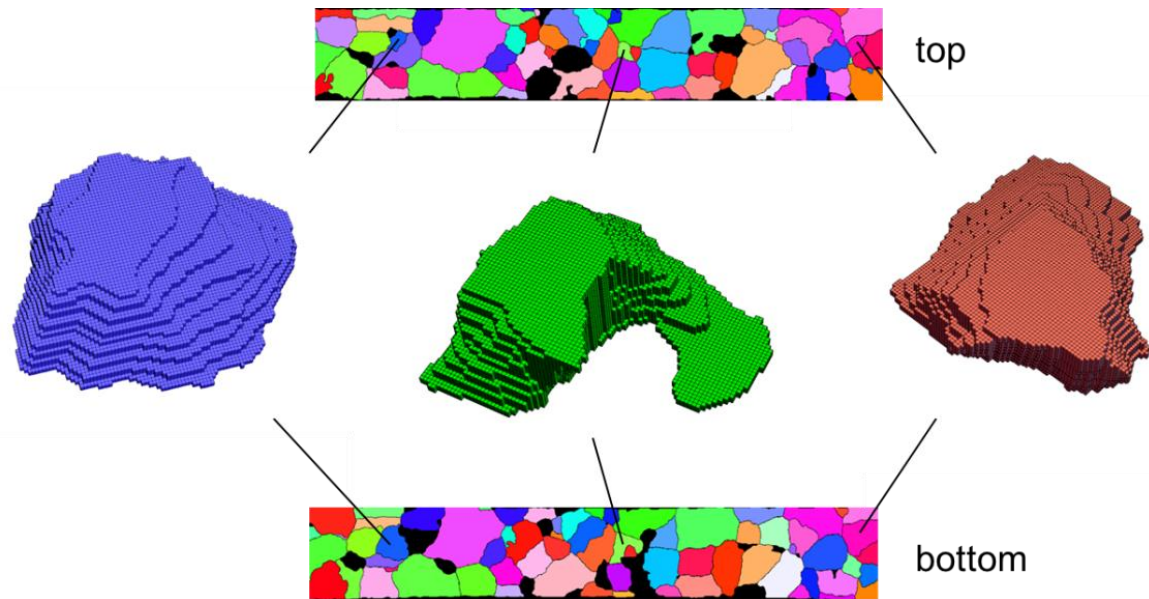


Figure 3.8 – Reconstructed voxel models of several grains.

The procedure developed in this work can be directly used to construct explicit grain structure models for crystal plasticity FE simulations from voxels, where every voxel is a finite element. Furthermore, the voxel-based models can be further processed into tetrahedral finite element mesh using a set of tools reported in [Knezevic *et al.* 2014](#). The advantage of tetrahedral mesh is in the description of grain boundaries as surfaces instead of stair-stepped grain boundaries, as a consequence of voxels and brick finite elements. An inherent advantage of the proposed method is that it generates surfaces of minimum area (or at least their step-wise approximants), which is consistent with the thermodynamics of grain growth.

c. Application to a reconstruction from multiple sections

As was mentioned above, reconstruction from 2 sections can be readily extended to reconstruction from any number of sections. In order to do that we apply the procedure

to each pair of consecutive sections. To demonstrate how reconstruction from multiple sections works, we apply it for 25 sections (of resolution 100×100 pixels) of a dual-phase, martensite-ferrite representative volume element (Fig. 3.9) of a DP 780 steel (Ha *et al.* 2017). These input sections were obtained by optical microscopy. In Fig. 3.9, the two phases are identified with different colors (blue for the martensite islands and red for the ferrite matrix).

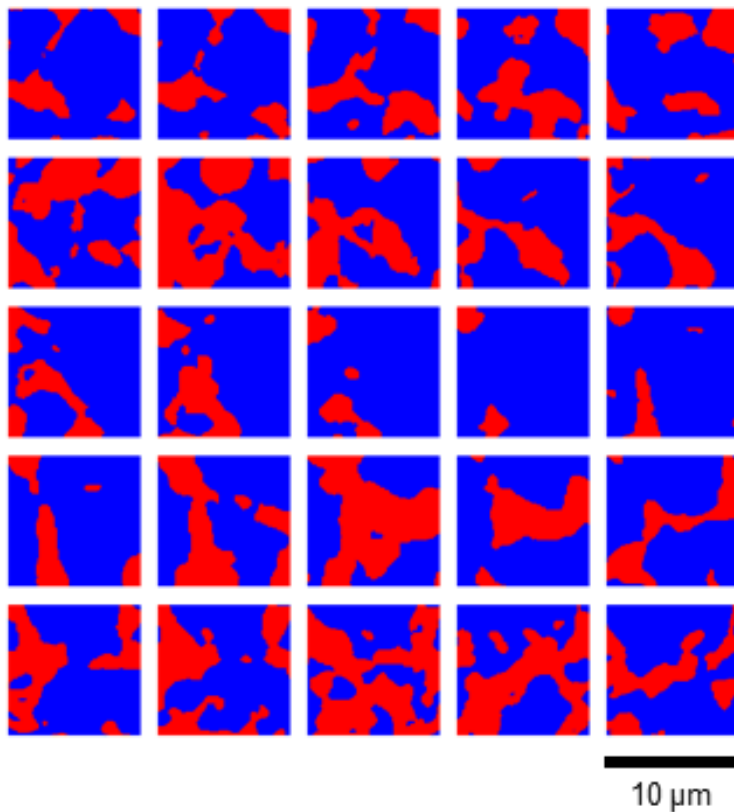


Figure 3.9 – Optical micrographs used as input for the reconstruction process of a martensite (red) – ferrite (blue) representative volume element.

To apply the procedure, we use two bisections in sequence, which results in 3 subsections generated between each pair of the original sections. In this way, the resultant model contains 97 sections and is shown in Fig. 3.10. The 3D voxel model obtained in this way can be used for further analysis (such as FE simulation), as well as

simply for visualization purposes. Indeed, in Fig. 3.10, the reconstructed model is meshed with solid, hexahedral finite elements.

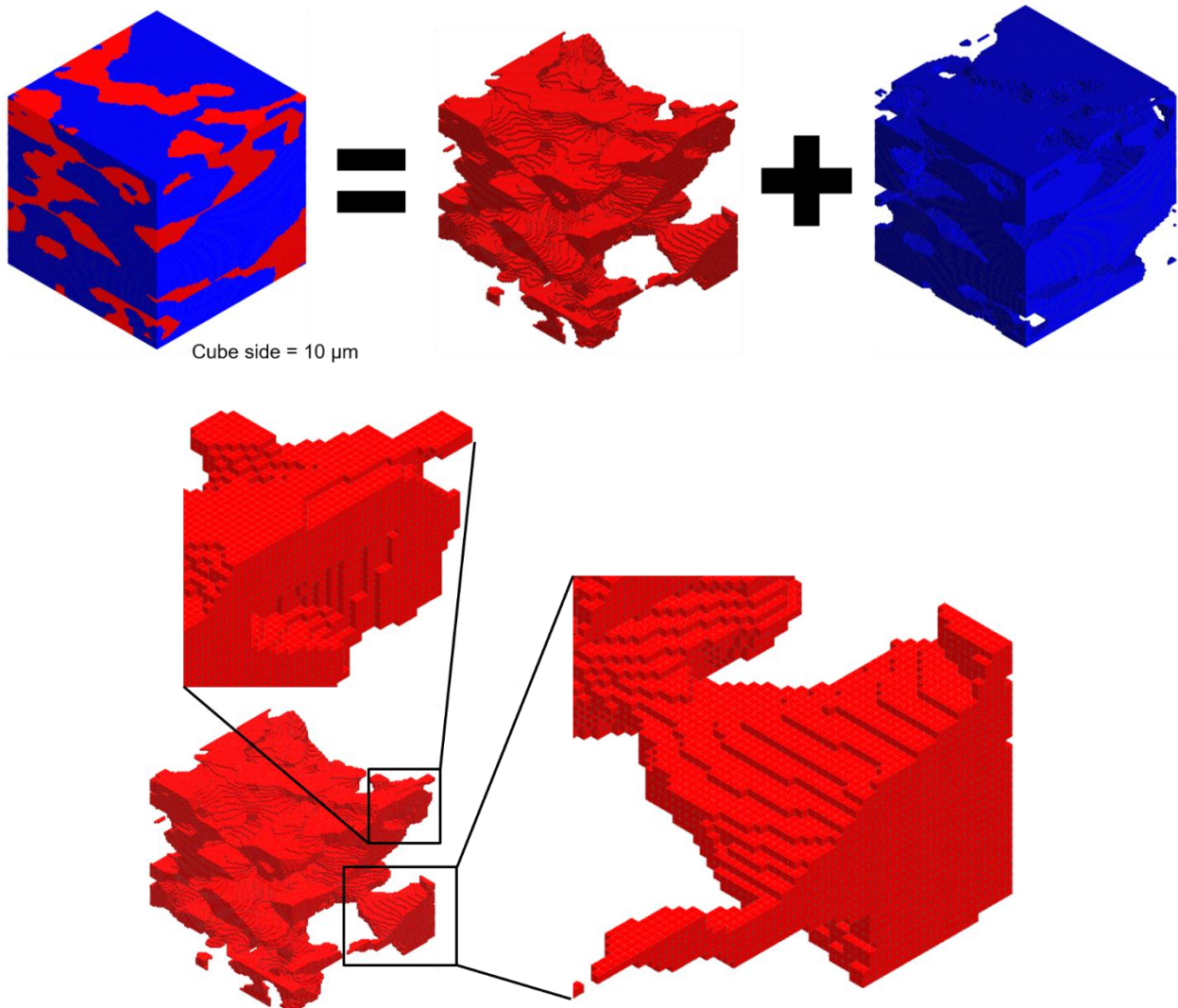


Figure 3.10 – Reconstructed voxel model martensite-ferrite representative volume element and magnification showing the finite element mesh.

3.4. Summary and conclusions

We propose a method that allows the reconstruction of a 3D voxel model from two images obtained from parallel sections of a physical object. The method is based on a morphing technique. The input to the method is a pair of images from given parallel

sections, the output is a sequence of images that interpolate the two given images. The images produced can be stacked on top of each other in order to obtain a 3D voxel model. The procedure works well for binary images as well as for images that contain matching sets of colors.

We first demonstrated the method for a simple artificial input. Also, we showed how it can be applied to real grain structure scans in order to reconstruct the volumetric grain structure of a thin metallic specimen. It was possible to verify the accuracy of the texture reconstruction by looking into how well the prediction is matching the actual structure in the bulk of the specimen. Finally, we demonstrated the feasibility of reconstruction from multiple sections using a dual-phase, martensite-ferrite representative volume element.

To the authors' knowledge, there is no similar procedure available in commercial codes used for image processing.

CHAPTER 4

DEFORMATION-INDUCED SURFACE ROUGHENING OF AN ALUMINUM-MAGNESIUM ALLOY: EXPERIMENTAL CHARACTERIZATION AND CRYSTAL PLASTICITY MODELING³

4.1. Introduction

In this chapter a comprehensive analysis of deformation-induced surface roughening is described. This chapter unifies other topics of the thesis as it relies on a shape reconstruction procedure developed in [Chapter 3](#), as well as black-box optimization procedure developed in [Chapter 2](#).

Deformation-induced surface roughening is a phenomenon of heterogeneous crystallographic origin, that can affect both the appearance and performance of a formed part. It manifests itself as a gradual change of the surface topography with plastic deformation, towards a surface with undulations of increasing amplitude. During forming, these undulations can act as stress risers, triggering an earlier localization of deformation in comparison to the same solid but with a smooth surface, hence limiting the capacity of the solid to stretch in the global sense. During service, the surface undulations can impair the fatigue life, acting as nucleation sites for extrusions/intrusions, etc. But even if premature failure is not an issue, the non-smooth surface can cause aesthetic concerns whether in the bare or coated form.

³ Submitted for publication as Knysh, P., Sasaki, K., Furushima, T., Knezevic, M. and Korkolis, Y.P., 2019, Deformation-induced surface roughening of an Aluminum-Magnesium alloy: Experimental characterization and crystal plasticity modeling.

The origins of this phenomenon rest with the strong intrinsic anisotropy of grains and the presence of preferred crystallographic texture in the as-received material. Therefore, under a macroscopically imposed strain, each deforms by activating its own slip systems, which are different from those in differently-oriented neighbors. At the same time, each grain is forced to accommodate the deformation of its neighbors so that the solid remains a continuum, in the macroscopic sense. However, at a free surface these constraints are much less, so that the differences in individual grain deformation are macroscopically seen as surface undulations, i.e., deformation-induced surface roughening.

A number of authors have previously studied the fundamental physical origins of deformation-induced surface roughening. In one of the pioneering works by [Osakada and Oyane 1971](#) several aspects triggering the surface roughening during deformation processes were studied using 52S aluminum. The average surface roughness was demonstrated to increase with strain ([Fig. 4.1](#)), and the roughening rate was shown to be affected by the mode of deformation. It was also found that the roughening rate was affected by grain size and the lattice structure of the metal. Roughening was found to be much more pronounced in metals with large grain size and small number of slip systems. Similar observations were obtained in [Guangnan and Huan 1990](#), where the roughness evolution of the free surface of a steel/aluminum sheet during stretch forming was investigated with a scanning electronic microscope and a profilometer. The surface roughness was measured for different strain states and levels. The results showed that the grain reorientation is the most important source of surface roughening. The roughening rate was found to be proportional to the initial surface roughness, as well as

to macroscopically applied strain.

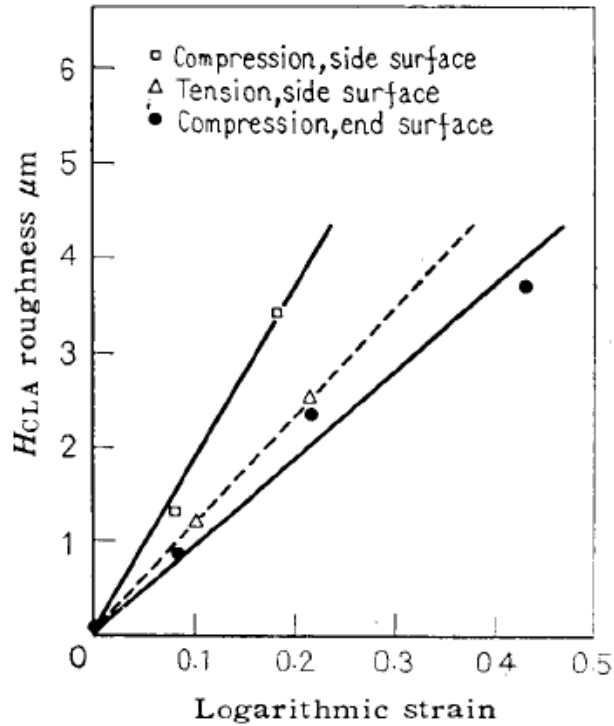


Figure 4.1 – Dependence between roughness and applied strain observed in Osakada and Oyane 1971.

A natural way of studying roughening behavior is by using numerical simulations. One of the first comprehensive numerical studies was done in [Becker 1998](#) in order to determine the effect of microstructure and mechanical properties. His model was applied on Al-6111-T4 sheet and accounted for the grain structure near the sheet surface, with the behavior of the grains being characterized by a constitutive model that accounted for deformation by crystallographic slip and for rotation of the crystal lattice during deformation. In addition to the known dependence of surface roughening on strain and grain size, it was determined that small scale strain localization at the surface plays a significant role. A number of other factors (such as strain hardening, crystallographic texture and material homogeneity), also found to be affecting surface

roughening. His results also demonstrated the effects of the strain localization induced by the material inhomogeneity. According to another study on 1100-H14 and 5052-0 aluminum alloys by [Wilson and Lee 2001](#) the predominant mechanism of surface roughening was associated with the orientation of slip systems in adjacent grains leading to mismatch strains at the grain boundaries. The emergence of slip planes played smaller role in the roughening process. A roughening model that assumed a spatial hardness variation was developed and matched well with theoretical predictions of the dependence of the surface roughness with bulk strain.

A study on grain-scale micromechanics of polycrystal surfaces during plastic deformation was done in [Raabe et al. 2003](#) for an aluminum alloy. A relationship between micro-strain heterogeneity and surface roughness in plastically strained polycrystals was discovered. Experiments (tensile and bending tests on sheet samples cut in rolling and transverse directions) were conducted on polycrystals with identical composition but different processing and microstructures. In [Tijum et al. 2007](#) the evolution of roughness at the surface of coating that co-deforms with a metal (stainless steel) under uniaxial strain was considered.

Besides fundamental studies, a number of authors studied surface roughening effects in context of sheet forming processes. In [Yamaguchi and Mellor 1976](#) an effect of thickness and grain size on the limit strains in isotropic sheet metals under biaxial tension was presented. The sheet surface was assumed to contain roughness which increases proportionally with the equivalent strain and the grain diameter of the material. Numerical results show that the limit strains decrease in all cases as the thickness-to-grain-size ratio decreases. The increase in surface roughness with plastic strain was

found to vary from material to material. Similar analysis was done in [Lee *et al.* 1998](#), [Beaudoin *et al.* 1998](#), [Mahmudi and Mehdizadeh 1998](#), [Tadros and Mellor 1978](#), [Banovic and Foecke 2003](#).

As for the choice of the material, pure aluminum and aluminum alloys are traditionally the most popular choice for performing studies on surface roughening. In [Stoudt *et al.* 2011](#) aluminum samples were mechanically polished, and uniaxially strained in situ under a scanning laser confocal microscope. Prior to deformation, electron backscatter diffraction was performed on the gauge sections of one specimen in the rolling direction of the sheet and one in the transverse direction. The effects of Taylor factors, grain boundary misorientation, largest Schmid factors, grain sizes, coincident site lattice orientations, and local grain breakup were considered. The largest surface displacements were observed to be concentrated at junctions where there was a large difference between the Taylor factors of the individual grains. More studies on aluminum and aluminum alloys were done in [Lo and Horng 1999](#), [Sachtleber *et al.* 2004](#), [Stoudt *et al.* 2011](#), [Turner and Miller 2007](#), [Wittridge and Knutsen 1999](#), [Wu and Lloyd 2004](#), [Zhao *et al.* 2004](#), [Zhao *et al.* 2008](#). A columnar model of aluminum oligocrystal studied in [Zhao *et al.* 2008](#) is shown in [Fig. 4.2](#).

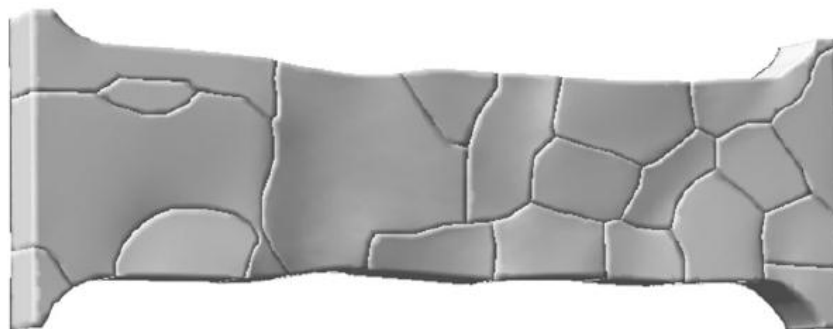


Figure 4.2 – A columnar model of aluminum oligocrystal studied in [Zhao *et al.* 2008](#).

Besides aluminum and aluminum alloys, other materials such as titanium ([Romanova et al. 2016](#)), iron ([Shimizu et al. 2001](#)), steel ([Baydogan et al. 2003](#), [Kubo et al. 2017](#), [Kubo et al. 2018](#)) also have been studied. For example, in [Baydogan et al. 2003](#) a study of deformation-induced surface roughening behavior of two austenitic stainless steel sheets was performed. In the as-received condition, surface roughness of the fine-grained steel turned out to be higher than that of the coarse-grained steel, where the roughness increased gradually during plastic deformation. As was observed before, the rate of roughening was found to be increasing with increasing grain size (coarse-grained steel exhibited rougher surface in comparison to fine-grained one).

There were also a number of roughening studies on copper. In [Meng and Fu 2015](#) a uniaxial tensile test on pure copper sheets with different thicknesses and comparable microstructure was performed. The experimental results reveal that the material flow stress, fracture stress and strain, and the number of microvoids at the fracture surface were reduced with the decreasing ratio of specimen-thickness-to-grain-size. Furthermore, the observation of fracture morphologies confirmed that the local deformation caused by the free surface roughening leads to strain localization and a decreased fracture strain. More studies on copper were done in [Furushima et al. 2014](#), [Luo et al. 2016](#). Roughening of nickel and tantalum was studied in [Guan et al. 2017](#), [Lim et al. 2014](#) and [Lim et al. 2015](#).

As for the types of test used by researchers, a uniaxial tension is the most used experiment for studying the evolution of surface roughening ([Stoudt et al. 2011](#), [Wilson and Lee 2001](#)). In [Shimizu et al. 2001](#) the principal strains of each grain were evaluated.

Then, the relationship between these strains and surface peaks and valleys was discussed. It was also found that surface roughening is closely related to the mutual rotation of crystals. Evolution of roughness during equibiaxial and plane-strain tension using a Marciniak test was studied by [Kubo *et al.* 2018](#). The effect of deformation mode on surface roughening behavior in steels was examined, with the focus on the effect of texture development. Differences in surface roughness development and changes of microstructure were examined under equibiaxial and plane-strain tension, using a macroscopic Marciniak test and microscopic in-situ observations. In addition, the influence of the distribution of crystal orientations on surface roughness development was numerically examined using a CPFЕ analysis. According to their results, roughening was larger for plane-strain tension than for equibiaxial tension regardless of the material, which is due to the larger difference in deformation resistance among crystal grains depending on crystal orientation. They suggested that surface quality after press forming could be improved by reducing the difference in deformation resistance in crystals. More specialized types of forming, such as cup drawing ([Luo *et al.* 2016](#), [Furushima *et al.* 2014](#)) or drawing through dies ([Lo and Horng 1999](#)) have been studied as well.

Among various numerical approaches to modeling surface roughening, the crystal-plasticity models are most commonly used ([Appendix F](#)). In [Turner and Miller 2007](#) the modeling framework was used to study the development of deformation induced surface roughening in thin sheets machined from an aluminum alloy plate. Electron backscatter diffraction experiments were used for material structure characterization, which included crystallographic texture, distributions in grain sizes, and the distribution in intragrain

misorientation. These distributions in structure were incorporated in digital microstructures which represented virtual specimens composed of finite element-discretized crystals. A continuum crystal plasticity model was coupled with the digital microstructures to study the differences in roughening seen in specimens deformed along the rolling direction and transverse direction of the plate material. The success of these simulations built additional insight into how to incorporate material structure into deformation simulations, and built representative virtual specimens that can be used to study the complicated processes that underlie the mechanics of plastic deformation. Similar crystal plasticity approaches were also used in [Becker 1998](#), [Romanova et al. 2016](#), [Wu and Lloyd 2004](#), [Zhao et al. 2004](#), [Zhao et al. 2008](#), [Zhang et al. 2018](#), [Guery et al. 2016](#).

The majority of the studies use based on synthetic grain texture, generated using procedures such as Voronoi tessellation ([Diard et al. 2005](#), [Shenoy et al. 2008](#), [Zhang et al. 2012](#)). Only few studies have attempted to reconstruct the exact arrangement of grains in a given specimen. In ([Zhao et al. 2008](#), [Lim et al. 2014](#), [Lim et al. 2015](#), [Guan et al. 2017](#), [Baudoin et al. 2018](#)) oligocrystal specimens that have one layer of grains through the thickness are considered; in these works, the grain shapes are, or are assumed to be, columnar ([Appendix E](#)). Thus the 3D grains are obtained by extruding through the thickness the 2D grain shapes seen on one of the outer faces. In contrast to these previous efforts, in the present study we also work with an oligocrystal containing one layer of grains. However, in our specimens we could observe that most of the grains are strongly non-columnar. To tackle this, a reconstruction procedure that is based on morphing approach was developed ([Knysh et al. 2019](#)). This made it possible

to incorporate into the model realistic (non-columnar) shapes of the grains based on 2D scans obtained from the top and bottom faces. Since the oligocrystal specimen described in the following sections contains only few grains, having realistic geometries of the grains (in contrast to artificial/simplified geometries) is crucial for capturing the physics of the deformation accurately. In addition, modeling the behavior of realistic texture as accurately as possible is one of the main objectives of current study as it allows assessing predictive capabilities of CPFE our model.

In the following sections we describe the details of the oligocrystal specimen preparation, experimental setup, formulation and calibration of the crystal-plasticity-finite-element (CPFE) model and the finite element (FE) mesh generation. Subsequently, we analyze and compare with experimental data the following features: the deformed shape of the oligocrystal specimen; the surface topographies at the top and bottom faces; derivatives of the elevation; the evolution of average roughness value; the texture and Schmid factor after deformation; and the reorientation of several soft and hard grains of the specimen. In addition, we further validate our CPFE model using data from a polycrystal experiment. Specifically, we construct two artificial representative volume elements (RVE) of the same crystallographic texture and grain size distribution as the actual specimen and simulate the evolution of the average roughness value. Subsequently, we use the same data for discovering relations between the local texture and the elevation of a given grain. These relations provide an alternative interpretation of the surface roughening phenomenon based on the difference in hardness of neighboring grains and, more specifically, on the difference in their Schmid factors.

In comparison to the state-of-art, the present work considers realistic 3D shapes of the grains: since we model the behavior of an actual, non-columnar oligocrystal, it is crucial to work with 3D grain morphologies, instead of extruding a surface scan through the thickness. This accurate volumetric reconstruction is accomplished here by a procedure described and verified in [Knysh *et al.* 2019](#). Also, the adopted crystal-plasticity model uses a fully-analytical Jacobian guarantying quadratic convergence and integrates a dislocation density-based hardening law, which was verified to work well for a number of metals (e.g. [Ardeljan *et al.* 2017](#), [Ardeljan *et al.* 2015](#), [Zecevic and Knezevic 2018](#)). The model is evaluated here for the first time for the prediction of roughness development with plastic strain. The material identification problem was solved efficiently and accurately ([Knysh and Korkolis 2016](#)), with the cost function explicitly defined and minimized, instead of a tedious manual parameter tuning. Finally, the texture-morphology relations obtained here for the polycrystal case were not known previously.

4.2. Experiments

The goals of this work are to study the roughening behavior of an aluminum alloy and to assess the performance of an advanced computational model by comparing its predictions to experiments. It is desired to study the simplest possible problem, and to have a model of as high a fidelity as possible, to be able to highlight its successes and pinpoint its limitations. Therefore, it was decided to study the (macroscopically) uniaxial tension on a flat specimen. This geometry enables easy observations of surface roughening. In selecting the most suitable specimen, a polycrystal could be considered.

Considering that such specimen is used not only for texture measurements, but also for subsequent testing and surface topography analysis, some type of non-destructive, 3D scanning would need to be performed to obtain its exact grain arrangement and texture, which is a challenging task. In addition, the resulting model would contain a significant number of finite elements, making it computationally very expensive. Instead, an oligocrystal specimen that contains relatively few grains arranged in a single layer was selected, avoiding both of these problems.

a. Specimen preparation

The material of this study is the commercially available aluminum alloy AA5052-O, which contains 95.7-97.7 wt.% aluminum and 2.2-2.8 wt.% magnesium ([ASM 1990](#)). The as-received sheet shows a typical rolling texture, see [Appendix D](#). In order to obtain the desired oligocrystal specimen, the following procedure is carried out:

1. An AA5052-O sheet of 0.5 mm thickness is prestrained in uniaxial tension to 10% nominal strain.
2. The plate is heat-treated at 450 °C for 1 hour.
3. Tensile specimens of the geometry shown in [Fig. 4.3](#) are cut from the plate.
4. The tensile specimen thickness is reduced from 0.5 mm to 0.134 mm by polishing.
5. The top and bottom faces of the tensile specimen are polished.

The 4th step was deemed necessary as it was not possible to find a combination of prestraining and heat-treating such that only one layer of grains would appear in the final specimen of 0.5 mm thickness. Therefore, a cycle of scans (see below) and

polishing was performed in sequence, until the same grains appeared on both faces. Of course, this process is limited by the increasing fragility of the resulting specimen with every grinding iteration, and so it was interrupted when an acceptable compromise between identical grains and fragility was found.

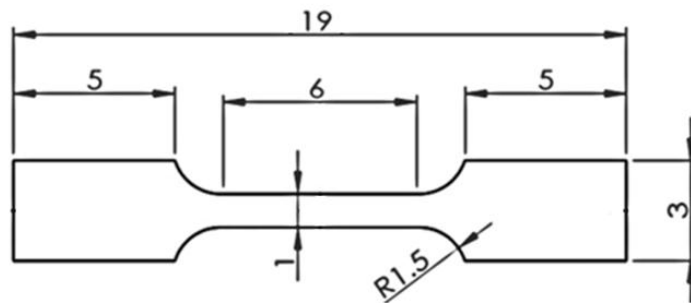
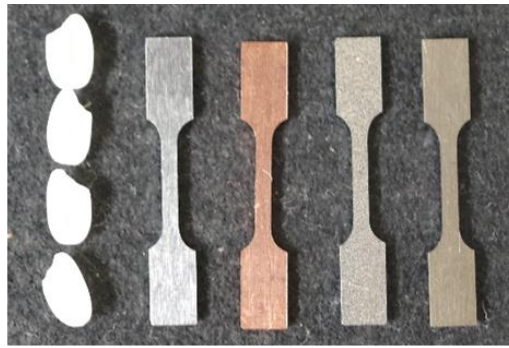


Figure 4.3 – Geometry of the oligocrystal specimen. (Top) Photo showing the relative size of the dogbone in comparison to rice grains on the left. (Bottom) Engineering drawing of the dogbone (dimensions in mm). Thickness is $134\ \mu\text{m}$.

b. Experimental setup

The resultant oligocrystal specimen contains relatively few grains: 38 are those that can be seen on both top and bottom faces of the specimen. For the purposes of this work, it is very important that these grains form one thin layer. This allows us to reconstruct the volumetric grain morphology based only on the planar morphologies visible at the top and bottom faces, i.e., no 3D scanning is needed. A specialized procedure for performing such a reconstruction was developed and its accuracy was verified ([Knysh](#)

et al. 2019). To allow scanning of the texture, the specimen was prepared using the following sequence – #1200 Emery polishing, 3 μm diamond grinding, acetone washing, electrolytic polishing (60% HClO_4 : ethanol = 4 : 45 volume ratio). The actual texture scanning at the top and bottom faces was performed using a HITACHI S-3700N Scanning Electron Microscope (SEM) with Nordlys NL 04-2201-03 Electron Back-Scatter Diffraction (EBSD) system. The shapes and orientations of grains obtained from these scans are shown in Fig. 4.4, and the corresponding Euler angles are provided in Table 4.1. It can be seen that most of the grains form one layer through the thickness, except for relatively few grains that appear either only at the top or only at the bottom and do not go through.

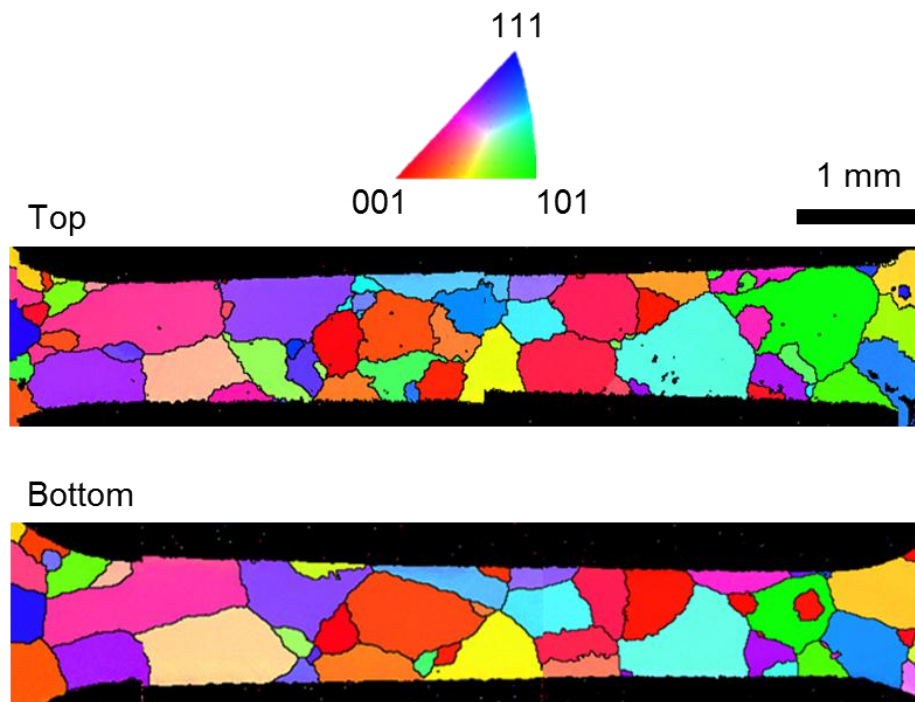


Figure 4.4 – Initial grain structure of the oligocrystal specimen with IPF colors representing grain orientations relative to the sample RD direction according to the colors in the IPF triangle. Scans of top and bottom faces are shown. Scan of bottom face was flipped horizontally for ease of interpretation.

Table 4.1 – Initial grain orientations in the oligocrystal. Bunge Euler angles (φ_1 , Φ , φ_2) in degrees are listed.

Grain #	φ_1	Φ	φ_2
1	343.1	36.2	58.7
2	170.4	7.5	78.5
3	155	30.6	3.6
4	122.1	37.9	0.5
5	37.9	23.7	84.3
6	342.9	20.6	81.4
7	33.1	23.1	56.9
8	44.3	43.6	37.9
9	192	38	80.8
10	235.8	38.7	38.9
11	227.7	32.4	36.1
12	322.2	30.7	46.8
13	82.8	25.7	30.8
14	247.4	26.5	14.3
15	328.5	41.5	54.4
16	215.5	11.4	23.8
17	354.9	42.7	5.6
18	169.4	19.3	83.3
19	258.1	51	45.5
20	340.4	36.1	17.9
21	233.7	48.4	58.1
22	209.9	41.4	7.1
23	38.5	25.7	15
24	185.8	16.9	60.4
25	37.7	14.8	40.8
26	202.9	29.6	76.9

27	7.3	33.8	83.9
28	89.1	14.4	53.3
29	302.1	19.6	76.5
30	352	10.7	54
31	283.2	24.4	9
32	314.7	33.3	36.4
33	229.9	28.8	84.7
34	181	43.6	53.4
35	77.8	51	53.2
36	337.2	15.8	48.8
37	154.4	10.2	7.2
38	263.7	6.1	6.9

The oligocrystal specimen was plastically deformed in uniaxial tension. A Zwick/Roell Universal Testing Machine of 5 kN force capacity and equipped with a laser extensometer laserXtens was used. The specimens were tested under displacement-control, at a nominal strain-rate of $5 \times 10^{-4} \text{ s}^{-1}$. The resultant nominal strain in the gauge region of the specimen was $\sim 10\%$. Such value of strain induces a vivid, observable change in the surface topography. At the same time, this strain is small enough to avoid necking or fracture.

The surface topography was obtained with a KEYENCE VK-X100 laser confocal microscope. The lateral resolution of the microscope is $0.01 \mu\text{m}$, the vertical resolution is $0.005 \mu\text{m}$ ([KEYENCE VK-X100 Specifications](#)). The data obtained is an array of points that can be visualized as a 3D or contour plot for further comparison and analysis.

4.3. Modeling

a. Crystal-plasticity finite element (CPFE) model overview

In order to capture the physics of crystal plasticity, we use the crystal-plasticity-based constitutive law originally developed in [Kalidindi *et al.*, 1992](#), and later advanced with dislocation-density-based hardening ([Ardeljan *et al.*, 2014](#)). This model represents purely mechanical effects, e.g., not deformation-induced heating ([Knysh and Korkolis 2015](#)) or other effects, which is an acceptable assumption for this aluminum alloy. For completeness, in this section we summarize this model.

The total deformation gradient \mathbf{F} can be decomposed into elastic (\mathbf{F}^*) and plastic (\mathbf{F}^p) components:

$$\mathbf{F} = \mathbf{F}^* \mathbf{F}^p. \quad (4.1)$$

The elastic component \mathbf{F}^* is related to stress by Hooke's law:

$$\mathbf{T}^* = \mathbf{C} \mathbf{E}^* \quad \text{or} \quad \mathbf{T}^* = \mathbf{F}^{*-1} [(\det \mathbf{F}^*) \boldsymbol{\sigma}] \mathbf{F}^{*-T} \quad \text{with} \quad \mathbf{E}^* = \frac{1}{2} (\mathbf{F}^{*T} \mathbf{F}^* - \mathbf{I}) \quad (4.2)$$

where \mathbf{T}^* and \mathbf{E}^* are Piola-Kirchhoff stress tensor and Green-Lagrange finite strain tensor, respectively (that form work-conjugate stress and strain measures), \mathbf{C} is the 4th-order elasticity tensor and $\boldsymbol{\sigma}$ is the Cauchy stress tensor.

The evolution of plastic component of the deformation gradient due to slip is given by:

$$\dot{\mathbf{F}}^p = \mathbf{L}^p \mathbf{F}^p, \quad (4.3)$$

where \mathbf{L}^p is the plastic velocity gradient, that can be represented as:

$$\mathbf{L}^p = \sum_{\alpha} \dot{\gamma}^{\alpha} \mathbf{b}_0^{\alpha} \otimes \mathbf{n}_0^{\alpha}. \quad (4.4)$$

In this equation, the vectors \mathbf{b}_0^{α} and \mathbf{n}_0^{α} indicate the slip-direction and the slip-plane

normal, for a given slip system α . The term $\dot{\gamma}^\alpha$ is the shearing-rate of slip system α , that can be expressed with the following power-law relationship:

$$\dot{\gamma}^\alpha = \dot{\gamma}_0 \left(\frac{|\tau^\alpha|}{\tau_c^\alpha} \right)^{1/m} \text{sign}(\tau^\alpha), \quad (4.5)$$

where $\dot{\gamma}_0 = 0.001 \text{ s}^{-1}$ is a reference slip-rate, $m = 0.05$ is a power-law exponent (Knezevic *et al.*, 2016) ensuring proper selection of active slip systems for accommodating the imposed plastic strain, τ^α is the resolved shear stress and τ_c^α is the characteristic resistance shear stress. The latter is assumed in this work that can be decomposed into 4 different contributions:

$$\tau_c^\alpha = \tau_{o,f} + \tau_{o,HP} + \tau_{for}^\alpha + \tau_{sub}. \quad (4.6)$$

The four terms in Eq. (4.6) represent different physical aspects: $\tau_{o,f}$ is a friction term also called initial slip resistance, $\tau_{o,HP}$ is a barrier- effect term, τ_{for}^α and τ_{sub} are the contributions from interaction of dislocations. The latter are assumed to involve forest and substructure interactions. Notice that from the four mechanisms that affect τ_c^α , only one is slip-system-dependent. The term $\tau_{o,HP}$ can be expressed using the Hall-Petch relationship (Hall 1951, Petch 1953):

$$\tau_{o,HP} = \mu H \sqrt{\frac{b}{d_g}}, \quad (4.7)$$

where μ is the shear modulus, $H = 0.136$ is the Hall-Petch parameter, b is the Burgers vector and $d_g = 10.3 \mu\text{m}$ is the average grain diameter calculated using the ASTM standard E112-13 (ASTM 2013). The terms τ_{for}^α and τ_{sub} are obtained from the following relations:

$$\tau_{for}^{\alpha} = \chi b \mu \sqrt{\rho_{for}^{\alpha}}, \quad (4.8)$$

$$\tau_{sub} = k_{sub} b \mu \sqrt{\rho_{sub}} \log\left(\frac{1}{b \sqrt{\rho_{sub}}}\right), \quad (4.9)$$

where $\chi = 0.9$ is a dislocation interaction parameter and $k_{sub} = 0.086$ is a parameter that ensures that Eq. (4.5) recovers the Taylor law at low dislocation densities.

The last two equations contain non-proportional relationships between the components of the resistance shear stress and the forest and substructure dislocation densities. The forest density ρ_{for}^{α} evolves in the following way:

$$\frac{\partial \rho_{for}^{\alpha}}{\partial \gamma^{\alpha}} = k_1 \sqrt{\rho_{for}^{\alpha}} - k_2 \rho_{for}^{\alpha}, \quad (4.10)$$

where k_1 is a coefficient for the rate of dislocation storage (also called trapping-rate coefficient, see Table 4.2) and k_2 is the coefficient for the rate of dynamic recovery. In turn, these two coefficients follow the relation:

$$\frac{k_2}{k_1} = \frac{\chi b}{g} \left[1 - \frac{k T}{D b^3} \ln\left(\frac{\dot{\epsilon}}{\dot{\epsilon}_0}\right) \right], \quad (4.11)$$

where $k = 1.38 \times 10^{-23} \text{ JK}^{-1}$, $\dot{\epsilon}_0 = 0.001 \text{ s}^{-1}$, g , D and $T = 298 \text{ K}$ are the Boltzmann's constant, a reference strain-rate, an activation barrier, the drag stress and the room temperature, respectively. The substructure density increase is proportional to the rate of dynamic recovery of all active dislocations via:

$$\Delta \rho_{sub} = q b k_2 \sum_{\alpha} \rho_{for}^{\alpha} |\Delta \gamma^{\alpha}|, \quad (4.12)$$

where q is a fitting coefficient representing the fraction of α -type dislocations that do not annihilate but form substructures.

Table 4.2 – Material parameters of AA5052-O alloy.

Parameter	Symbol	Value	Unit	Comment
Aluminum crystal elastic constants	C_{1111}	107,300	MPa	Simmons and Wang 1970
	C_{1122}	60,900	MPa	Simmons and Wang 1970
	$2C_{2323}$	56,600	MPa	Simmons and Wang 1970
Initial slip resistance	$\tau_{0,f}$	32.6	MPa	Optimization
Shear modulus	μ	26,100	MPa	Zecevic and Knezevic 2015
Burgers vector	b	0.286	nm	Zecevic and Knezevic 2015
Trapping rate coefficient	k_1	6.376×10^7	m^{-1}	Optimization
Activation barrier	g	0.005283	-	Optimization
Drag stress	D	1,535	MPa	Optimization
Dislocation recovery rate	q	16	-	Zecevic and Knezevic 2015

The initial value of forest density ρ_{for}^α is set to $10^{10} m^{-2}$, typical for annealed FCC metals. The substructure density ρ_{sub} theoretically initiates from 0, but numerically starts from the value of $0.1 m^{-2}$. Both densities subsequently evolve according to [Eq. \(4.10\)](#) and [Eq. \(4.12\)](#).

b. Identification of material properties

The crystal-plasticity framework described above is implemented in a user-material subroutine (UMAT) that is called within ABAQUS. The UMAT needs access to texture

information (Euler angles for each individual grain) as well as material properties. Many of these properties, such as the elastic constants C_{ijkl} , shear modulus μ , Burgers vector b and dislocation recovery-rate q are reported in the literature (Table 4.2). However, four material constants that enter Eq. (4.6) need to be identified for our specific material (AA5052-O).

Apart from specialized methods (Guery *et al.*, 2016), the identification of unknown material parameters is often done manually by trial and error – until the response of the model (for a chosen loading case) is matching the corresponding experimental response. Since in our case every trial is associated with running a CPFEM simulation, this could be an acceptable method for identifying one unknown parameter, however it becomes very tedious and inefficient when we deal with four parameters. Therefore, we automated the material identification problem by considering it as an optimization problem. The corresponding objective function is a Python function assembled from several stages, as illustrated in Fig. 4.5. This function reads a vector x of the four unknown parameters as an input and runs a FE simulation of uniaxial tension of a polycrystal block made out of 4096 C3D8 elements, where each element corresponds to a single crystal. The experimentally measured crystallographic texture of the polycrystal (see Appendix D) is used in the FE simulation. Subsequently, the objective function compares how well the corresponding nominal stress-strain curve matches with the experimental response of the corresponding polycrystal and returns the integral error ($E = \int_0^\epsilon |\sigma_{FE} - \sigma_{exp}| d\epsilon$) between these two curves. The optimization goal is to minimize the value of E .

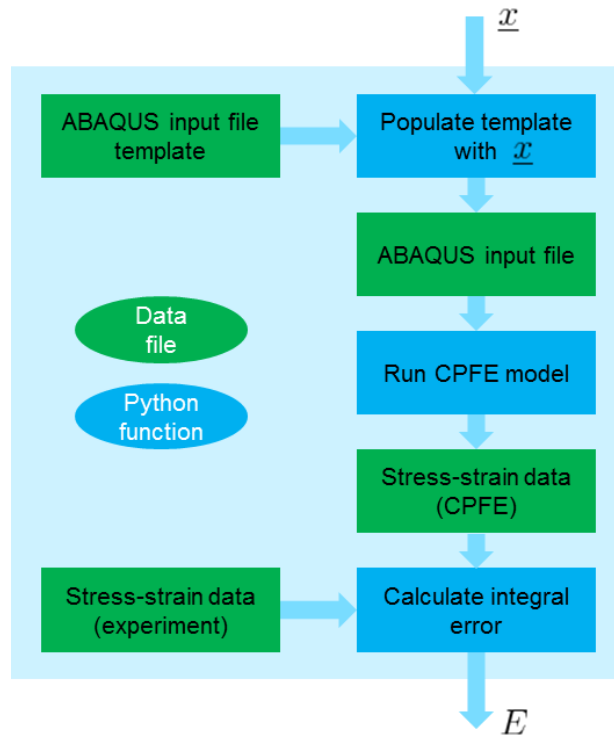


Figure 4.5 – A schematic of the objective function used in optimization procedure, where \underline{x} is the vector of input parameters and E is the scalar error value (output).

In order to solve this optimization task we use “blackbox” – an optimization method (Knysh and Korkolis 2016) specifically designed for black-box functions (ones that have input-output nature) that are expensive to evaluate. The method was successfully used previously for identification of post-necking hardening behavior of stainless steel across a range of strain-rates and temperatures in a fully-coupled way (Knysh and Korkolis 2017). Since the method itself is also implemented as a Python module, it can be easily integrated into the current problem. The values of the four material constants identified in this way are listed in Table 4.2. The final matching obtained between the experiment and the FE model prediction with the optimized material parameters is shown in Fig. 4.6. The total number of function evaluations used is 150, i.e., after this number is reached, the current solution (i.e., the current set of the four material constants) is taken

as the optimum. This solution was verified by running the optimization procedure a few times. Since the procedure involves random numbers, each new run started with different initial samples. The same result was obtained consistently.

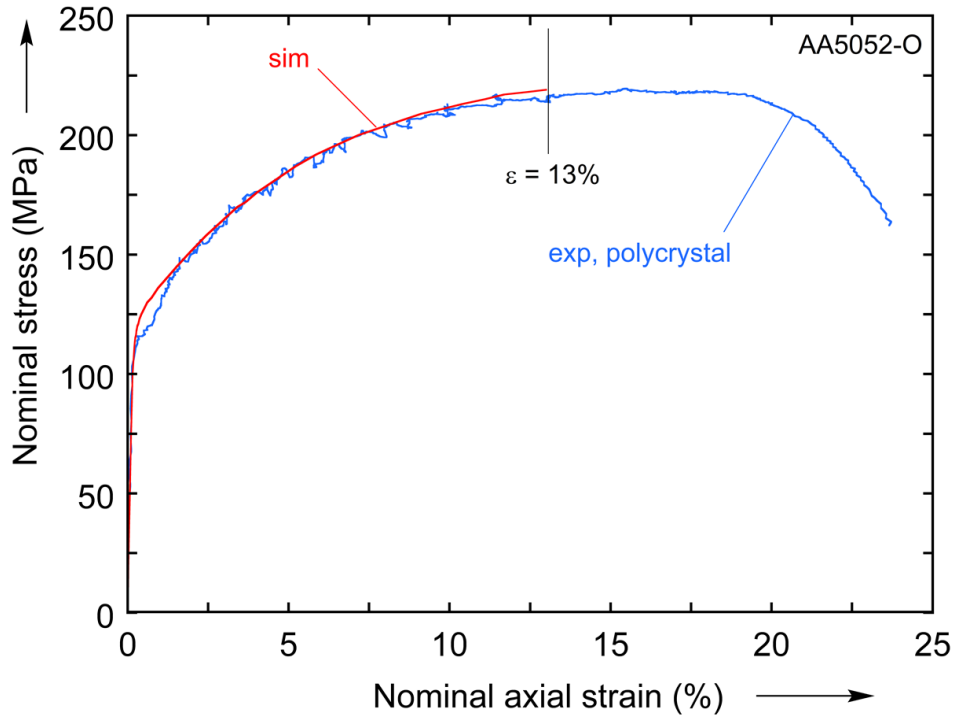


Figure 4.6 – Measured and predicted stress-strain curves for a polycrystal, that are used for calculating corresponding error value ($E = \int_0^{\epsilon} |\sigma_{FEA} - \sigma_{exp}| d\epsilon$). The plot shows the match between two curves after the 4 unknown parameters were identified.

c. Mesh construction

As was mentioned before, working with a thin oligocrystal specimen that has essentially one layer of grains through the thickness allows to not only to lower computational cost, but also to obtain the exact arrangement of grains without the need to perform a 3D scan. In this way, the volumetric shape of each grain can be accurately represented based on its “footprints” at the top and bottom faces of the specimen (Fig. 4.7).

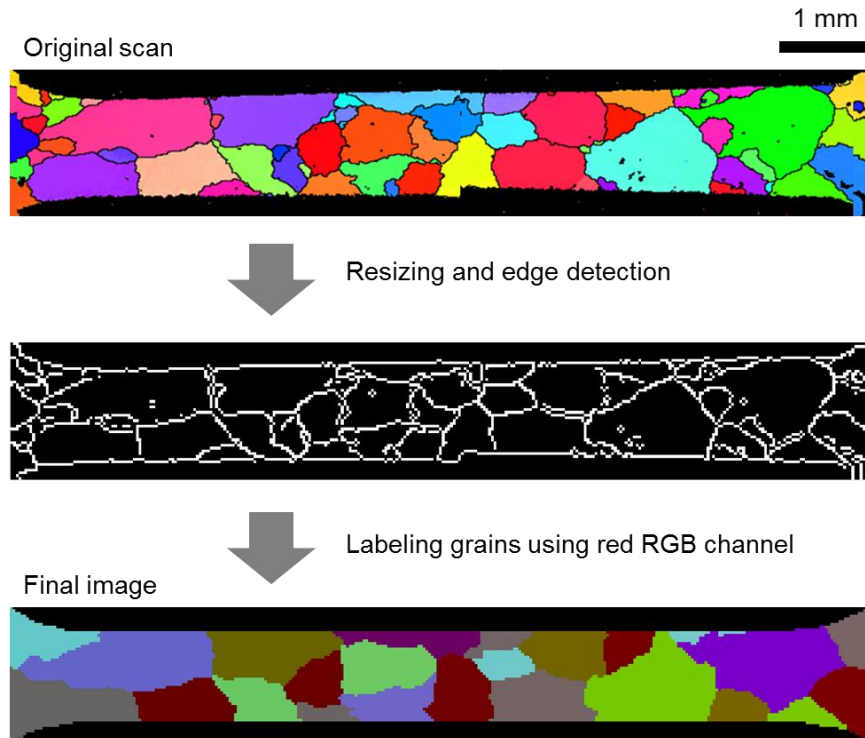


Figure 4.7 – Preparation steps that are applied in order to obtain clear images of top and bottom faces (subsequently used in reconstruction procedure).

A simple and robust procedure based on a morphing approach that allows such a reconstruction has been developed (Knysh *et al.*, *subm.*). The input to the procedure is a set (in our case, a pair) of images that contain matching colors. Each color corresponds to a volumetric phase, e.g., in this case a grain. The output is a set of intermediate images which, when stacked on top of each other, form the desired 3D shape. The accuracy of the procedure was successfully verified through destructive testing, with revealed that the predicted grain outlines at various depths from the outer faces were indeed close to the observed ones (Knysh *et al.*, *subm.*).

As can be seen in Fig. 4.7, the EBSD scans of the top and bottom faces of the specimen contain noise. This is seen as small fluctuations of Red-Green-Blue (RGB) values within the same grain, black dots, fuzzy grain boundaries, etc. Since the

reconstruction procedure requires colors in the input images to be “clean”, all unwanted noise is removed by the 2 steps illustrated in [Fig. 4.7](#) and explained below.

The first step consists of two substeps. The first substep is to resize the EBSD images ([Fig. 4.7](#), top) to the desired resolution (we picked 316×50 for our case) depending on how many finite elements are expected. The second substep is to obtain binary (black and white) images containing only the grain boundaries ([Fig. 4.7](#), mid). This is accomplished using the built-in function “EdgeDetect” within the Mathematica computational environment. Since the binary images obtained in this way are still polluted by some residual lines and dots, an additional image cleanup is done manually.

The second step is to assign each grain its unique color. A simple fill function of any raster graphics editor (for example, MS Paint) can be used for that purpose. For further mesh generation steps it is very convenient to keep the information about grain numbers within the image itself. In order to do this, the grain number is stored in a red RGB channel (i.e., green and blue channel values can be chosen randomly). Finally, a script that removes the grain boundaries is applied. The image obtained after these steps is clean, as shown in [Fig. 4.7](#), bottom, and can now be used as an input to the reconstruction procedure proposed in ([Knysh *et al.*, *subm.*](#)).

The result of applying the reconstruction procedure is a 3D voxel model of the specimen of [Fig. 4.4](#), shown in [Fig. 4.8](#). As can be seen from the perspective view, the 3D shapes of the grains are basically interpolated between their projections at the top and bottom faces. The resolution of the voxel mesh is $316 \times 50 \times 6$, which results in almost 100,000 finite elements (each voxel represents an element).

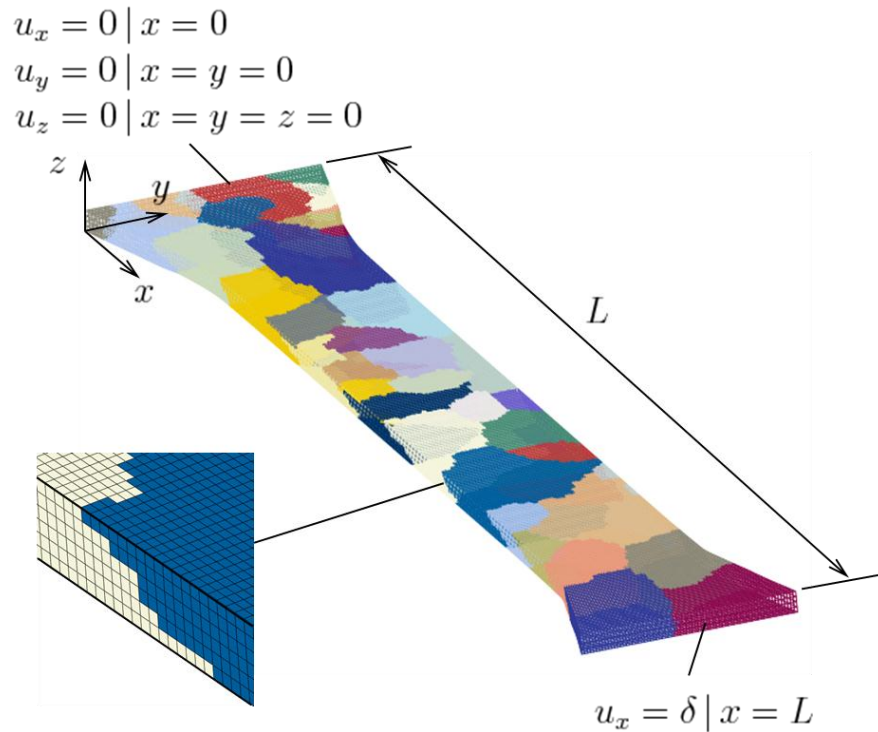


Figure 4.8 – A reconstructed non-columnar voxel model of the oligocrystal specimen and its boundary conditions, also showing the finite element mesh.

d. Finite element model

This model is created in the commercial, non-linear, implicit code Abaqus/Standard. The element type used is linear with full integration, or C3D8 in Abaqus' terminology. For the geometric modeling, part of the specimen shoulders, i.e., not only the gauge region, are included. This is to enable the enforcement of boundary conditions; due to deformation-induced roughening, in the plastically-deforming regions flat faces do not remain flat; on the other hand, the material at the shoulders is expected to remain elastic, so this issue would be minimized. The boundary conditions implemented are shown in Fig. 4.8, as well. Displacements are prescribed at both ends. In addition, a vertical edge and its adjacent vertex are fixed (i.e., given zero displacements), in order to prevent rigid body motion. As mentioned earlier, the crystal-plasticity material model is introduced to the

simulation through a UMAT. The only difference from the values mentioned in [Section 4.3a](#) and/or listed in [Table 4.2](#) is the average grain size d_g used in [Eq. \(4.7\)](#). While for the identification this was set to $10.3 \mu m$, appropriate for the as-received polycrystal, for the surface roughening simulations it was set to $395 \mu m$, this time appropriate for the oligocrystal in hand.

4.4. Comparison between experiment and model

The objective of this work is to assess the predictive capabilities of CPFE by simulating a specific specimen as realistically as possible and comparing the numerical results to the experiments. The first feature that can be extracted from the CPFE simulation is the overall shape of the deformed specimen at 10% nominal strain, shown in [Fig. 4.9](#). In that figure, a deformation scale factor of 2 is used to illustrate the post-deformation curvature of the surfaces and edges of the specimen, that initially were flat and straight, respectively. The equivalent plastic strain field is also shown in that figure, even though full-field strain measurement techniques (such as Digital Image Correlation) were not used in the experiment, therefore it is not possible to perform a direct comparison. It is however interesting to note that the deformation of this oligocrystal specimen is very inhomogeneous, with some areas having experienced significant deformation and others not. This will be revisited in more detail later. It also highlights the difficulty of performing these experiments, as, depending on the grain arrangement, orientation and proximity to the fillets, in many experiments the deformation was concentrated in a single grain, and no significant roughening could be observed outside of it, rendering them useless for this work.

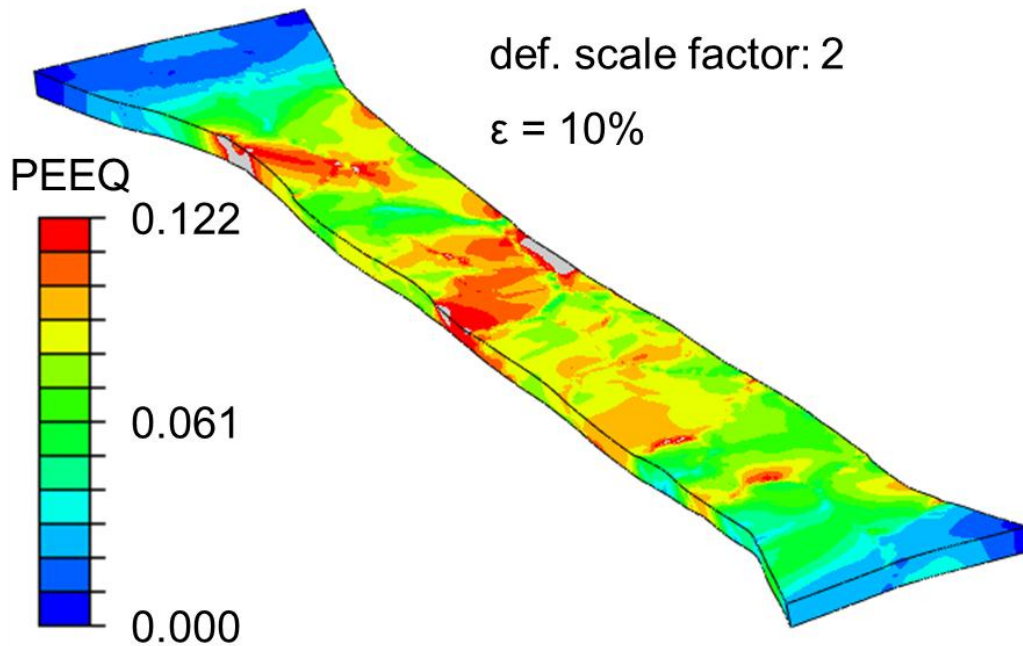


Figure 4.9 – Prediction of the distribution of equivalent plastic strain (PEEQ) in the oligocrystal specimen. A deformation scale factor of 2 is used in order to exaggerate deformed shape, for easier visualization.

Figure 4.10 shows the predicted 3D shape and out-of-plane displacement field of the deformed specimen at 10% nominal strain, with a deformation scale factor of 2 for illustration purposes. We also show two cross-sectional cuts along the gauge area, from which a mild corrugation effect can be observed – thickness remains more or less constant, while the mid-plane is wavy. While intuition perhaps suggests that the mid-plane should remain flat and thickness should reduce from grain to grain, it turns out that in our thin specimen corrugation is more favorable from the equilibrium point of view.

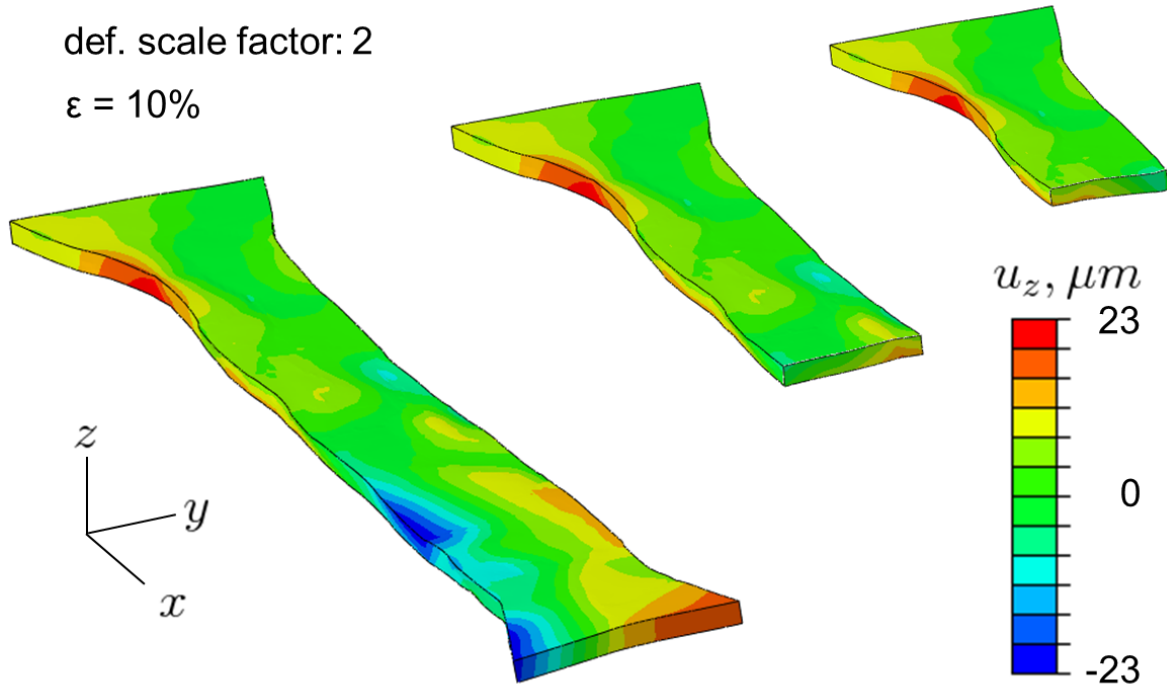


Figure 4.10 – Prediction of the deformed shape of the oligocrystal specimen along with the distribution of z-displacements (u_z). Two cross-sectional views are shown. A deformation scale factor of 2 is used in order to exaggerate deformed shape, for easier visualization.

A quantitative comparison of the surface topography of the deformed specimen from the CPFE model with the experimental results obtained using the laser confocal microscope is given in Fig. 4.11. The comparisons are given for both the top and bottom surfaces of the specimen. Included in that figure are the outlines of the grains. The absolute difference between model and experiment is shown in Fig. 4.11. In addition we can also introduce the relative error between out-of-plane displacement values u_{exp} and u_{sim} based on the following formula:

$$E = \frac{|u_{exp} - u_{sim}|}{\frac{1}{2}|u_{exp} + u_{sim}|} = 2 \frac{|u_{exp} - u_{sim}|}{|u_{exp} + u_{sim}|} \quad (4.13)$$

When both u_{exp} and u_{sim} have the same sign (direction of displacement is predicted

correctly), the value of E is less than 2. Otherwise (when direction is not predicted) the value of E is greater than 2. Areas with correctly predicted displacement direction (0-2 error range in Fig 4.12) occupy 71.5% of the top surface area and 57.8% of the bottom surface area. Meanwhile, areas with error value below 0.5 occupy 28.9% of the top surface area and 16.6% of the bottom surface area (see 0-0.5 error range in Fig 4.12).

Based on the values provided above, it can be concluded that the predicted and measured surface morphologies do not agree well. As this study involves many elaborated steps (both experimentally and numerically), there can be several reasons why such discrepancy occurs. One possible reason is the fact that several grains (mostly small, but few larger ones as well) appeared only in one of the two faces and did not go all the way through the thickness (Fig. 4.4). Since such grains could not be simply removed from the model (which would result in cavities), the reconstruction procedure made these areas being occupied with neighboring grains. That affected the shapes of corresponding grains and therefore also might have affected the predicted deformation at these local areas. Another possible reason is that very thin specimen ($134\ \mu\text{m}$) could possibly be bent or twisted while being placed into the scanning area for surface elevation measurements. In addition, the ability of the model to capture grain deformation accurately could be further validated by modeling a specimen that contains very few grains (1-3). Also, cohesive zone elements can potentially be used in order to model physics of grain boundaries more accurately. Finally, strain gradient crystal plasticity formulation would help to improve the predictions.

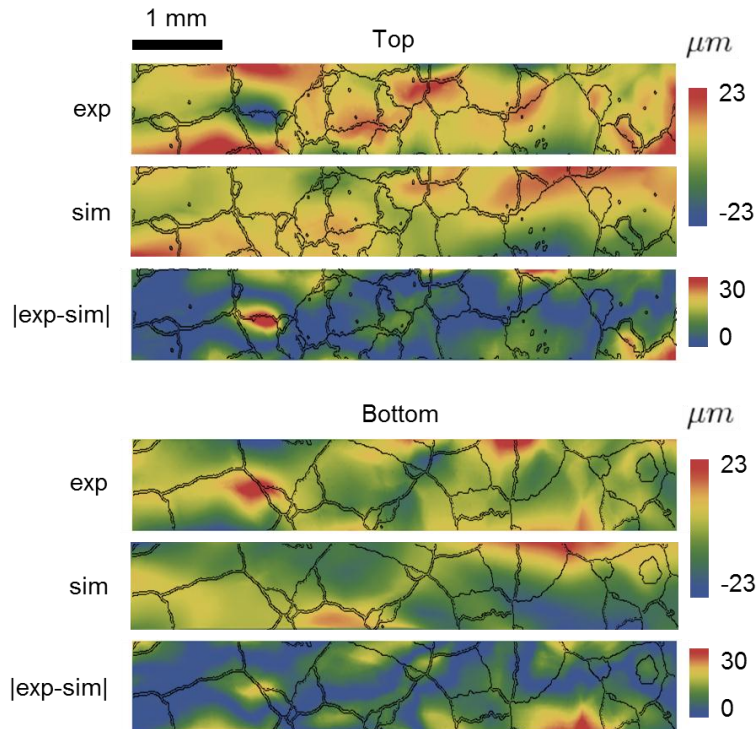


Figure 4.11 – Surface topographies at the top and bottom faces of the specimen, extracted from simulation (marked as “sim”) and experiment (marked as “exp”) at 10% nominal strain. The absolute difference plots (marked as “|exp-sim|”) are shown, as well.

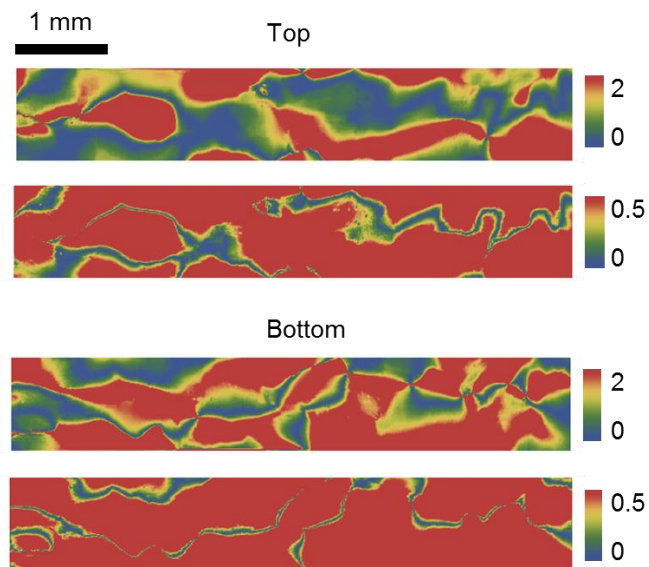


Figure 4.12 – Relative error between simulation and experiment at 10% nominal strain. Error of less than 2 indicates correctly predicted displacement direction.

One interesting fact that can be observed from [Fig. 4.11](#) is that peaks and valleys of the surface normally occur in the areas adjacent to grain boundaries and close to the free edges of the specimen. This can be explained as follows. Because the specimen is thin, most of the grains have planar shapes. If we performed a virtual tension test (holding the ends to be coplanar) on an isolated grain (not considering its interaction with neighbors), we would observe that the grain is naturally tilting one way or another due to slip. Once we consider grain interactions, all grain boundaries start acting as kinematic constraints that cause discontinuities in mechanical fields. It can be expected that extreme values of these fields (including displacements, and therefore surface elevation) occur at the grain boundaries, not within the grains. This reasoning further explains the corrugation effect that can be seen in [Fig. 4.10](#).

As the direct strain fields from the experiment are not available, in order to estimate the strain-related performance of the CPFEM, the surface elevation derivatives $\partial u_z/\partial x$ and $\partial u_z/\partial y$ are shown in [Figs. 4.13 and 4.14](#), for the top and bottom faces ([Baudoin and Hama 2018](#)). Note that these derivatives are related to the out-of-plane shear components of the strain tensor.

It is visible from [Figs. 4.13 and 4.14](#) that the elevation derivatives were not predicted well everywhere, which is because the surface elevation ([Fig. 4.11](#)) was not predicted well in the first place due to the possible reasons addressed above.

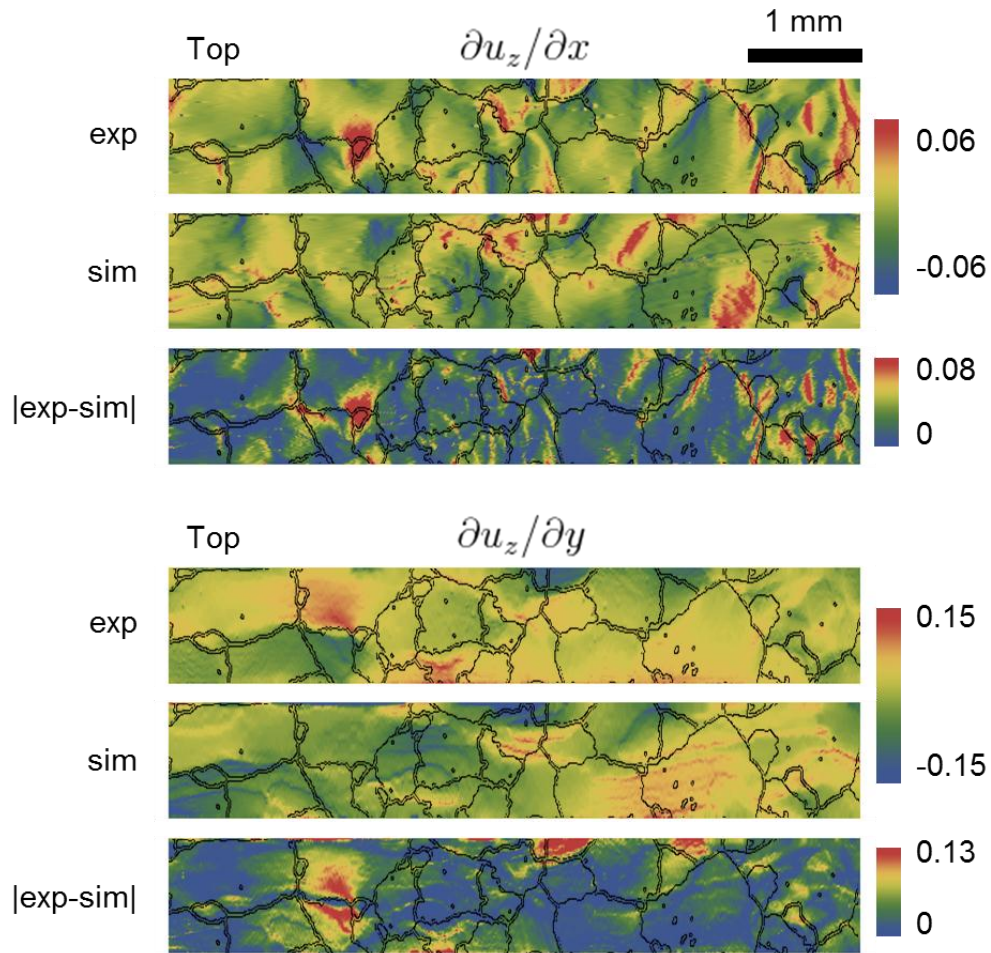


Figure 4.13 – Elevation derivatives at the top face of the specimen, extracted from simulation (marked as “sim”) and experiment (marked as “exp”) at 10% nominal strain. The absolute difference plots (marked as “|exp-sim|”) are shown, as well.

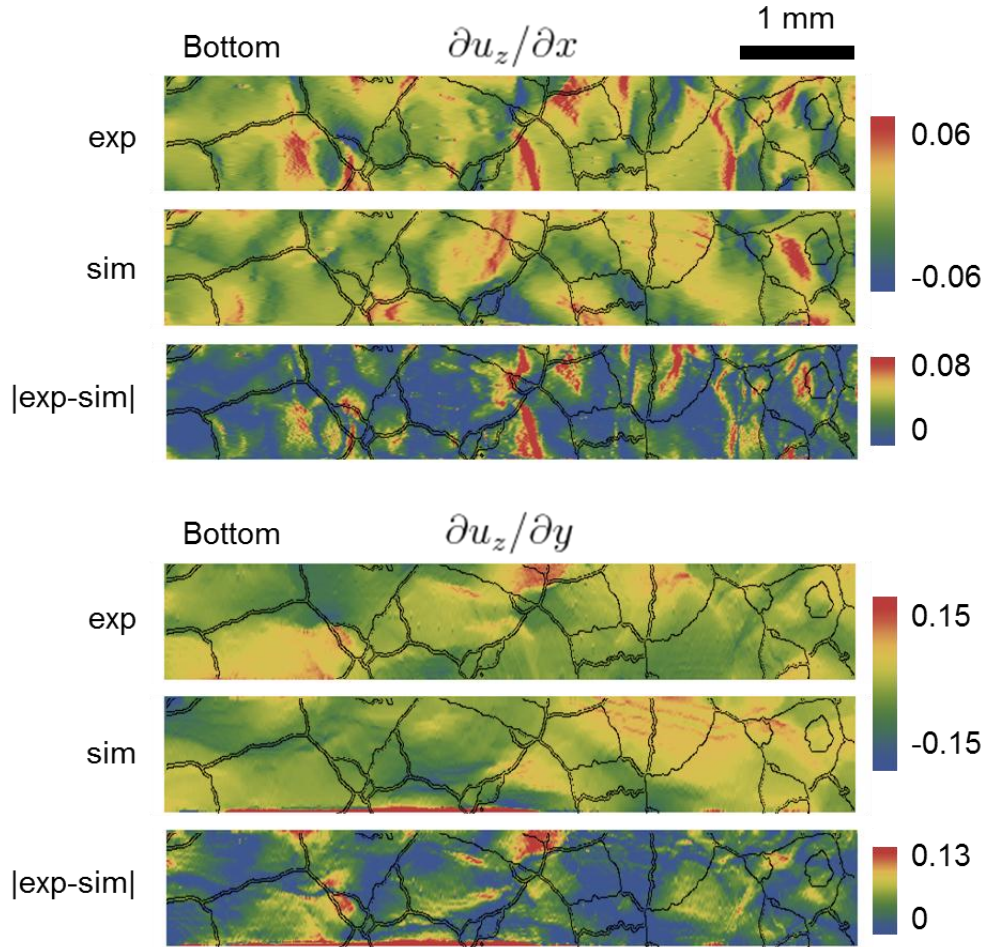


Figure 4.14 – Elevation derivatives at the bottom face of the specimen, extracted from simulation (marked as “sim”) and experiment (marked as “exp”) at 10% nominal strain. The absolute difference plots (marked as “|exp-sim|”) are shown, as well.

The average surface roughness can be defined in the following way:

$$S_A = \frac{1}{A} \int_A |z - \bar{z}| dA, \quad (4.14)$$

where A is the area of interest, and $z(x, y)$ and \bar{z} are the current and average elevation of the surface respectively. Based on this definition, another result that can be discussed is the evolution of S_A with the macroscopically-applied axial strain, see [Fig. 4.15](#). Experimental values of S_A were calculated by converting images of surface profiles

(along with corresponding color bars) into elevation data sets and subsequently applying Eq. (4.14). The dependence obtained is very close to linear, which is in accordance with the previous studies (Osakada and Oyane 1971, Becker 1998, Wilson and Lee 2001).

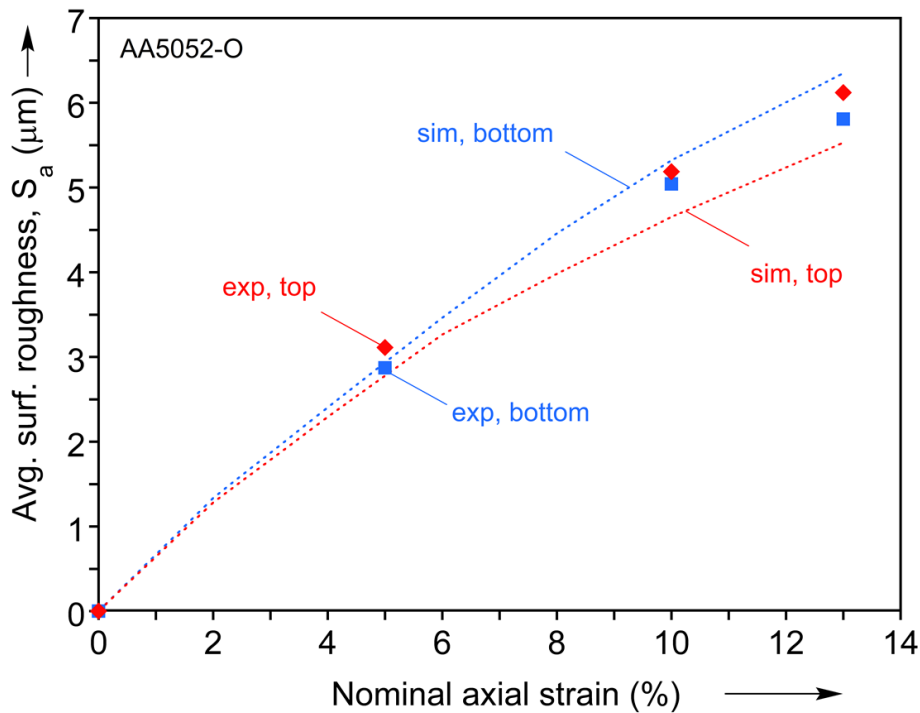


Figure 4.15 – Evolution of average surface roughness (S_a) at the top and bottom faces of the specimen with nominal strain, extracted from simulation and experiment.

A further assessment of the ability of the CPFEM model to represent reality is by comparing the predicted texture to the EBSD measurements of the specimen after the test. During the simulation, the Euler angles are stored at each integration point of the mesh. These Euler angles were visualized with the MTEX toolbox available in MATLAB. As a result, the corresponding inverse pole figure (IPF) color maps before and after deformation and at the top and bottom faces (Fig. 4.16 and Fig. 4.17, respectively) were obtained. Overall, a good agreement between experiment and prediction is observed.

Some minor local disagreement is primarily caused by the fact that the specimen prepared contained several small grains that did not go through the thickness and were only present at one of the faces (as can be seen in Figs. 4.16 and 4.17). Such grains were not included into the CPFÉ model and their volume was occupied by neighboring grains. In the simulation results, some areas adjacent to grain boundaries contain local regions with random orientations. These random orientations are due to numerical instabilities and are visible as noisy colors (e.g., at the “Top, Final” and “Bottom, Final” images in Figs. 4.16 and 4.17).

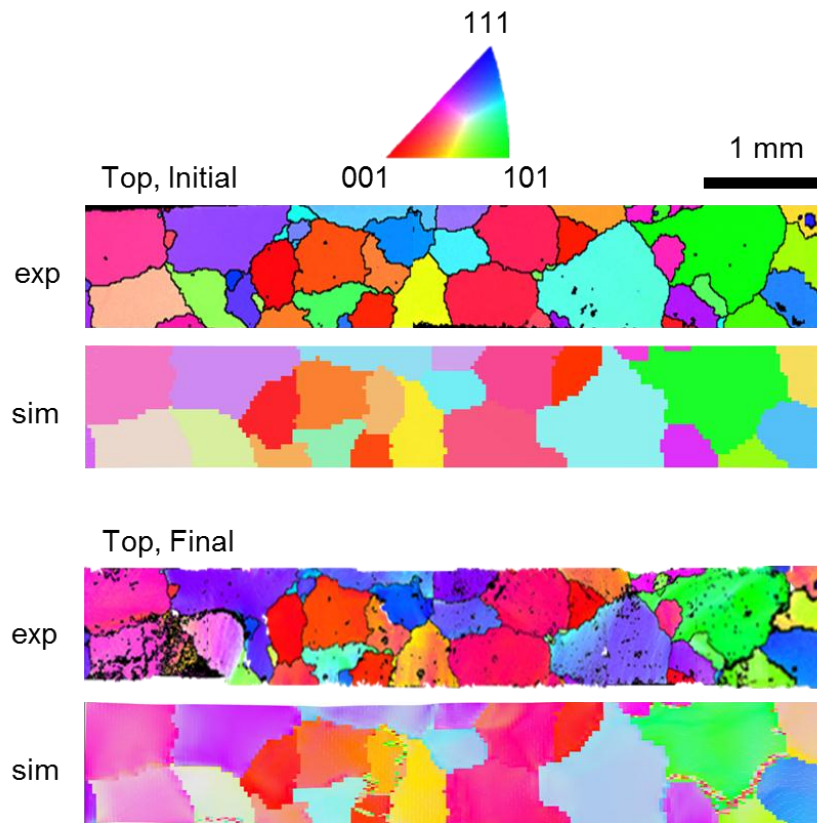


Figure 4.16 – Initial and final (at 10% nominal strain) structures at the top face of the specimen, extracted from simulation (marked as “sim”) and experiment (marked as “exp”).

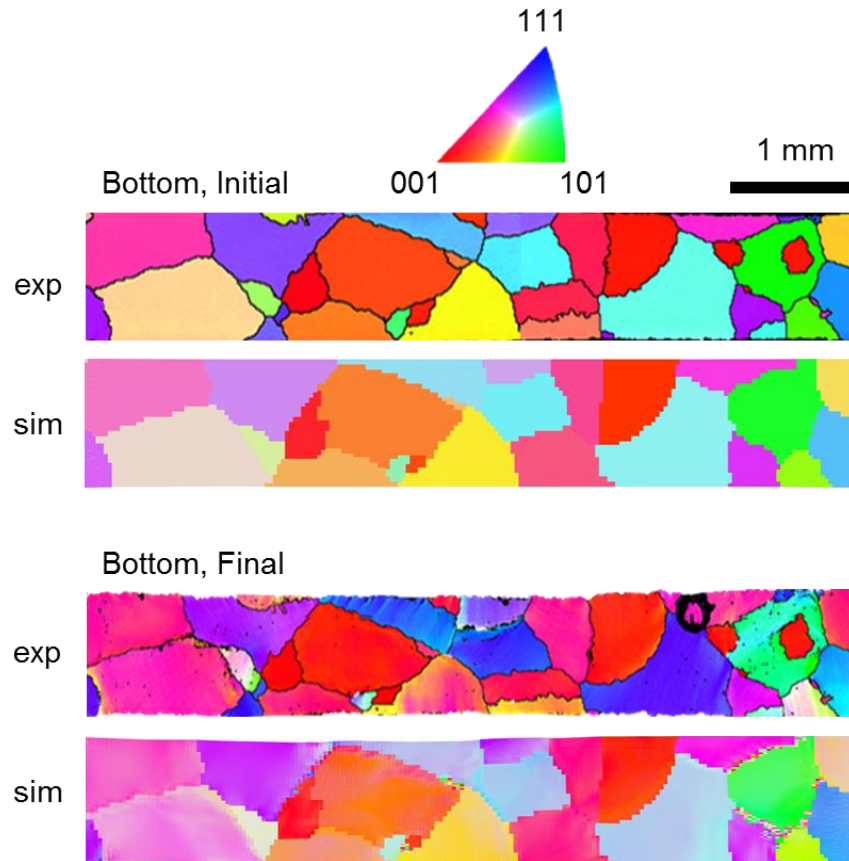


Figure 4.17 – Initial and final (at 10% nominal strain) structures at the bottom face of the specimen, extracted from simulation (marked as “sim”) and experiment (marked as “exp”).

To further illustrate the physics of texture evolution, the reorientation (after 10% nominal strain) of a few soft and hard grains during deformation is shown in Fig. 4.18. The texture evolution for each grain is represented by a solid arrow in the IPF. Cubes that illustrate the orientation of the unit cell of a given grain as well as EBSD scans of the entire specimen are shown with respect to the same global coordinate system. As can be observed, soft grains (i.e., those with colors that are close to the center of IPF color map, here grains 9, 21 and 25) are more prone to reorientation (Hosford 2010), while hard grains (i.e., those with colors that are further away from the center, here grains 23 and 27) do not reorient much (Hosford 2010). In addition, to further examine

how the predicted texture matches the measured one, a reorientation graph (after 10% nominal strain) for the five softest grains in the specimen is shown in Fig. 4.19. In that figure, solid arrows correspond to experimental measurements and dashed arrows to CPFЕ predictions. An overall agreement between measurements and simulation results is observed visually. To quantify the level of agreement, we can introduce the following metric for vectors (arrows) that represents change in IPF colors:

$$\Delta = \frac{|\vec{a}_{sim} - \vec{a}_{exp}|}{|\vec{a}_{sim} + \vec{a}_{exp}|} \quad (4.15)$$

where \vec{a}_{exp} and \vec{a}_{sim} are vectors representing measured and predicted IPF color change in Fig. 4.19. When both vectors match perfectly, the value Δ is going to be 0. When both vectors are of the same magnitude, but orthogonal to each other (or when one of the vectors has zero magnitude) the value of Δ is going to be 1. Table 4.3 provides values of Δ calculated for each of 5 pairs, as well as average value.

Table 4.3 – Level of agreement between predicted and measured reorientations.

Grain #	Δ (Top)	Δ (Bottom)
9	0.12	0.20
10	0.49	0.26
16	0.13	0.11
21	0.36	0.43
25	0.42	0.42
Average	0.29	

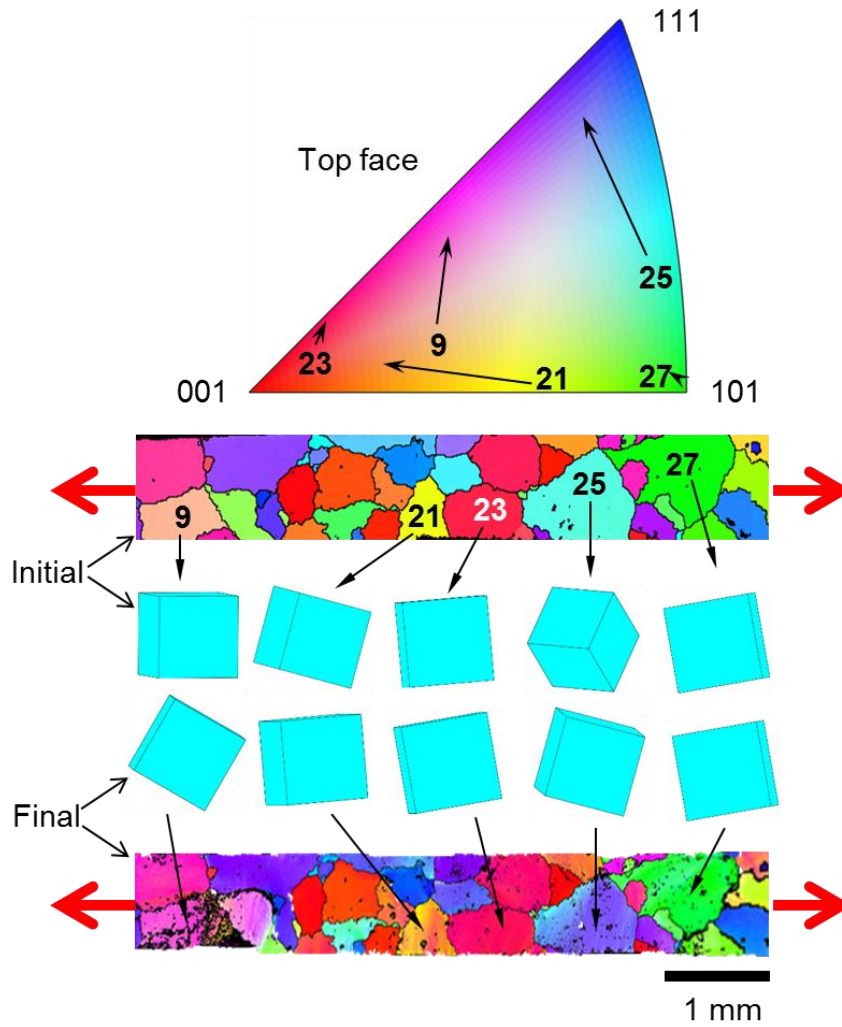


Figure 4.18 – Reorientation of several soft and hard grains during the experiment, in terms of change of corresponding IPF (RD) colors and of crystal lattice unit cell rotation (presented as cubes).

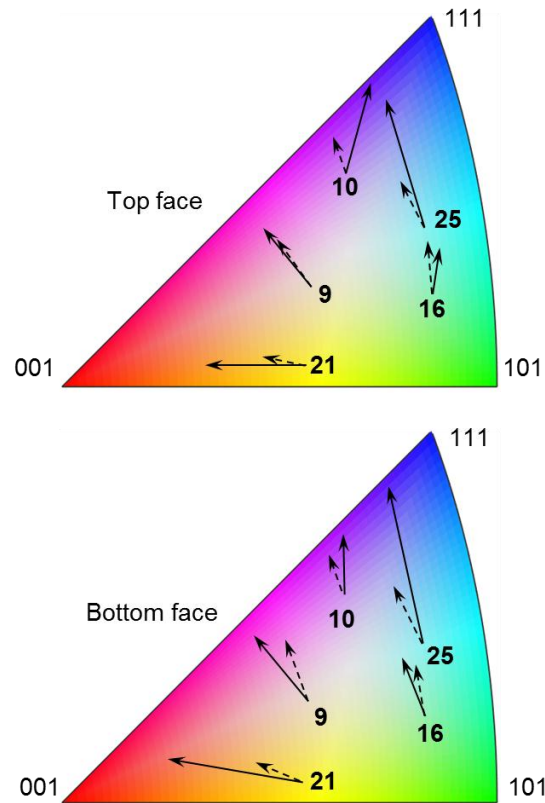


Figure 4.19 – Reorientation of 5 of the softest grains in the oligocrystal specimen, in terms of change of corresponding IPF (RD) colors. Solid arrows represent experimental observations, dashed arrows represent model predictions.

It was also possible to predict the Schmid factor fields (Fig. 4.20). It can be noticed that many distinct grains initially form unions that have very similar values of Schmid factor. These unions separate fully/partially as each individual grain is reorienting in its unique way. The grain boundaries within these unions become visible eventually. It can also be seen that initially soft grains that correspond to high initial values of Schmid factor (i.e., closer to red) become harder (i.e., orange/green) as deformation progresses. This fact is in accordance with previous observations of grain reorientations (Figs. 4.18, 4.19).

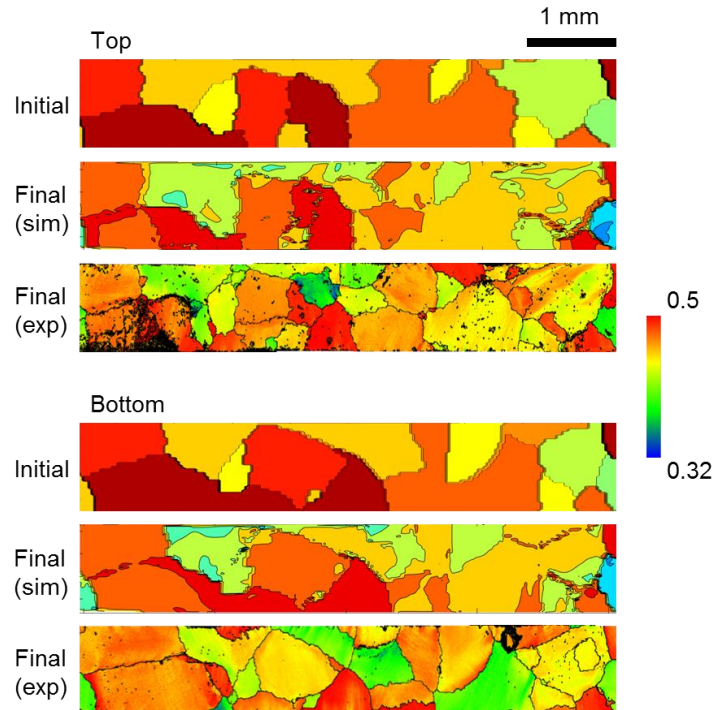


Figure 4.20 – Initial and final (at 10% nominal strain) distributions of Schmid factor at the top and bottom faces of the specimen, extracted from simulation (marked as “sim”) and experiment (marked as “exp”).

It is interesting to observe that the majority of the grains that have similar initial orientations (similar initial EBSD colors) reoriented in the same way. This implies that their reorientation was not affected much by the fact that each of them had quite different arrangements of neighboring grains. One possible explanation to this is that grains in our oligocrystal specimen are more planar than volumetric (since they form a single layer), which means they have more free surface area and therefore they are less restricted by the deformation of neighboring grains.

We can also observe that the CPFÉ model is able to capture the fact that orientations are varying within the grains (visible as change in color shades within corresponding grains, e.g., see [Figs. 4.16 and 4.17](#)), which is also seen in EBSD images.

4.5. Analysis of roughness statistics

a. Modeling surface roughening in a polycrystal

In order to further verify the CPFEM model, we analyze its performance for a case of polycrystal AA5052-O. In addition, the polycrystal study reveals statistical patterns that are hard or impossible to conclude from oligocrystal results. A tensile specimen of the same geometry as Fig. 4.4 is analyzed, but with no heat-treatment applied, i.e., in the as-received, polycrystalline state (the pole figures of corresponding texture are shown in Fig. A1). To assist with data extraction, 19 sets of indentation marks were applied to one of the faces of the specimen (Fig. 4.21). These marks provide a useful reference as they appear both in texture and surface elevation scans (after 10% macroscopic prestrain), see Fig. 4.21. Data from 10 of the 19 areas marked with indentations is shown in Fig. 4.22.

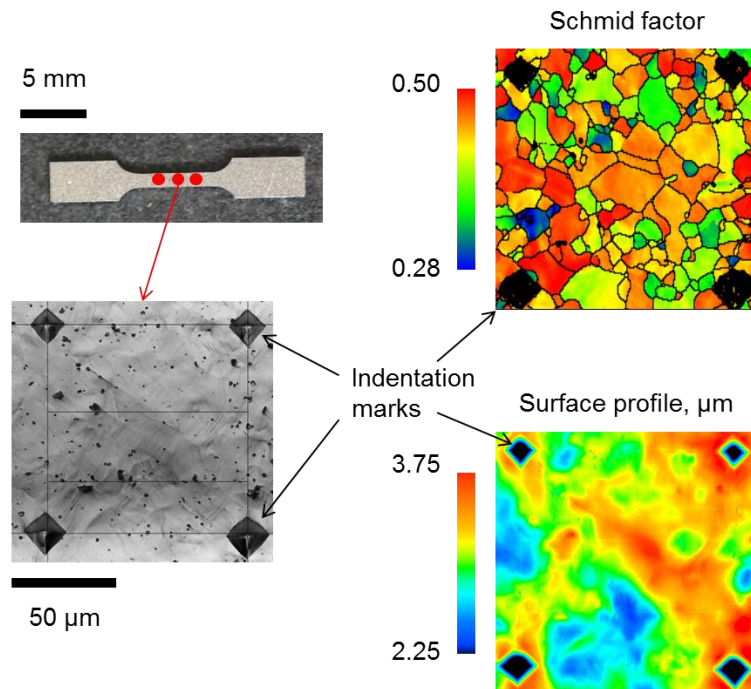


Figure 4.21 – One of the indentation areas from the surface of polycrystal along with Schmid factor and surface elevation data extracted from the same area.

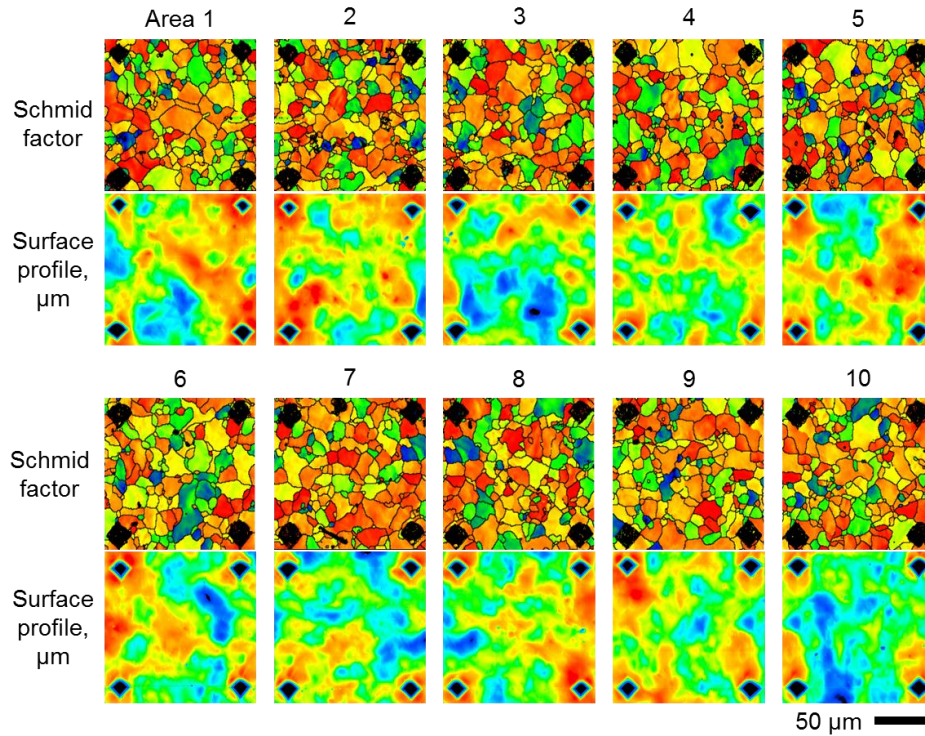


Figure 4.22 – Schmid factor and surface elevation data from 10 (out of 19) marked areas at the surface of polycrystalline specimen.

In order to model the roughening behavior of this polycrystalline specimen, two representative volume elements (RVE) are constructed using the DREAM.3D package, a digital representation environment for the analysis of 3D microstructures (Groeber and Jackson 2014). The RVE models are created using Abaqus/Standard. Each RVE contains $35 \times 35 \times 35 \approx 43,000$ finite elements. The element type is linear with full integration (C3D8). Each RVE has the same initial texture as the polycrystal (Fig. A1). Boundary conditions for both RVEs were the same and are shown in Fig. 4.23. The crystal-plasticity model described above is used in the simulation in form of a UMAT. By loading the two RVEs in tension, the roughness metric S_α is extracted from the 8 lateral sides (4 from each one). At the same time, S_α is calculated for each of the 19 areas of the tensile specimen. In order to make a fair comparison between CPFE results and

experiment, the initial roughness value of the specimen, S_0 , is subtracted. Also, the result is divided by the average grain size d_g , since the roughness is known to be linearly proportional to d_g . The value of $d_g = 10.3 \mu m$ was calculated using the ASTM standard E112-13 (ASTM 2013). Normalized values of surface roughness $(S_a - S_0)/d_g$ from experimental data (19 marked areas) and two RVEs (8 lateral sides) at 10% strain are shown in Figs. 4.24a and b, respectively. As could be expected, there is quite a bit of variation between different regions since each one contains relatively limited number of grains. Nevertheless, average values match well, which is seen in Fig. 4.24c.

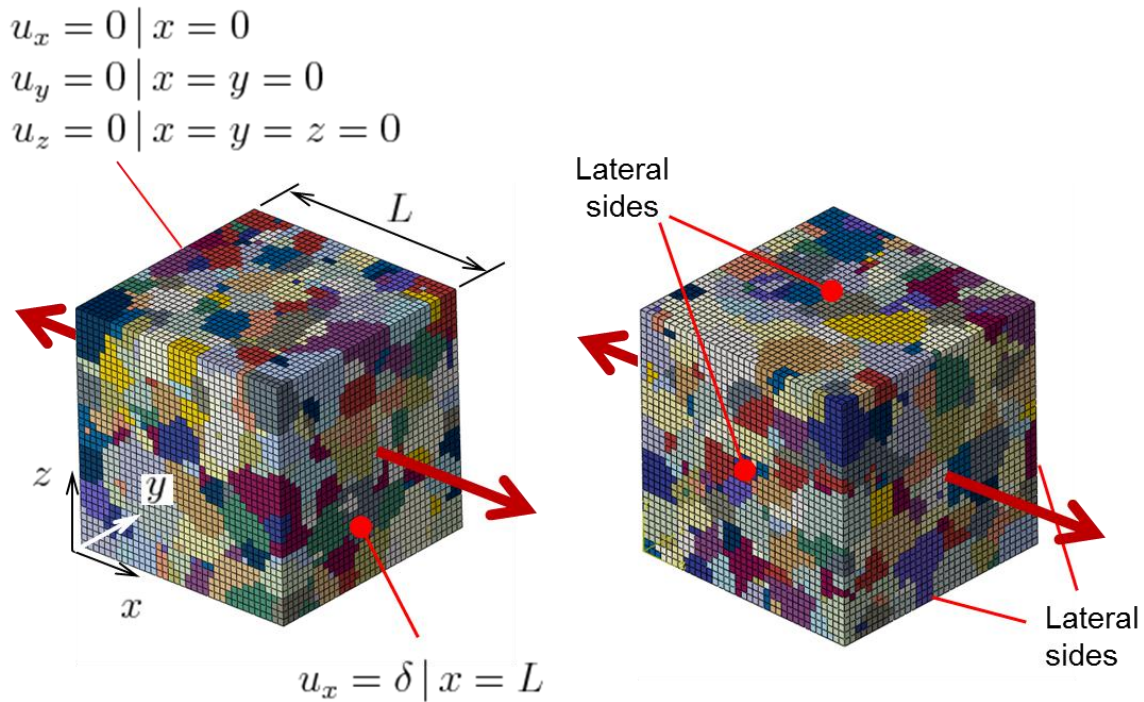


Figure 4.23 – Finite element meshes and boundary conditions (L is the side of the cube) for two representative volume elements (RVEs) that were used to model the roughening behavior of a polycrystal.

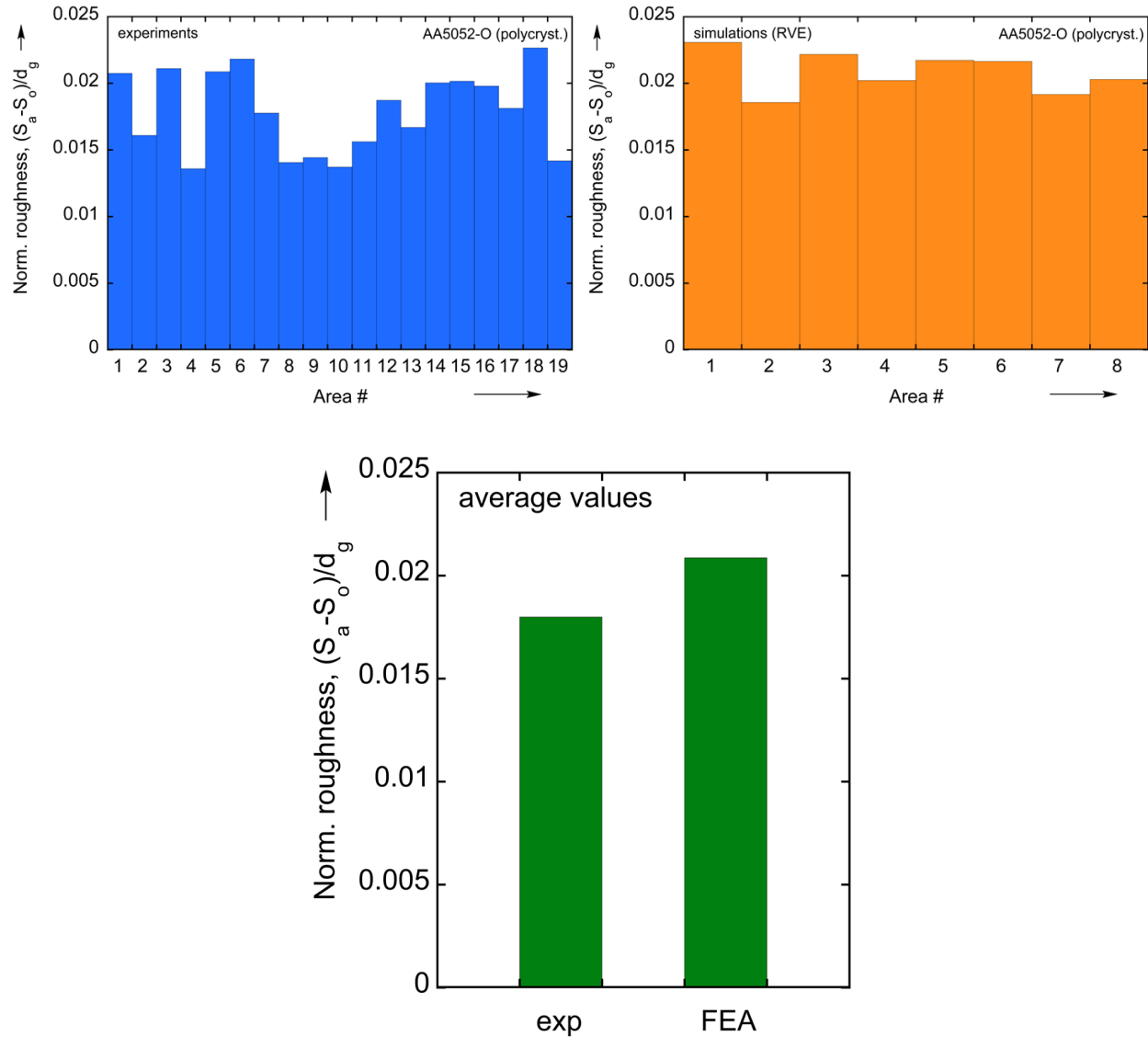


Figure 4.24 – A comparison between experiment and model for a polycrystal: raw values of normalized roughness parameters extracted from corresponding regions in experiment (19 areas) and model (8 areas). Average values are shown as well.

b. Texture-morphology relations

Since we have access to a considerable amount of data that can be extracted from the 19 areas of the polycrystalline specimen, we attempt here to find some mathematical relation between the texture and surface morphology. It is important that indentation marks appear both on EBSD scans and surface topography maps (Fig. 4.22), which

ensures a correspondence between texture and surface elevation before and after deformation. From each individual grain we extract several non-dimensional data sets:

1. Ratio of average elevation within the grain ($\delta = \frac{1}{A_i} \int_{A_i} z dA$, where A_i is the area of the given grain) to the average surface roughness of the specimen (S_A , see Eq. (4.14)):

$$\eta = \frac{\delta}{S_A}. \quad (4.16)$$

2. Ratio of average roughness within the grain ($S_i = \frac{1}{A_i} \int_{A_i} |z - \bar{z}| dA$) to the average surface roughness of the specimen (S_A):

$$\rho = \frac{S_i}{S_A}. \quad (4.17)$$

3. Average Schmid factor of the grain (SF) with respect to the loading axis.
4. Relative grain size:

$$\gamma = \frac{r}{\bar{r}^2} \quad (4.18)$$

where r is an effective radius of the given grain $r = \sqrt{A_i/\pi}$ and \bar{r} is the average effective radius among all grains.

It is also important to consider the effect of the surrounding grains. Assuming that the surrounding grains that are located along the loading axis have the greatest effect on the deformation of a given grain, we construct around each grain a circular or elliptical neighborhood, from which we extract η_n , ρ_n and SF_n correspondingly. Note that the quantities with the subscript n are for neighbors while the quantities with no subscript are for a given grain. One chosen grain and its neighborhood are shown in

Fig. 4.25. As a result, from each individual grain (about 1300 grains total) we obtain 7 parameters $(\rho, \rho_n, \eta, \eta_n, SF, SF_n, \gamma)$. Our goal is to find some relation between these parameters in the form:

$$\eta = f(\rho, \rho_n, \eta_n, SF, SF_n, \gamma), \quad (4.19)$$

where f is an unknown function. In order to find f we perform a symbolic Monte Carlo search by generating a very large number of random symbolic expressions and then pick the ones that show the best fit. We perform the search with the following parameters: unary operations $x^2, \sqrt{|x|}, \ln|x|, \exp(x)$; binary operations $+, -, \times, \div$; constants 2 and 3; maximum number of math operations per expression 10. The total number of unique generated random relations is around 7 million.

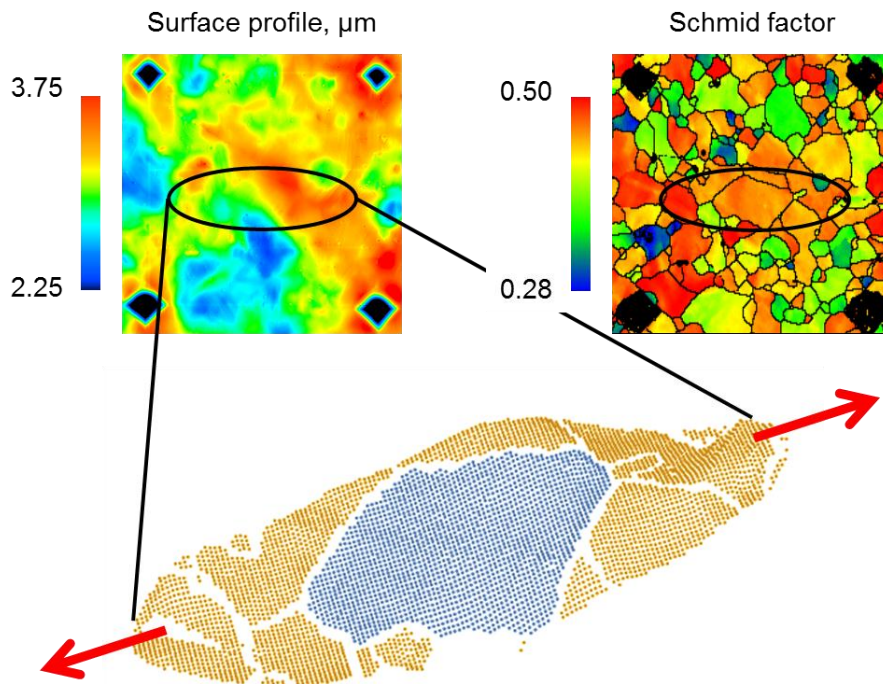


Figure 4.25 – Surface topography and Schmid factor data, extracted from a grain and its elliptical neighborhood. Similar data is extracted from each surface grain of the polycrystalline specimen (e.g., Figs. 4.21 and 4.22).

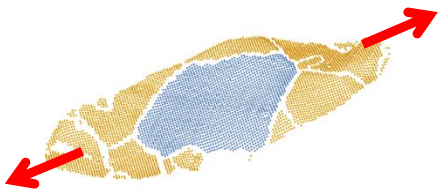
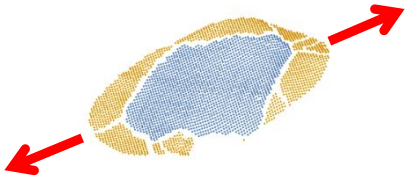
Several different shapes of neighborhood are investigated and are shown along with the corresponding identified relations in [Table 4.4](#). The strongest correlation is obtained for neighborhoods that are elongated and aligned with the loading axis, specifically for an elliptical neighborhood with semi-axes $3r$ and r (as well as $2r$ and r). A comparison between correlations obtained using elliptical and circular shapes of the neighborhood is shown in [Fig. 4.26](#). The elliptical neighborhood is seen to offer a better correlation than the circular one. The texture-morphology relation obtained for elongated neighborhoods has the following form:


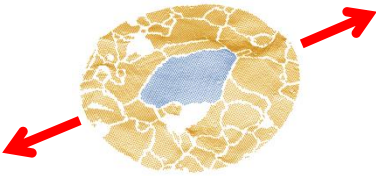
$$(\eta - \eta_n) \propto (SF_n - SF) \quad (4.20)$$

or, in a form similar to [Eq. \(4.19\)](#):

$$\eta = \eta_n + SF_n - SF. \quad (4.20a)$$

Table 4.4 – Relations constructed for different shapes of the neighborhood.

Shape	Semi-axes	Relation
	$(3r, r)$	$\eta = \eta_n + SF_n - SF$
	$(2r, r)$	$\eta = \eta_n + SF_n - SF$

	$(2r, 2r)$	$\eta = \eta_n + \frac{SF_n - SF}{2}$
	$(3r, 3r)$	$\eta = \eta_n + \frac{SF_n - SF}{3}$

Since the Schmid factor characterizes the softness or hardness of a given grain, the physical meaning of this relation can be understood as follows: the difference between the elevation of a given grain and its neighborhood is proportional to the difference between their corresponding Schmid factors. In other words, if a grain and its surrounding are equally soft or equally hard, a large change in elevation should not be expected. In contrast, a hard grain embedded into a soft neighborhood (as well as a soft grain embedded into a hard neighborhood) causes change in elevation. Also, as can be seen from the scatter in [Fig. 4.26](#), the obtained relations are not applicable to individual grains, but instead capture the overall trend. In comparison to current understanding of surface roughening, this section statistically identifies a specific mathematical relation between non-dimensionalized texture and morphology parameters, after checking a very large amount of candidate relations. Similar analysis has been performed into the effect of properties of neighboring grains on intra-granular misorientation development in a given grain with plastic strain ([Knezevic et al. 2014](#)). It was found that smaller intra-granular misorientation levels are associated ‘softer’ neighborhoods and vice versa.

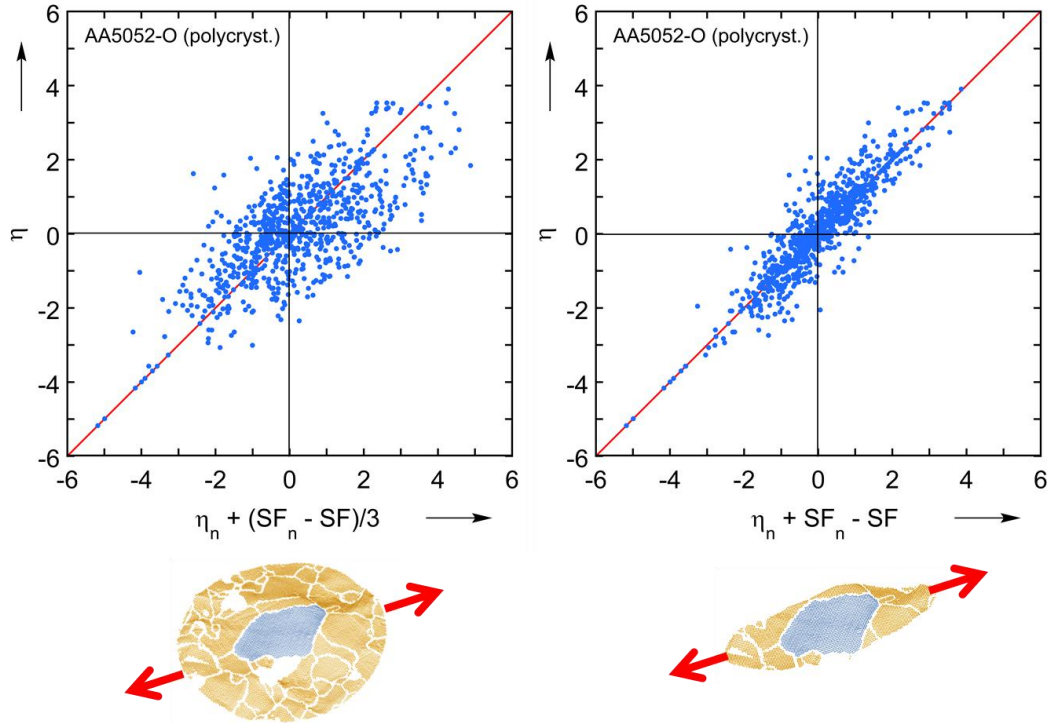


Figure 4.26 – Correlations shown for circular (radius $3r$) and elliptical (semi-axes $3r$ and r) neighborhoods. Red solid line corresponds to perfect correlation; blue dots are actual observations. The elliptical neighborhood offers better correlation (variance = 0.16) than the circular one (variance = 0.49).

4.6. Summary and conclusions

In this work we studied the deformation-induced surface roughening of an Al-Mg oligocrystal (produced from polycrystalline AA5052-O) by examining the roughening behavior of a mesoscale-size specimen that contains relatively few grains, most of them arranged in a single layer. The specimen was deformed plastically under (macroscopically) uniaxial tension. The initial and final textures of the specimen, as well as surface topographies at the top and bottom faces were measured. The physics of plastic deformation was captured with an appropriate CPFEE model. Four unknown material parameters were determined inversely using an efficient black-box optimization procedure. Differently from other numerical studies on deformation-induced surface

roughening, the FE model created in this work had realistic (non-columnar) shapes of the grains. These shapes were reconstructed from EBSD scans of top and bottom faces using a custom-developed shape interpolation procedure that is based on a morphing approach. Using this FE model, we were able to analyze a number of aspects such as deformed shape of the specimen, surface topographies at top and bottom faces, corresponding elevation derivatives, evolution of the average roughness value, texture and Schmid factor after deformation, and reorientation of several soft and hard grains. The results extracted from the model match well with experimental observations, however exact surface topographies were not predicted well.

In order to further verify the CPFEM model, we also analyzed statistical aspects of surface roughening by simulating the behavior of a polycrystal. A tension test was performed on a polycrystalline AA5052-O specimen. Two representative volume elements (each containing around 1500 grains) of corresponding initial texture were constructed and their deformation was simulated. A good match between average roughness values from the model and from the experiment was observed. The polycrystal specimen contained a number of indentation marks on its surface, so that it was possible to establish the correspondence between grain texture and morphology at these marked regions. Subsequently, using an automated method based on a symbolic Monte Carlo approach we were able to identify relations between the problem variables.

After analyzing the behavior of oligocrystal, several conclusions can be made. The CPFEM model is overall capable of capturing the deformation-induced roughening behavior of this material. This is certainly true in an average sense, but also in a local sense, with the exception of only few regions of the specimen. Some limited corrugation

of the specimen – bending of mid-plane with thickness remaining relatively constant – was observed and also captured by our model. In addition, peaks and valleys of surface topography were observed primarily at the grain boundaries, which is due to the fact that grain boundaries act as kinematic constraints and therefore extreme values of mechanical fields such as out-of-plane displacement also appear there. Finally, grain reorientations seem to depend mostly on initial orientations of these grains, and not on arrangement/orientations of their neighbors, owing to the pancake-like shapes of grains in our oligocrystal which are not very restrictive kinematically.

From the polycrystal analysis we can conclude that a model with proper statistical input such as initial texture and average grain size is enough to capture the roughening behavior with good accuracy. In addition, it was shown that simple relations between Schmid factor and non-dimensional surface elevation for individual grains and their neighbors can be inferred purely from experimental data and also can be easily explained from physical point of view. Future work will advance the CPFEE model into a strain gradient plasticity (SG-CPFEE) formulation ([Gurtin and Anand 2009](#)) to evaluate whether the SG-CPFEE model will improve the predictions of roughness fields.

CHAPTER 5

SUMMARY AND FUTURE WORK

This thesis consists of 3 main chapters that cover the following topics:

- Post-necking hardening identification in metals ([Chapter 2](#))
- Accurate reconstruction of 3D textures based on a set of 2D textures ([Chapter 3](#))
- Study of deformation-induced surface roughening using advanced crystal plasticity model ([Chapter 4](#))

All chapters cover both phenomenological and physical approaches to modeling metal deformation processes and are strongly connected to each other. For example, [Chapter 2](#), while focused on post necking identification that accounts for rate and temperature effects using simple J_2 model, describes an efficient black-box optimization algorithm that can be used for solving virtually any inverse problem. Subsequently the same algorithm finds its application in [Chapter 4](#) for identification of unknown material constants of an advanced CPFE model. Similarly, the shape interpolation algorithm developed in [Chapter 3](#) is very general and is shown to work for 3D reconstruction from any number of given 2D sections. This approach as well found its application in [Chapter 4](#) for producing a realistic model of the given sample based only on a pair of scans. More specific findings of each chapter are discussed below.

In [Chapter 2](#) an approach to identify post-necking hardening curves with decoupled rate and temperature effects was proposed. Isothermal tension experiments were performed on SS-304L tubes using a custom setup. This material was selected because its response is very sensitive to both strain-rate and temperature. The problem was

tackled as an optimization task. An objective function was created using parameters that control the post-necking shape of the hardening curves as input, and a scalar value that represents the proximity between the predicted (FEA) and experimental structural responses as output. Because such a function is expensive to evaluate, an optimization procedure based on the response surface methodology was implemented in order to reach an optimum with limited number of function evaluations. The post-necking hardening curves were identified under different assumptions: without considering rate and temperature effects; by considering only the temperature effect; and by considering both rate and temperature effects. The latter case makes the most sense, physically.

The hardening curves identified were verified using fully-coupled thermomechanical FEA for modeling the conventional tension test. A proper value of the convection coefficient was found using the optimization procedure to match the experimental force-average axial strain curve. Using full-field measuring techniques (DIC and IR) it was possible to extract the strain and temperature fields along the specimen and compare them to the FE predictions. These predictions were found to be more accurate for the case of the fully-coupled curves in comparison to rate- and/or temperature-independent cases.

[Chapter 3](#) describes a method that allows the reconstruction of a 3D voxel model of a physical object from two images obtained from parallel sections of that object. The method is based on a morphing technique. The input to the method is a pair of images from given parallel sections; the output is a sequence of images that interpolate the two given images. The images produced can be stacked on top of each other in order to obtain a 3D voxel model. As shown in this work, the procedure works well for binary

images as well as for images that contain matching sets of colors.

The performance of the method is demonstrated for a simple artificial input. It is also shown how it can be applied to real grain structure scans in order to reconstruct the volumetric grain structure of a thin metallic specimen. It was possible to verify the accuracy of the texture reconstruction by looking into how well the prediction is matching the actual structure in the bulk of the specimen. Finally, the feasibility of reconstruction from multiple sections using a dual-phase, martensite-ferrite representative volume element was demonstrated.

[Chapter 4](#) covers the deformation-induced surface roughening of an Al-Mg oligocrystal (produced from polycrystalline AA5052-O) by examining the roughening behavior of a mesoscale-size specimen that contains relatively few grains, most of them arranged in a single layer. The specimen was deformed plastically under (macroscopically) uniaxial tension. The initial and final textures of the specimen, as well as surface topographies at the top and bottom faces were measured. The physics of plastic deformation was captured with an appropriate CPFEM model. Four unknown material parameters were determined inversely using the efficient black-box optimization procedure described in [Chapter 2](#). Differently from many other numerical studies on deformation-induced surface roughening, the FE model created in this work had realistic (non-columnar) shapes of the grains. These shapes were reconstructed from EBSD scans of top and bottom faces using a custom-developed shape interpolation procedure that is based on a morphing approach. Using this FE model, it was possible to analyze a number of aspects such as deformed shape of the specimen, surface topographies at top and bottom faces, corresponding elevation derivatives,

evolution of the average roughness value, texture and Schmid factor after deformation, and reorientation of several soft and hard grains. The results extracted from the model match well with experimental observations, however exact surface topographies were not predicted well.

In order to further verify the CPFEM model, statistical aspects of surface roughening were analyzed by simulating the behavior of a polycrystal. A tension test was performed on a polycrystalline AA5052-O specimen. Two representative volume elements (each containing around 1500 grains) of corresponding initial texture were constructed and their deformation was simulated. A good match between average roughness values from the model and from the experiment was observed. The polycrystal specimen contained a number of indentation marks on its surface, so that it was possible to establish the correspondence between grain texture and morphology at these marked regions. Subsequently, using an automated method based on a symbolic Monte Carlo approach it was possible to identify relations between the problem variables.

From the polycrystal analysis it can be concluded that a model with proper statistical input such as initial texture and average grain size is enough to capture the roughening behavior with good accuracy. In addition, it was shown that simple relations between Schmid factor and non-dimensional surface elevation for individual grains and their neighbors can be inferred purely from experimental data and also can be easily explained from physical point of view.

In summary, this thesis covers both phenomenological and physical approaches to modeling the deformation of metals. Novel methods of solving several fundamental problems were proposed. One such problem is an accurate hardening identification that

accounts for rate and temperature sensitivity of the material. Another problem is the comprehensive analysis of the deformation-induced surface roughening at the grain scale. Few general computational tools were developed – efficient black-box optimization procedure, shape interpolation procedure and symbolic model generation procedure. These tools allowed to solve given problems successfully and efficiently. The obtained results as well as developed approaches and methodologies can be applied in wide range of engineering problems.

As for the future work, [Chapter 2](#) describes a complete and working methodology. It should be noted that the methodology can be applied to other mathematical forms of the hardening curve at large strains (e.g., Stage III and IV of hardening). One thing that could be done differently (fundamentally) is using more advanced plasticity model (instead of J_2), such as Yld2000-2D ([Barlat *et al.*, 2003](#)) or Yld2004-3D ([Barlat *et al.*, 2005](#)), which would account for plastic anisotropy in the material. However, this would also significantly complicate the study from both calibration and optimization points of view (much higher number of parameters).

The main downside of the reconstruction procedure ([Chapter 3](#)) – inability to interpolate between shapes that have no overlap – needs to be addressed in the future. For example, for non-overlapping shapes, a fictitious shape mid-way between them could be introduced, to allow the procedure to be applied. This was not an issue in the present study, because the sections of interest were close to each other and did overlap. However, the procedure will definitely fail for more complicated cases, such as elongated and inclined grains.

As for [Chapter 4](#), the cause of poor prediction of surface elevation should be

identified in the future. This is not an easy task, as the procedure involves elaborate preparation–scanning–testing cycle. As was mentioned earlier, the fact that many grains did not go all the way through the thickness, as well as possible experimental measurement issues are the most likely reasons for disagreement. It would be also useful to see if the model is able to capture deformation of a single grain (or an assembly of 2-3 grains) accurately, which would be a much needed validation. Also, strain gradient crystal plasticity formulation would help to improve the predictions. In addition, the usage of cohesive zone elements could potentially help modeling physics of grain boundaries more accurately. Once all this is verified, the study of roughening in biaxial state of stress can be performed.

REFERENCES

- Aboav, D.A., 1970. The arrangement of grains in a polycrystal. *Metallography*, 3(4), pp.383-390.
- Ardeljan, M., Beyerlein, I.J. and Knezevic, M., 2014. A dislocation density based crystal plasticity finite element model: application to a two-phase polycrystalline HCP/BCC composites. *Journal of the Mechanics and Physics of Solids*, 66, pp.16-31.
- Ardeljan, M., Beyerlein, I.J. and Knezevic, M., 2017. Effect of dislocation density-twin interactions on twin growth in AZ31 as revealed by explicit crystal plasticity finite element modeling. *International Journal of Plasticity*, 99, pp.81-101.
- Ardeljan, M., Knezevic, M., Nizolek, T., Beyerlein, I.J., Mara, N.A. and Pollock, T.M., 2015. A study of microstructure-driven strain localizations in two-phase polycrystalline HCP/BCC composites using a multi-scale model. *International Journal of Plasticity*, 74, pp.35-57.
- Aronofsky, J., 1951. Evaluation of stress distribution in the symmetrical neck of flat tensile bars. *Journal of Applied Mechanics-Trans. ASME*, 18(1), pp.75-84.
- ASM International Handbook Committee, 1990. Metals Handbook: Vol. 2, Properties and selection—nonferrous alloys and pure metals.
- ASTM International, 2013. ASTM E112-13-Standard Test Methods for Determining Average Grain Size.
- Bajaj, C.L., Coyle, E.J. and Lin, K.N., 1996. Arbitrary topology shape reconstruction from planar cross sections. *Graphical models and image processing*, 58(6), pp.524-543.
- Banovic, S.W. and Foecke, T., 2003. Evolution of strain-induced microstructure and texture in commercial aluminum sheet under balanced biaxial stretching. *Metallurgical and Materials Transactions A*, 34(3), p.657.
- Barlat, F., Aretz, H., Yoon, J.W., Karabin, M.E., Brem, J.C. and Dick, R.E., 2005. Linear transformation-based anisotropic yield functions. *International Journal of Plasticity*, 21(5), pp.1009-1039.
- Barlat, F., Brem, J.C., Yoon, J.W., Chung, K., Dick, R.E., Lege, D.J., Pourboghrat, F., Choi, S.H. and Chu, E., 2003. Plane stress yield function for aluminum alloy sheets—part 1: theory. *International Journal of Plasticity*, 19(9), pp.1297-1319.
- Barrett, T.J., Savage, D.J., Ardeljan, M. and Knezevic, M., 2018. An automated procedure for geometry creation and finite element mesh generation: Application to explicit grain structure models and machining distortion. *Computational Materials*

Science, 141, pp.269-281.

Baudoin, P. and Hama, T., 2018. Private communication.

Baudoin, P., Hama, T. and Takuda, H., 2018. Influence of critical resolved shear stress ratios on the response of a commercially pure titanium oligocrystal: crystal plasticity simulations and experiment. *International Journal of Plasticity*.

Baydogan, M., MA, A. and Cimenoglu, H., 2003. Deformation induced surface roughening of austenitic stainless steels. *ISIJ international*, 43(11), pp.1795-1798.

Beaudoin, A.J., Bryant, J.D. and Korzekwa, D.A., 1998. Analysis of ridging in aluminum auto body sheet metal. *Metallurgical and Materials Transactions A*, 29(9), pp.2323-2332.

Becker, R., 1998. Effects of strain localization on surface roughening during sheet forming. *Acta Materialia*, 46(4), pp.1385-1401.

Boissonnat, J.D., 1988. Shape reconstruction from planar cross sections. *Computer vision, graphics, and image processing*, 44(1), pp.1-29.

Boots, B.N., 1982. The arrangement of cells in “random” networks. *Metallography*, 15(1), pp.53-62.

Bors, A.G., Kechagias, L. and Pitas, I., 2002. Binary morphological shape-based interpolation applied to 3-D tooth reconstruction. *IEEE transactions on medical imaging*, 21(2), pp.100-108.

Box, G.E. and Wilson, K.B., 1951. On the experimental attainment of optimum conditions. *Journal of the Royal Statistical Society. Series B (Methodological)*, 13(1), pp.1-45.

Bridgman, P.W., 1952. *Studies in large plastic flow and fracture* (Vol. 177). New York: McGraw-Hill.

Calcagnotto, M., Ponge, D., Demir, E. and Raabe, D., 2010. Orientation gradients and geometrically necessary dislocations in ultrafine grained dual-phase steels studied by 2D and 3D EBSD. *Materials Science and Engineering: A*, 527(10-11), pp.2738-2746.

Chen, K., Scales, M., Kyriakides, S. and Corona, E., 2016. Effects of anisotropy on material hardening and burst in the bulge test. *International Journal of Solids and Structures*, 82, pp. 70–84.

Chen, S.Y., Lin, W.C., Liang, C.C. and Chen, C.T., 1990. Improvement on dynamic elastic interpolation technique for reconstructing 3-D objects from serial cross sections (biomedical application). *IEEE Transactions on Medical Imaging*, 9(1), pp.71-83.

- Chen, W.H., 1971. Necking of a bar. *International Journal of Solids and Structures*, 7(7), pp.685-717.
- Coppieters, S. and Kuwabara, T., 2014. Identification of post-necking hardening phenomena in ductile sheet metal. *Experimental Mechanics*, 54(8), pp.1355-1371.
- Coppieters, S., Cooreman, S., Sol, H., Van Houtte, P. and Debruyne, D., 2011. Identification of the post-necking hardening behaviour of sheet metal by comparison of the internal and external work in the necking zone. *Journal of Materials Processing Technology*, 211(3), pp.545-552.
- Coppieters, S., Lava, P., Sol, H., Van Bael, A., Van Houtte, P. and Debruyne, D., 2010. Determination of the flow stress and contact friction of sheet metal in a multi-layered upsetting test. *Journal of Materials Processing Technology*, 210(10), pp.1290-1296.
- Cordero, R.R., François, M., Lira, I. and Vial-Edwards, C., 2005. Whole-field analysis of uniaxial tensile tests by Moiré interferometry. *Optics and Lasers in Engineering*, 43(9), pp.919-936.
- Cullen, G.W. and Korkolis, Y.P., 2013. Ductility of 304 stainless steel under pulsed uniaxial loading. *International Journal of Solids and Structures*, 50(10), pp.1621-1633.
- De Almeida, L.H., Le May, I. and Monteiro, S.N., 1984. On cell structure and subgrain formation in type 304 stainless steel. *Metallography*, 17(4), pp.349-357.
- De Berg, M., Van Kreveld, M., Overmars, M. and Schwarzkopf, O.C., 2000. Computational geometry. In *Computational geometry* (pp. 1-17). Springer, Berlin, Heidelberg.
- Diard, O., Leclercq, S., Rousselier, G. and Cailletaud, G., 2005. Evaluation of finite element based analysis of 3D multicrystalline aggregates plasticity: Application to crystal plasticity model identification and the study of stress and strain fields near grain boundaries. *International Journal of Plasticity*, 21(4), pp.691-722.
- Dick, C.P. and Korkolis, Y.P., 2014. Mechanics and full-field deformation study of the ring hoop tension test. *International Journal of Solids and Structures*, 51(18), pp.3042-3057.
- Dick, C.P. and Korkolis, Y.P., 2015. Strength and ductility evaluation of cold-welded seams in aluminum tubes extruded through porthole dies. *Materials & Design*, 67, pp.631-636.
- Fullwood, D.T., Niezgoda, S.R. and Kalidindi, S.R., 2008. Microstructure reconstructions from 2-point statistics using phase-recovery algorithms. *Acta Materialia*, 56(5), pp.942-948.
- Furushima, T., Tsunozaki, H., Manabe, K.I. and Alexandrov, S., 2014. Ductile fracture

- and free surface roughening behaviors of pure copper foils for micro/meso-scale forming. *International Journal of Machine Tools and Manufacture*, 76, pp.34-48.
- Ghosh, A.K., 1977. Tensile instability and necking in materials with strain hardening and strain-rate hardening. *Acta Metallurgica*, 25(12), pp.1413-1424.
- Goshtasby, A., Turner, D.A. and Ackerman, L.V., 1992. Matching of tomographic slices for interpolation. *IEEE Transactions on Medical Imaging*, 11(4), pp.507-516.
- Groeber, M.A. and Jackson, M.A., 2014. DREAM. 3D: a digital representation environment for the analysis of microstructure in 3D. *Integrating Materials and Manufacturing Innovation*, 3(1), p.5.
- Gross, A.J. and Ravi-Chandar, K., 2015. On the extraction of elastic–plastic constitutive properties from three-dimensional deformation measurements. *Journal of Applied Mechanics – Trans. ASME*, 82(7), p.071013.
- Guan, Y., Chen, B., Zou, J., Britton, T.B., Jiang, J. and Dunne, F.P., 2017. Crystal plasticity modelling and HR-DIC measurement of slip activation and strain localization in single and oligo-crystal Ni alloys under fatigue. *International Journal of Plasticity*, 88, pp.70-88.
- Guangnan, C., Huan, S., Shiguang, H. and Baudelet, B., 1990. Roughening of the free surfaces of metallic sheets during stretch forming. *Materials Science and Engineering: A*, 128(1), pp.33-38.
- Guery, A., Hild, F., Latourte, F. and Roux, S., 2016. Identification of crystal plasticity parameters using DIC measurements and weighted FEMU. *Mechanics of Materials*, 100, pp.55-71.
- Guery, A., Hild, F., Latourte, F. and Roux, S., 2016. Slip activities in polycrystals determined by coupling DIC measurements with crystal plasticity calculations. *International Journal of Plasticity*, 81, pp.249-266.
- Gurtin, M.E. and Anand, L., 2009. Thermodynamics applied to gradient theories involving the accumulated plastic strain: the theories of Aifantis and Fleck and Hutchinson and their generalization. *Journal of the Mechanics and Physics of Solids*, 57(3), pp.405-421.
- Ha, J., Lee, J., Kim, J.H., Lee, M.G. and Barlat, F., 2017. Investigation of plastic strain rate under strain path changes in dual-phase steel using microstructure-based modeling. *International Journal of Plasticity*, 93, pp.89-111.
- Hall, E.O., 1951. The deformation and ageing of mild steel: III discussion of results. *Proceedings of the Physical Society. Section B*, 64(9), p.747.
- Higgins, W.E., Orlick, C.J. and Ledell, B.E., 1996. Nonlinear filtering approach to 3-D gray-scale image interpolation. *IEEE transactions on medical imaging*, 15(4),

pp.580-587.

Hill, R., 1952. On discontinuous plastic states, with special reference to localized necking in thin sheets. *Journal of the Mechanics and Physics of Solids*, 1(1), pp.19-30.

Holmström, K., 2008. An adaptive radial basis algorithm (ARBF) for expensive black-box global optimization. *Journal of Global Optimization*, 41(3), pp.447-464.

Hosford, W.F., 2010. *Mechanical behavior of materials*. Cambridge university press.

Humphreys, F.J., 2004. Characterisation of fine-scale microstructures by electron backscatter diffraction (EBSD). *Scripta materialia*, 51(8), pp.771-776.

Inkson, B.J., Mulvihill, M. and Möbus, G., 2001. 3D determination of grain shape in a FeAl-based nanocomposite by 3D FIB tomography. *Scripta Materialia*, 45(7), pp.753-758.

Johnson, G., King, A., Honnicke, M.G., Marrow, J. and Ludwig, W., 2008. X-ray diffraction contrast tomography: a novel technique for three-dimensional grain mapping of polycrystals. II. The combined case. *Journal of Applied Crystallography*, 41(2), pp.310-318.

Johnson, G.R. and Cook, W.H., 1983. A constitutive model and data for metals subjected to large strains, high strain rates and high temperatures. In *Proceedings of the 7th International Symposium on Ballistics* (Vol. 21, pp. 541-547).

Joliot, M. and Mazoyer, B.M., 1993. Three-dimensional segmentation and interpolation of magnetic resonance brain images. *IEEE Transactions on Medical Imaging*, 12(2), pp.269-277.

Joun, M., Eom, J.G. and Lee, M.C., 2008. A new method for acquiring true stress–strain curves over a large range of strains using a tensile test and finite element method. *Mechanics of Materials*, 40(7), pp.586-593.

Kajberg, J. and Lindkvist, G., 2004. Characterisation of materials subjected to large strains by inverse modelling based on in-plane displacement fields. *International Journal of Solids and Structures*, 41(13), pp.3439-3459.

Kalidindi, S.R., Bronkhorst, C.A. and Anand, L., 1992. Crystallographic texture evolution in bulk deformation processing of FCC metals. *Journal of the Mechanics and Physics of Solids*, 40(3), pp.537-569.

Kamaya, M. and Kawakubo, M., 2014. True stress–strain curves of cold worked stainless steel over a large range of strains. *Journal of Nuclear Materials*, 451(1), pp.264-275.

KEYENCE VK-X100 Specifications (accessed on www.keyence.com on Aug 8, 2019)

- Khorashadizadeh, A., Raabe, D., Zaeferrer, S., Rohrer, G.S., Rollett, A.D. and Winning, M., 2011. Five-Parameter Grain Boundary Analysis by 3D EBSD of an Ultra Fine Grained CuZr Alloy Processed by Equal Channel Angular Pressing. *Advanced Engineering Materials*, 13(4), pp.237-244.
- Kim, J.H., Serpantié, A., Barlat, F., Pierron, F. and Lee, M.G., 2013. Characterization of the post-necking strain hardening behavior using the virtual fields method. *International Journal of Solids and Structures*, 50(24), pp.3829-3842.
- Knezevic, M., Drach, B., Ardeljan, M. and Beyerlein, I.J., 2014. Three dimensional predictions of grain scale plasticity and grain boundaries using crystal plasticity finite element models. *Computer Methods in Applied Mechanics and Engineering*, 277, pp.239-259.
- Knezevic, M., Zecevic, M., Beyerlein, I.J. and Lebensohn, R.A., 2016. A numerical procedure enabling accurate descriptions of strain rate-sensitive flow of polycrystals within crystal visco-plasticity theory. *Computer Methods in Applied Mechanics and Engineering*, 308, pp.468-482.
- Knysh, P. and Korkolis, Y., 2016. Blackbox: A procedure for parallel optimization of expensive black-box functions. *arXiv preprint arXiv:1605.00998*.
- Knysh, P. and Korkolis, Y.P., 2015. Determination of the fraction of plastic work converted into heat in metals. *Mechanics of Materials*, 86, pp.71-80.
- Knysh, P. and Korkolis, Y.P., 2015. Necking of pressurized tubes of 304L stainless steel under tension, *IUTAM Symposium: Ductile Fracture and Localization*, Paris, Mar. 17-20.
- Knysh, P. and Korkolis, Y.P., 2017. Identification of the post-necking hardening response of rate-and temperature-dependent metals. *International Journal of Solids and Structures*, 115, pp.149-160.
- Knysh, P., Sasaki, K., Furushima, T., Knezevic, M. and Korkolis, Y.P., 2018, Deformation-induced surface roughening of an Al-Mg alloy. *2018 NUMISHEET*, Tokyo, Japan, Jul 30-Aug 3
- Knysh, P., Sasaki, K., Furushima, T., Knezevic, M. and Korkolis, Y.P., 2019. A shape interpolation procedure: Application to creating explicit grain structure models based on partial data sets. (under review)
- Koc, P. and Štok, B., 2004. Computer-aided identification of the yield curve of a sheet metal after onset of necking. *Computational Materials Science*, 31(1), pp.155-168.
- Korkolis, Y.P. and Kyriakides, S., 2008a. Inflation and burst of anisotropic aluminum tubes for hydroforming applications. *International Journal of Plasticity*, 24(3), pp.509-543.

- Korkolis, Y.P. and Kyriakides, S., 2008b. Inflation and burst of aluminum tubes. Part II: An advanced yield function including deformation-induced anisotropy. *International Journal of Plasticity*, 24(9), pp.1625-1637.
- Korkolis, Y.P. and Kyriakides, S., 2009. Path-dependent failure of inflated aluminum tubes. *International Journal of Plasticity*, 25(11), pp.2059-2080.
- Korkolis, Y.P. and Kyriakides, S., 2011. Hydroforming of anisotropic aluminum tubes: Part II analysis. *International Journal of Mechanical Sciences*, 53(2), pp.83-90.
- Korkolis, Y.P., Kyriakides, S., Giagmouris, T. and Lee, L.H., 2010. Constitutive modeling and rupture predictions of Al-6061-T6 tubes under biaxial loading paths. *Journal of Applied Mechanics-Trans. ASME*, 77(6), p.064501.
- Kubo, M., Hama, T., Tsunemi, Y., Nakazawa, Y. and Takuda, H., 2018. Influence of Strain Ratio on Surface Roughening in Biaxial Stretching of IF Steel Sheets. *ISIJ International*, 58(4), pp.704-713.
- Kubo, M., Nakazawa, Y., Hama, T. and Takuda, H., 2017. Effect of Microstructure on Surface Roughening in Stretch Forming of Steel Sheets. *ISIJ International*, 57(12), pp.2185-2193.
- Lee, P.S., Piehler, H.R., Adams, B.L., Jarvis, G., Hampel, H. and Rollett, A.D., 1998. Influence of surface texture on orange peel in aluminum. *Journal of Materials Processing Technology*, 80, pp.315-319.
- Li, S.F., Lind, J., Hefferan, C.M., Pokharel, R., Lienert, U., Rollett, A.D. and Suter, R.M., 2012. Three-dimensional plastic response in polycrystalline copper via near-field high-energy X-ray diffraction microscopy. *Journal of Applied Crystallography*, 45(6), pp.1098-1108.
- Lim, H., Carroll, J.D., Battaile, C.C., Boyce, B.L. and Weinberger, C.R., 2015. Quantitative comparison between experimental measurements and CP-FEM predictions of plastic deformation in a tantalum oligocrystal. *International Journal of Mechanical Sciences*, 92, pp.98-108.
- Lim, H., Carroll, J.D., Battaile, C.C., Buchheit, T.E., Boyce, B.L. and Weinberger, C.R., 2014. Grain-scale experimental validation of crystal plasticity finite element simulations of tantalum oligocrystals. *International Journal of Plasticity*, 60, pp.1-18.
- Lin, M.R. and Wagoner, R.H., 1986. Effect of temperature, strain, and strain rate on the tensile flow stress of IF steel and stainless steel type 310. *Scripta Metallurgica*, 20(1), pp.143-148.
- Lind, J., Li, S.F., Pokharel, R., Lienert, U., Rollett, A.D. and Suter, R.M., 2014. Tensile twin nucleation events coupled to neighboring slip observed in three dimensions. *Acta Materialia*, 76, pp.213-220.

- Ling, Y., 1996. Uniaxial true stress-strain after necking. *AMP Journal of Technology*, 5, pp.37-48.
- Lo, S.W. and Horng, T.C., 1999. Surface roughening and contact behavior in forming of aluminum sheet. *Strain*, 6, pp.7-0.
- Lovato, M.L. and Stout, M.G., 1992. Compression testing techniques to determine the stress/strain behavior of metals subject to finite deformation. *Metallurgical Transactions A*, 23(3), pp.935-951.
- Ludwig, W., Schmidt, S., Lauridsen, E.M. and Poulsen, H.F., 2008. X-ray diffraction contrast tomography: a novel technique for three-dimensional grain mapping of polycrystals. I. Direct beam case. *Journal of Applied Crystallography*, 41(2), pp.302-309.
- Luo, B. and Hancock, E.R., 1997, July. Slice interpolation using the distance transform and morphing. In *Digital Signal Processing Proceedings, 1997. DSP 97., 1997 13th International Conference on* (Vol. 2, pp. 1083-1086). IEEE.
- Luo, L., Jiang, Z., Wei, D., Manabe, K.I., Zhao, X., Wu, D. and Furushima, T., 2016. Effects of surface roughness on micro deep drawing of circular cups with consideration of size effects. *Finite Elements in Analysis and Design*, 111, pp.46-55.
- Luo, M. and Wierzbicki, T., 2010. Numerical failure analysis of a stretch-bending test on dual-phase steel sheets using a phenomenological fracture model. *International Journal of Solids and Structures*, 47(22), pp.3084-3102.
- Mahmudi, R. and Mehdizadeh, M., 1998. Surface roughening during uniaxial and equibiaxial stretching of 70-30 brass sheets. *Journal of Materials Processing Technology*, 80, pp.707-712.
- Mandal, S., Rakesh, V., Sivaprasad, P.V., Venugopal, S. and Kasiviswanathan, K.V., 2009. Constitutive equations to predict high temperature flow stress in a Ti-modified austenitic stainless steel. *Materials Science and Engineering: A*, 500(1), pp.114-121.
- McKay, M.D., Beckman, R.J. and Conover, W.J., 2000. A comparison of three methods for selecting values of input variables in the analysis of output from a computer code. *Technometrics*, 42(1), pp.55-61.
- Meng, B. and Fu, M.W., 2015. Size effect on deformation behavior and ductile fracture in microforming of pure copper sheets considering free surface roughening. *Materials & Design*, 83, pp.400-412.
- Meyers, M.A. and Chawla, K.K., 1984. *Mechanical Metallurgy: Principles and Applications* New Jersey: Prentice-Hall.
- Mohr, D. and Marcadet, S.J., 2015. Micromechanically-motivated phenomenological Hosford–Coulomb model for predicting ductile fracture initiation at low stress

- triaxialities. *International Journal of Solids and Structures*, 67, pp.40-55.
- Moser, N.H., Gross, T.S. and Korkolis, Y.P., 2014. Martensite formation in conventional and isothermal tension of 304 austenitic stainless steel measured by X-ray diffraction. *Metallurgical and Materials Transactions A*, 45(11), pp.4891-4896.
- Needleman, A., 1972. A numerical study of necking in circular cylindrical bar. *Journal of the Mechanics and Physics of Solids*, 20(2), pp.111-127.
- Nemat-Nasser, S., Guo, W.G. and Kihl, D.P., 2001. Thermomechanical response of AL-6XN stainless steel over a wide range of strain rates and temperatures. *Journal of the Mechanics and Physics of Solids*, 49(8), pp.1823-1846.
- Norris, D.M., Moran, B., Scudder, J.K. and Quinones, D.F., 1978. A computer simulation of the tension test. *Journal of the Mechanics and Physics of Solids*, 26(1), pp.1-19.
- Osakada, K. and Oyane, M., 1971. On the roughening of free surface in deformation processes. *Bulletin of JSME*, 14(68), pp.171-177.
- Peirs, J., Verleysen, P., Van Paepegem, W. and Degrieck, J., 2011. Determining the stress-strain behaviour at large strains from high strain rate tensile and shear experiments. *International Journal of Impact Engineering*, 38(5), pp.406-415.
- Petch, N.J., 1953. The cleavage strength of polycrystals. *Journal of the Iron and Steel Institute*, 174, pp.25-28.
- Petit, J., Montay, G. and François, M., 2014. Strain rate measurements by speckle interferometry for necking investigation in stainless steel. *International Journal of Solids and Structures*, 51(2), pp.540-550.
- Pierron, F., Zhavoronok, S. and Grédiac, M., 2000. Identification of the through-thickness properties of thick laminated tubes using the virtual fields method. *International Journal of Solids and Structures*, 37(32), pp.4437-4453.
- Raabe, D., Sachtleber, M., Weiland, H., Scheele, G. and Zhao, Z., 2003. Grain-scale micromechanics of polycrystal surfaces during plastic straining. *Acta Materialia*, 51(6), pp.1539-1560.
- Raya, S.P. and Udupa, J.K., 1990. Shape-based interpolation of multidimensional objects. *IEEE transactions on medical imaging*, 9(1), pp.32-42.
- Regis, R.G. and Shoemaker, C.A., 2005. Constrained global optimization of expensive black box functions using radial basis functions. *Journal of Global Optimization*, 31(1), pp.153-171.
- Reis, L.C., Oliveira, M.C., Santos, A.D. and Fernandes, J.V., 2016. On the determination of the work hardening curve using the bulge test. *International Journal of Mechanical Sciences*, 105, pp.158-181.

- Ripley, P.W. and Korkolis, Y.P., 2015. Multiaxial deformation apparatus for testing of microtubes under combined axial-force and internal-pressure. *Experimental Mechanics*, pp.1-14.
- Romanova, V., Balokhonov, R., Zinovieva, O. and Shakhidjanov, V., 2016. Numerical study of the surface hardening effect on the deformation-induced roughening in titanium polycrystals. *Computational Materials Science*, 116, pp.96-102.
- Rowenhorst, D.J., Gupta, A., Feng, C.R. and Spanos, G., 2006. 3D crystallographic and morphological analysis of coarse martensite: combining EBSD and serial sectioning. *Scripta Materialia*, 55(1), pp.11-16.
- Rusinek, A. and Klepaczko, J.R., 2001. Shear testing of a sheet steel at wide range of strain rates and a constitutive relation with strain-rate and temperature dependence of the flow stress. *International Journal of Plasticity*, 17(1), pp.87-115.
- Sachtleber, M., Raabe, D. and Weiland, H., 2004. Surface roughening and color changes of coated aluminum sheets during plastic straining. *Journal of Materials Processing Technology*, 148(1), pp.68-76.
- Saje, M., 1979. Necking of a cylindrical bar in tension. *International Journal of Solids and Structures*, 15(9), pp.731-742.
- Sasaki, K., Kakehi, K., Korkolis Y.P. and Furushima, T., Investigation of Deformation-induced Surface Roughening based on Microstructure Analysis in Polycrystalline Metal Sheets, *The 10th Asian Workshop on Micro/Nano Forming Technology, AWMFT2017*, October 15th -17th, 2017, Pohang, South Korea
- Scheider, I., Brocks, W. and Cornec, A., 2004. Procedure for the determination of true stress-strain curves from tensile tests with rectangular cross-section specimens. *Journal of Engineering Materials and Technology-Trans. ASME*, 126(1), pp.70-76.
- Shenoy, M., Tjiptowidjojo, Y. and McDowell, D., 2008. Microstructure-sensitive modeling of polycrystalline IN 100. *International Journal of Plasticity*, 24(10), pp.1694-1730.
- Shimizu, I., Okuda, T., Abe, T. and Tani, H., 2001. Surface roughening and deformation of grains during uniaxial tension of polycrystalline iron. *JSME International Journal Series A Solid Mechanics and Material Engineering*, 44(4), pp.499-506.
- Simmons, G. and Wang, H., 1970. *Single Crystal Elastic Constants and Calculated Aggregate Properties*. MIT Press.
- Stein, C.A., Cerrone, A., Ozturk, T., Lee, S., Kenesei, P., Tucker, H., Pokharel, R., Lind, J., Hefferan, C., Suter, R.M. and Ingraffea, A.R., 2014. Fatigue crack initiation, slip localization and twin boundaries in a nickel-based superalloy. *Current Opinion in Solid State and Materials Science*, 18(4), pp.244-252.

- Stoudt, M.R., Levine, L.E., Creuziger, A. and Hubbard, J.B., 2011. The fundamental relationships between grain orientation, deformation-induced surface roughness and strain localization in an aluminum alloy. *Materials Science and Engineering: A*, 530, pp.107-116.
- Sung, J.H., Kim, J.H. and Wagoner, R.H., 2010. A plastic constitutive equation incorporating strain, strain-rate, and temperature. *International Journal of Plasticity*, 26(12), pp.1746-1771.
- Surazhsky, T., Surazhsky, V., Barequet, G. and Tal, A., 2001. Blending polygonal shapes with different topologies. *Computers & Graphics*, 25(1), pp.29-39.
- Tadros, A.K. and Mellor, P.B., 1978. An experimental study of the in-plane stretching of sheet metal. *International Journal of Mechanical Sciences*, 20(2), pp.121-133.
- Tardif, N. and Kyriakides, S., 2012. Determination of anisotropy and material hardening for aluminum sheet metal. *International Journal of Solids and Structures*, 49(25), pp.3496-3506.
- Theocaris, P.S. and Marketos, E., 1967. The formation of necking in polycrystalline steel. *Acta Mechanica*, 3(2), pp.103-122.
- Turner, T.J. and Miller, M.P., 2007. Modeling the influence of material structure on deformation induced surface roughening in AA7050 thick plate. *Journal of Engineering Materials and Technology*, 129(3), pp.367-379.
- Tvergaard, V., 1993. Necking in tensile bars with rectangular cross-section. *Computer Methods in Applied Mechanics and Engineering*, 103(1-2), pp.273-290.
- Uchic, M.D., Groeber, M.A., Dimiduk, D.M. and Simmons, J.P., 2006. 3D microstructural characterization of nickel superalloys via serial-sectioning using a dual beam FIB-SEM. *Scripta Materialia*, 55(1), pp.23-28.
- Van Tijum, R., Vellinga, W.P. and De Hosson, J.T.M., 2007. Surface roughening of metal-polymer systems during plastic deformation. *Acta Materialia*, 55(8), pp.2757-2764.
- Wang, L. and Tong, W., 2015. Identification of post-necking strain hardening behavior of thin sheet metals from image-based surface strain data in uniaxial tension tests. *International Journal of Solids and Structures*, 75, pp.12-31.
- Wilson, W.R. and Lee, W., 2001. Mechanics of surface roughening in metal forming processes. *Journal of Manufacturing Science and Engineering*, 123(2), pp.279-283.
- Wittridge, N.J. and Knutsen, R.D., 1999. A microtexture based analysis of the surface roughening behaviour of an aluminium alloy during tensile deformation. *Materials Science and Engineering: A*, 269(1), pp.205-216.

- Wu, P.D. and Lloyd, D.J., 2004. Analysis of surface roughening in AA6111 automotive sheet. *Acta Materialia*, 52(7), pp.1785-1798.
- Yamaguchi, K. and Mellor, P.B., 1976. Thickness and grain size dependence of limit strains in sheet metal stretching. *International Journal of Mechanical Sciences*, 18(2), pp.85-90.
- Yi, S., Schestakow, I. and Zaefferer, S., 2009. Twinning-related microstructural evolution during hot rolling and subsequent annealing of pure magnesium. *Materials Science and Engineering: A*, 516(1-2), pp.58-64.
- Zaafarani, N., Raabe, D., Singh, R.N., Roters, F. and Zaefferer, S., 2006. Three-dimensional investigation of the texture and microstructure below a nanoindent in a Cu single crystal using 3D EBSD and crystal plasticity finite element simulations. *Acta Materialia*, 54(7), pp.1863-1876.
- Zaefferer, S., Wright, S.I. and Raabe, D., 2008. Three-dimensional orientation microscopy in a focused ion beam–scanning electron microscope: A new dimension of microstructure characterization. *Metallurgical and Materials Transactions A*, 39(2), pp.374-389.
- Zecevic, M. and Knezevic, M., 2015. A dislocation density based elasto-plastic self-consistent model for the prediction of cyclic deformation: Application to AA6022-T4. *International Journal of Plasticity*, 72, pp.200-217.
- Zecevic, M. and Knezevic, M., 2018. A new visco-plastic self-consistent formulation implicit in dislocation-based hardening within implicit finite elements: Application to high strain rate and impact deformation of tantalum. *Computer Methods in Applied Mechanics and Engineering*, 341, pp.888-916.
- Zhang, K.S. and Li, Z.H., 1994. Numerical analysis of the stress-strain curve and fracture initiation for ductile material. *Engineering Fracture Mechanics*, 49(2), pp.235-241.
- Zhang, P., Karimpour, M., Balint, D. and Lin, J., 2012. Three-dimensional virtual grain structure generation with grain size control. *Mechanics of Materials*, 55, pp.89-101.
- Zhang, Z., Lunt, D., Abdolvand, H., Wilkinson, A.J., Preuss, M. and Dunne, F.P., 2018. Quantitative investigation of micro slip and localization in polycrystalline materials under uniaxial tension. *International Journal of Plasticity*, 108, pp.88-106.
- Zhang, Z.L., Hauge, M., Ødegård, J. and Thaulow, C., 1999. Determining material true stress–strain curve from tensile specimens with rectangular cross-section. *International Journal of Solids and Structures*, 36(23), pp.3497-3516.
- Zhao, Z., Radovitzky, R. and Cuitino, A., 2004. A study of surface roughening in fcc metals using direct numerical simulation. *Acta Materialia*, 52(20), pp.5791-5804.

Zhao, Z., Ramesh, M., Raabe, D., Cuitino, A.M. and Radovitzky, R., 2008. Investigation of three-dimensional aspects of grain-scale plastic surface deformation of an aluminum oligocrystal. *International Journal of Plasticity*, 24(12), pp.2278-2297.

APPENDIX A

Examples of infrared images of the 15 and 35 °C isothermal tests are shown in Fig. A1, to illustrate the uniformity of the temperature field during testing. The images were taken right before failure, i.e., past necking. Contrast these to Fig. 1.16, which shows the development of a temperature gradient during the conventional tension test.

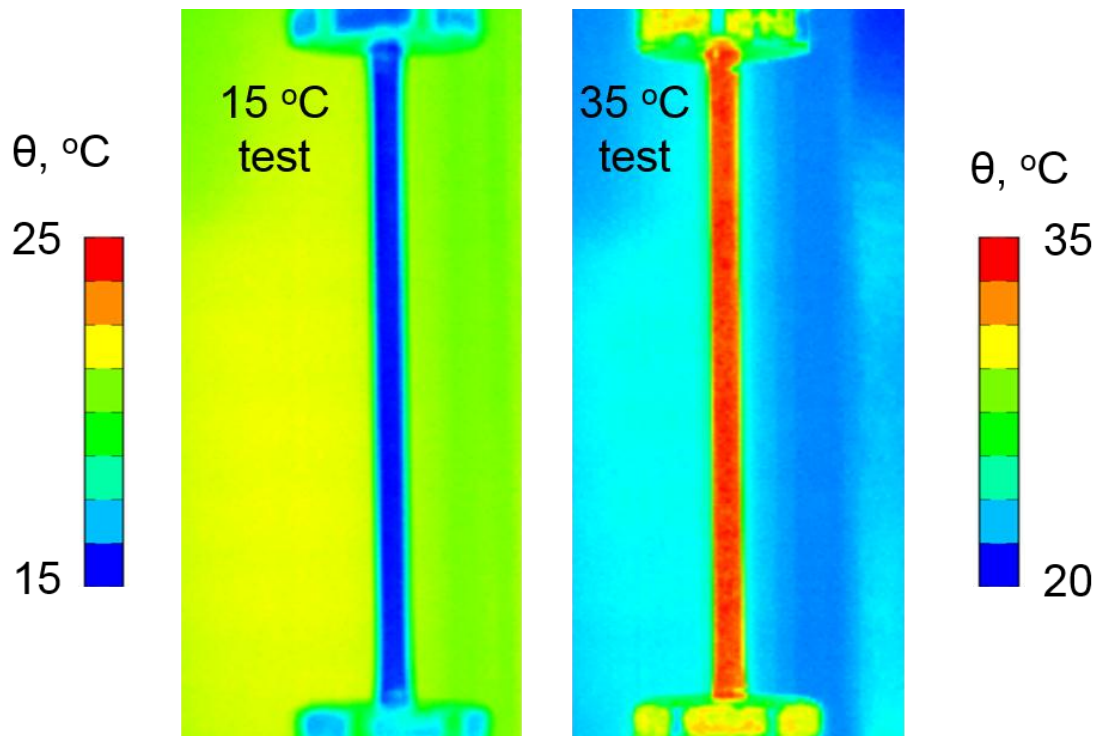


Figure A1 – Infrared images of a tube during isothermal tests, taken after necking but right before failure. Test at 15 °C is shown on the left, test at 35 °C is shown on the right.

APPENDIX B

Austenitic stainless steels are prone to strain-induced martensitic transformation (e.g., Moser *et al.*, 2014 and the references therein). However, the particular material in hand did not exhibit this transformation, perhaps because of the relatively high Nickel content (see Table 1.1). The absence of martensite was suspected after testing since the specimens did not become magnetic, and was verified by X-ray diffraction, using the same equipment as in Moser *et al.*, (2014) with the following settings: Cu K_{α} tube at 40 kV and 30 mA; scanning angle 2θ between 30° and 100° ; scanning rate of $2^{\circ}/\text{min}$ using steps of 0.02° . The resulting intensity plot for a specimen that failed in conventional tension is shown in Fig. B1, including, at the bottom, the expected peaks for iron (BCC) and γ -iron (FCC). It can be seen that the microstructure of the deformed SS-304L has remained austenitic (i.e., FCC).

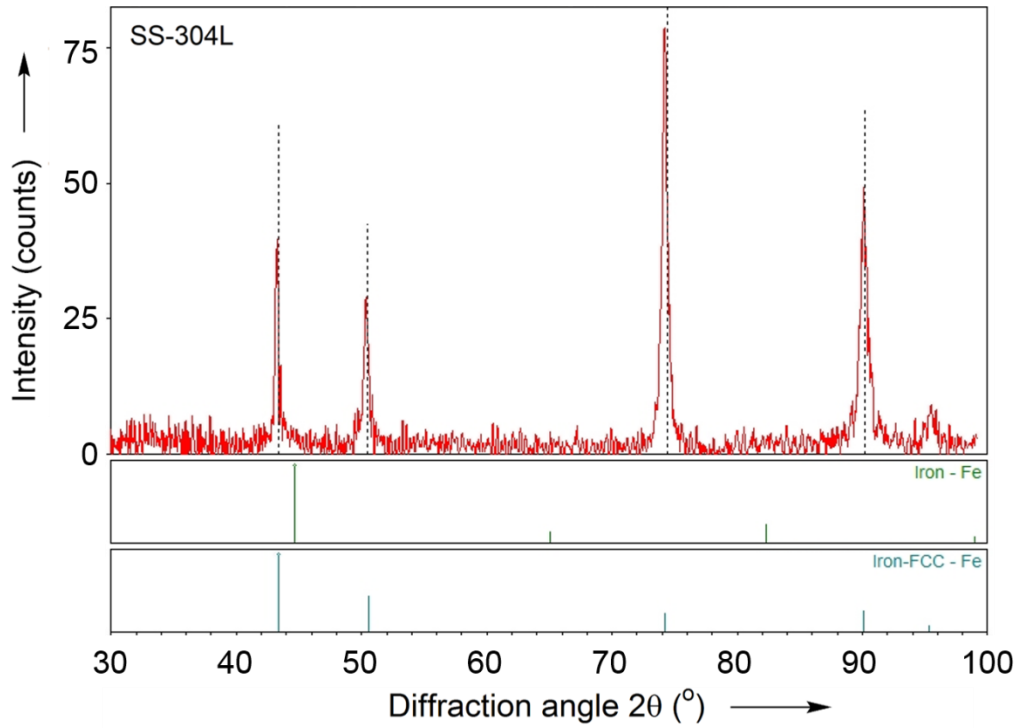


Figure B1 – Intensity plot from X-ray diffraction of a deformed SS-304L specimen after failure. The microstructure has remained FCC, with no evidence of martensite forming.

APPENDIX C

In this Appendix, we estimate the probability of “false-positive” – a case when, for a given EBSD color (say, at the top surface), the corresponding color (at the bottom) accidentally belongs to a different, rather than the same grain.

Colors are represented as intensities of red, green and blue (RGB), with the values ranging from 0 to 255 (integers) when stored in a digital computer. Each color can then be mapped into a point inside the cube, see Fig. C1. We will call two colors “similar” if the Euclidian distance between two corresponding points is less than some threshold value t . In our experiments, it was observed that the EBSD software produces colors that contain at least one intensity (red, green or blue) equal to 255, which means that we only have colors lying in the 3 faces of the cube in the first octant of RGB space. Then the probability of a given color (at one surface) being similar to another is equal to a probability of a point randomly sampled at one of these 3 faces of the RGB cube (Fig. C1) being inside a circle with radius t . This probability can then be calculated as the ratio of the two areas, or:

$$p \approx \frac{A_{circle}}{A_{total}} = \frac{\pi t^2}{3 \times 255^2} \quad (C1)$$

The “approximately equal” sign in Eq. (C1) indicates that this is a rough estimation that assumes colors to be following a uniform random distribution. In reality, colors could follow a more pronounced distribution, depending on how strong the texture is.

Also, Eq. (C1) assumes colors to be continuous random variables, while they are actually triples of integers and therefore form a finite set of points.

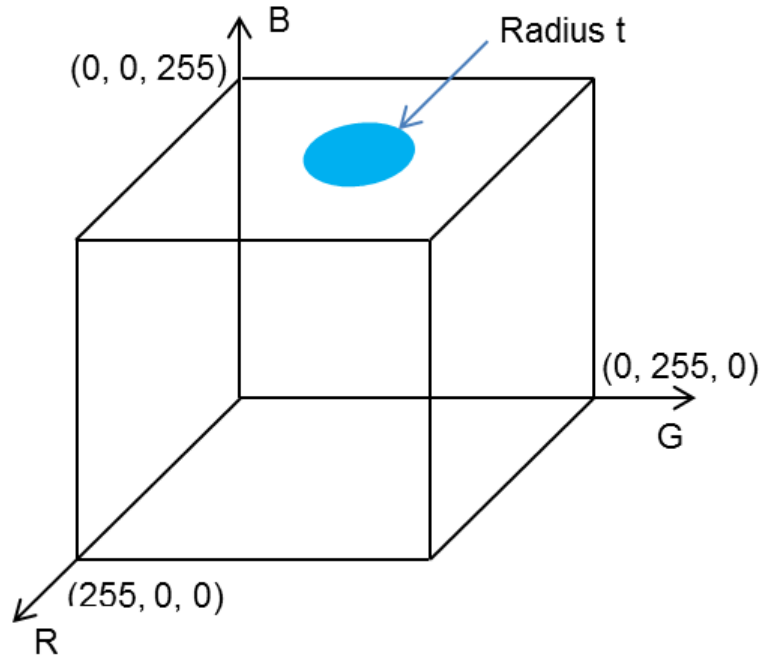


Figure C1 – Representation of a color in the RGB space including a circle representing proximity of two colors.

To get an estimate of the threshold t we analyzed 10 similar color pairs from our data (Section 3.3b) that we know they belong to the same grain (since we performed sequential sectioning through the thickness, see Fig. 3.5). The data is included in Table C1 and a few examples are shown in Fig. C2. The greatest color distance between colors at the top and bottom surfaces that we observed was 21. Using this value as a threshold t in Eq. (C1) we obtain the probability of false-positive as $p \approx 0.007 = 0.7\%$. We can therefore conclude that it is very unlikely that two regions in the two scans have similar colors but in fact belong to different grains.

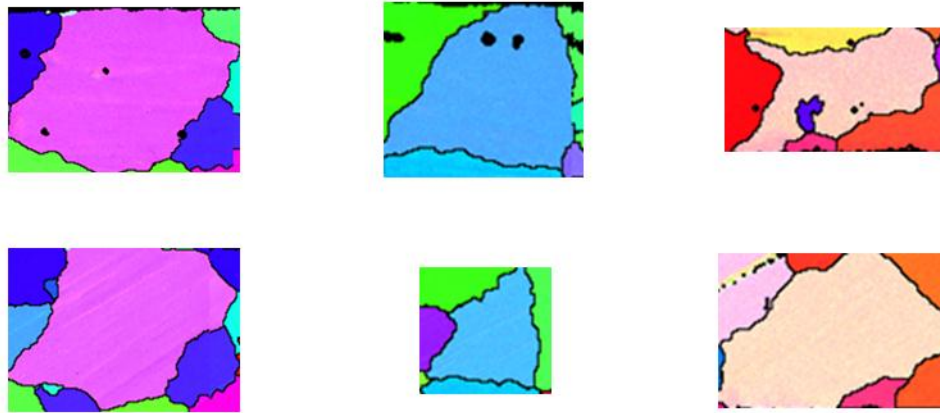


Figure C2 – Three pairs of grains from the EBSD scans of the top and bottom surfaces (top and bottom rows, respectively).

Table C1 – Colors of pairs of grains at the top and bottom surfaces used in this analysis.

Grain #	RGB of grain at the top surface	RGB of grain at the bottom surface	Color distance
1	(239, 84, 255)	(237, 98, 255)	14
2	(75, 172, 255)	(76, 193, 255)	21
3	(255, 203, 197)	(255, 222, 195)	19
4	(255, 40, 23)	(255, 35, 27)	6
5	(255, 185, 100)	(255, 192, 110)	12
6	(255, 131, 6)	(255, 132, 11)	5
7	(10, 34, 255)	(9, 41, 255)	7
8	(85, 255, 97)	(79, 255, 82)	16
9	(97, 255, 66)	(90, 255, 71)	8
10	(102, 255, 33)	(111, 255, 48)	17

APPENDIX D

The texture of the as-received polycrystalline AA5052-O is shown in Fig. D1. In the pole figures presented, we can observe patterns typical of rolled texture, such as two parallel features in $\{111\}$ pole figure. In addition, we can see presence of cube texture (pronounced poles at top, bottom, left, right) in $\{100\}$ pole figure, which is due to recrystallization.

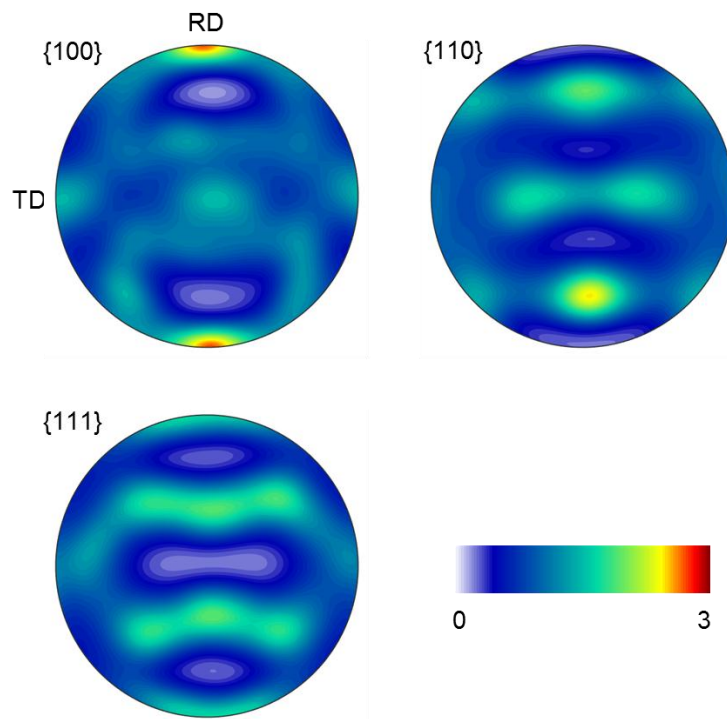


Figure D1 – Crystallographic texture of as-received polycrystalline AA5052-O, shown as a set of pole figures.

APPENDIX E

In this appendix we compare the performance of a non-columnar model (introduced and analyzed in [Chapter 4](#)) versus a columnar model ([Fig. E1](#)). The columnar model is constructed by extruding the grain shapes from the top face through the thickness, which results in slightly different 3D grain shapes. All other parameters (initial texture, boundary conditions, material constants) were kept the same.

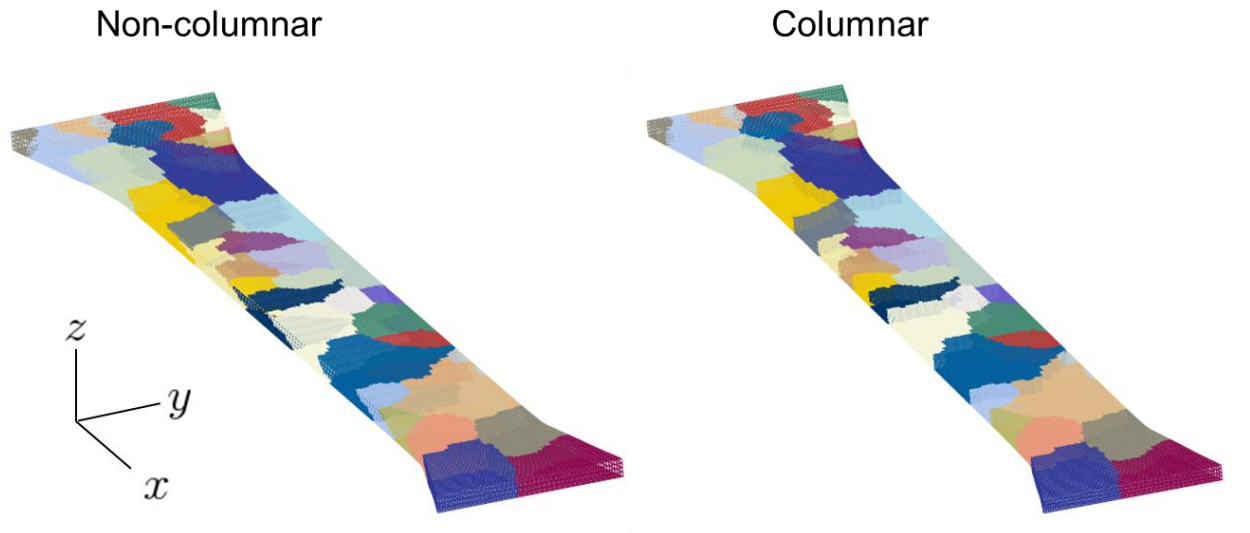


Figure E1 – Finite element meshes of non-columnar and columnar models.

In [Fig. E2](#) the deformed shapes of both models are shown. These shapes can be translated into out-of-plane displacement fields that are shown in [Fig. E3](#). As can be observed, there is no substantial difference between the two surface profiles; both models seem to miss few local peaks/valleys that appear in experimental results. This is visible when the absolute errors between models and experiments are compared side-by-side ([Fig. E4](#)).

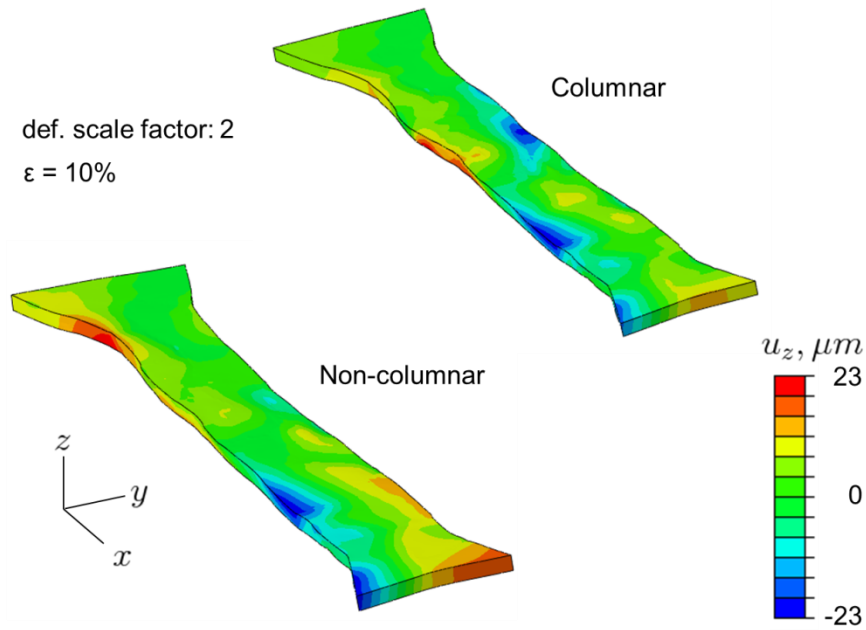


Figure E2 – Deformed shapes of both columnar and non-columnar models along with the distribution of z-displacements (u_z). A deformation scale factor of 2 is used in order to exaggerate deformed shape, for easier visualization.

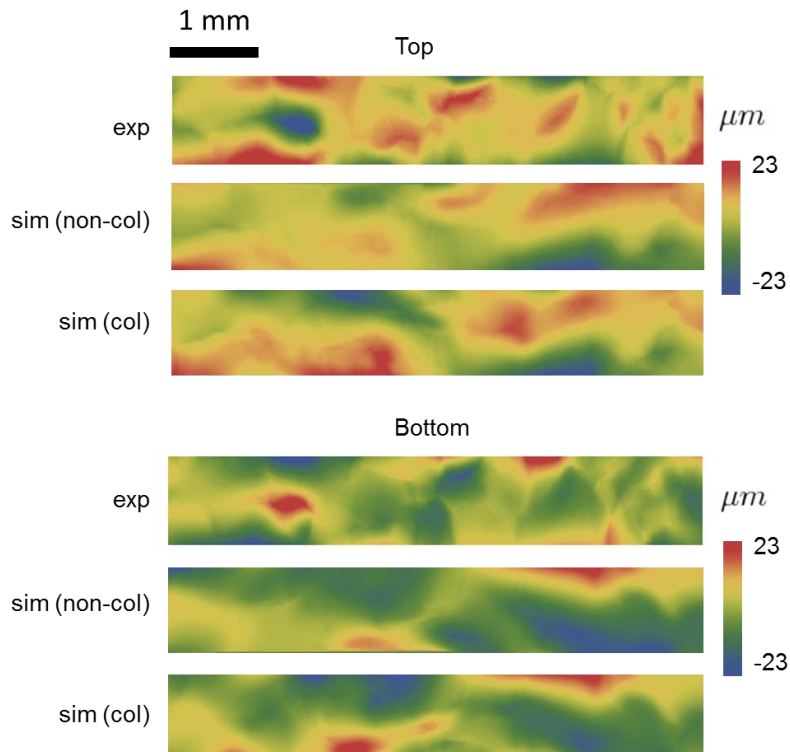


Figure E3 – Surface topographies for columnar/non-columnar models at the top and bottom faces of the specimen, extracted from simulation (marked as “sim”) and experiment (marked as “exp”) at 10% nominal strain.

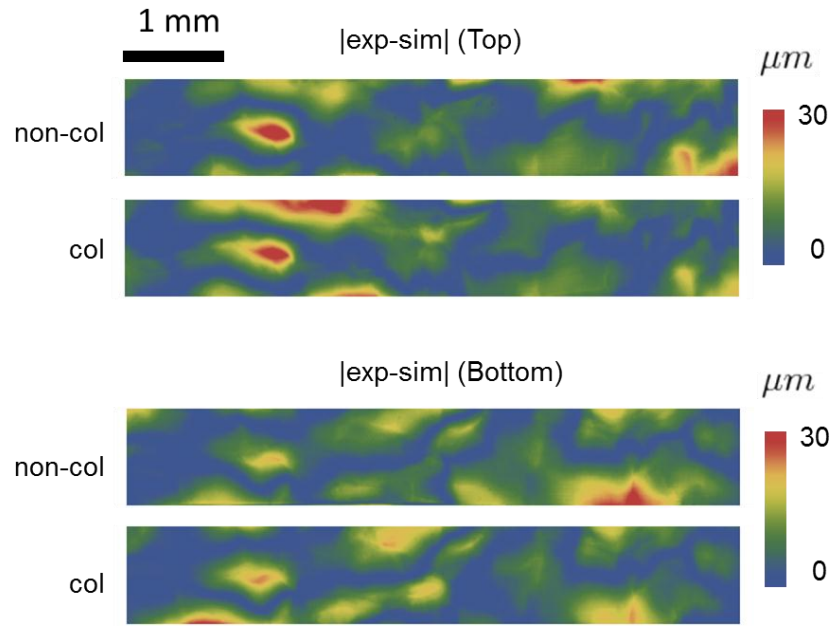
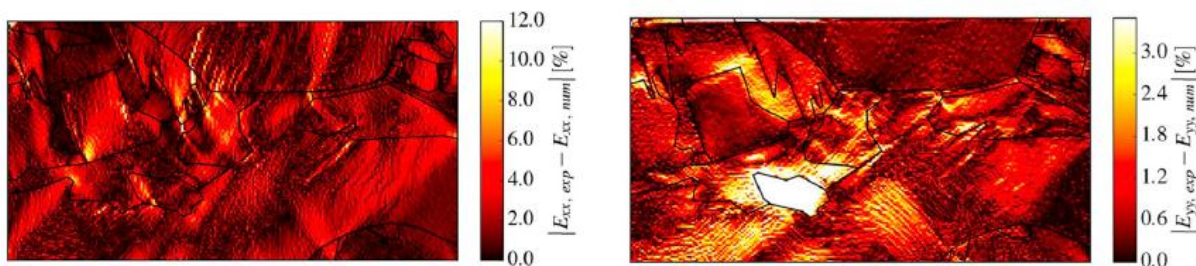


Figure E4 – The absolute difference between simulation and experiment (marked as “|exp-sim|”) for both columnar and non-columnar models.

APPENDIX F

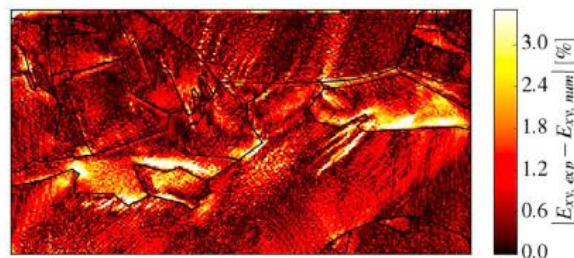
The goal of this Appendix is to describe state-of-art research results, using advanced crystal plasticity models, and their performance in accurately predicting the localized (and also average) deformation of polycrystal and oligocrystal specimens. Several cases extracted from 2018 publications are shown below.

Data shown in Fig. F1 was extracted from [Baudoin et al., 2018](#) and represents the absolute difference between predicted and measured strain fields at 4% mean axial strain. These results were obtained for columnar model of commercially-pure Titanium. These plots show that many regions have error values that are comparable to 4% or even higher.



(a) Axial strain E_{xx} .

(b) Transverse strain E_{yy} .



(c) Shear strain E_{xy} .

Figure F1 – The absolute difference between measured (DIC) and predicted strain components ([Baudoin et al., 2018](#)).

In Fig. F2 strain data was extracted from a path laying on a surface of a Ti-6Al-4V specimen (Zhang *et al.*, 2018) during a uniaxial tension. The comparison between strain results from columnar CPFE model containing about 50 grains and DIC measurements shows that many regions were not captured well.

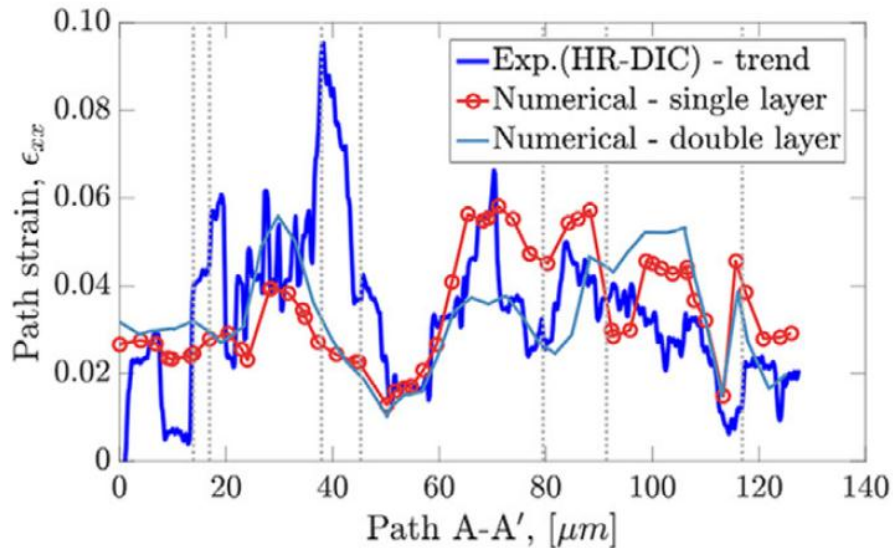


Figure F2 – Measured (DIC) and predicted path strain (Zhang *et al.*, 2018).

Figure F3 comes from the work of (Kubo *et al.*, 2018) who examined both uniaxial ($\beta=0$) and equibiaxial ($\beta=1$) stretching of IF steel. In their numerical model, an assembly of about 70 grains was used. Figure F3 shows that for the case of uniaxial stretching the average surface roughness value is captured well. However, the case of biaxial stretching was found to be more challenging.

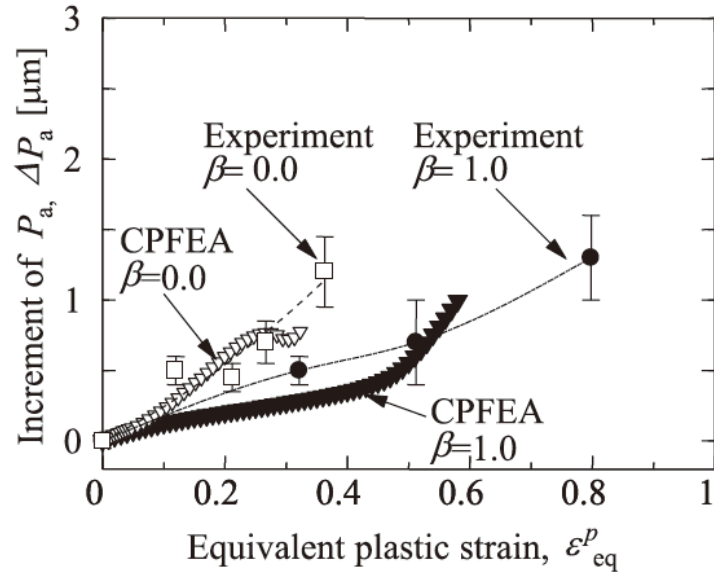


Figure F3 – Measured and predicted values of R_a (Kubo et al., 2018).

In summary, our present results are in qualitative agreement with these recent works, in the sense that while the surface roughening is generally captured well in an average sense, some local predictions can be deficient. This was also found in this work, e.g., Fig. 4.11. Some thoughts about improving the current state-of-art are discussed in Chapter 5.